UNIVERSIDADE ESTADUAL DE CAMPINAS
Faculdade de Engenharia Civil, Arquitetura e Urbanismo

Carlos Henrique Chama Puga

A novel H(div)-based hybridized formulation for Stokes equations with applications in complex flow patterns

Uma nova formulação H(div) hibridizada para equações de Stokes com aplicações em padrões complexos de escoamento

Campinas
2024

Carlos Henrique Chama Puga

A novel H(div)-based hybridized formulation for Stokes equations with applications in complex flow patterns

Uma nova formulação H(div) hibridizada para equações de Stokes com aplicações em padrões complexos de escoamento

Dissertação de Mestrado apresentada à Faculdade de Engenharia Civil, Arquitetura e Urbanismo da Universidade Estadual de Campinas como parte dos requisitos para a obtenção do título de Mestre em Engenharia Civil na área de Estruturas e Geotécnica.

Master's Degree Thesis presented to the School of Civil Engineering, Architecture and Urban Planning of the Universidade Estadual de Campinas in partial fulfillment of the requirements for the degree of Master of Science in Civil Engineering in the area of Structures and Geotechnics.

Advisor/Orientador: Prof. Dr. Philippe Remy Bernard Devloo
Co-advisor/Co-orientador: Prof. Dr. Nathan Shauer

Este exemplar corresponde à versão final da Dissertação de Mestrado apresentada por Carlos Henrique Chama Puga, orientada pelo Prof. Dr. Philippe Remy Bernard Devloo, e co-orientada pelo Prof. Dr. Nathan Shauer.

Campinas
2024

Ficha catalográfica
Universidade Estadual de Campinas (UNICAMP)
Biblioteca da Área de Engenharia e Arquitetura
Elizangela Aparecida dos Santos Souza - CRB 8/8098

P963n

Puga, Carlos Henrique Chama, 1999-
A novel H(div)-based hybridized formulation for Stokes equations with applications in complex flow patterns / Carlos Henrique Chama Puga. – Campinas, SP : [s.n.], 2024.

Orientador: Philippe Remy Bernard Devloo.
Coorientador: Nathan Shauer.
Dissertação (mestrado) – Universidade Estadual de Campinas (UNICAMP), Faculdade de Engenharia Civil, Arquitetura e Urbanismo.

1. Equações de Navier-Stokes. 2. Métodos dos elementos finitos. 3. Geração numérica de malhas (Analise numérica). 4. domínios obstruídos. I. Devloo, Philippe Remy Bernard, 1958-. II. Shauer, Nathan, 1989-. III. Universidade Estadual de Campinas (UNICAMP). Faculdade de Engenharia Civil, Arquitetura e Urbanismo. IV. Título.

Informações Complementares

Título em outro idioma: Uma nova formulação H(div) hibridizada para equações de Stokes com aplicações em padrões complexos de escoamento
Palavras-chave em inglês:
Navier-Stokes equations
Finite element method
Numerical mesh generation
Área de concentração: Estruturas e Geotécnica
Titulação: Mestre em Engenharia Civil
Banca examinadora:
Philippe Remy Bernard Devloo [Orientador]
Maicon Ribeiro Correa
Hugo Luiz Oliveira
Data de defesa: 06-08-2024
Programa de Pós-Graduação: Engenharia Civil

Identificação e informações acadêmicas do(a) aluno(a)
- ORCID do autor: https://orcid.org/0000-0002-2275-3391
- Currículo Lattes do autor: http://lattes.cnpq.br/6056491688628913

UNIVERSIDADE ESTADUAL DE CAMPINAS
Faculdade de Engenharia Civil, Arquitetura e Urbanismo

A novel H(div)-based hybridized formulation for Stokes equations with applications in complex flow patterns

Carlos Henrique Chama Puga

Dissertação de Mestrado aprovada pela Banca Examinadora, constituída por:

Prof. Dr. Philippe Remy Bernard Devloo
Presidente e Orientador / FECFAU-UNICAMP

Prof. Dr. Maicon Ribeiro Correa
Membro Titular / IMECC-UNICAMP

Prof. Dr. Hugo Luiz Oliveira
Membro Titular / FECFAU-UNICAMP

A Ata de defesa com as respectivas assinaturas dos membros encontra-se no processo de vida acadêmica do aluno.

Campinas, 06 de Agosto de 2024.

“Dois problemas se misturam:
a verdade do universo e
a prestação que vai vencer”

- Raul Seixas

Dedication

Dedico esse trabalho a todos os professores e professoras que passaram pela minha vida. Vocês tiveram um forte impacto na minha carreira e principalmente na maneira como enxergo o mundo e as coisas à minha volta. Gostaria de agradecer especificamente ao Prof. Dr. Luiz Vieira Jr. sem o qual não tomaria a importante decisão de ingressar no mestrado. Ao Prof. Dr. Gustavo Siqueira, que em meio a brincadeiras e piadas me ensinou e me fez perceber como é bom o mundo da pesquisa. Ao Prof. Dr. Nathan Shauer, a quem devo muito mais do que orientações e conversas de corredor no LabMeC. Por fim, agradecimentos ao Prof. Dr. Philippe Devloo, que me presenteou com a oportunidade de trabalhar em seu laboratório, mesmo com apenas metade do tempo para me formar. Phil, você é uma pessoa excepcional e um exemplo a ser seguido. Vocês de fato mudaram a minha vida em aspectos que eu nem mesmo sei descrever. Hoje posso dizer que finalmente encontrei a área que quero seguir e devo isso a cada um de vocês.

Dedico também a todas as pessoas que o mestrado me apresentou e que hoje em dia tenho o prazer de chamar de amigos. Ao Dr. Giovane Avancini, que me inspirou tanto durante o mestrado e principalmente por ter me ensinado a importância de se ter um bom amigo. À Ingrid e ao Marco, pessoas maravilhosas que eu não sei como agradecer por me aguentarem apesar de tudo que eu faço e falo. Espero que a nossa amizade dure por anos. Aos amigos feitos no LabMeC e no RELab, em especial ao Fran, Sérgio e à Camila.

Aos moradores da Replay, sem os quais não teria uma casa pra chamar de lar. Ferraz, Wesley, Rapha, Randall, Robs, Guth, Jordan e Airton, meus mais sinceros agradecimentos por esses dois anos ao lado de vocês. Ao Rodrigo por sempre me fazer rir quando preciso. A Dourado, Zamy e Bruna que apesar da distância sempre estiveram presentes. À Rainha e aos Quatro Cabeleiras do Após-Calypso, que me mantiveram são durante infindáveis noites de estudo.

Por fim, à minha família. Aos meus primos queridos, em especial Nicole, que cresceram comigo e me tornaram a pessoa que sou hoje. À Maria Clara e Manuela por serem as melhores irmãs que eu poderia ter. E claro, Pai e Mãe por sempre me apoiarem durante a minha trajetória e cuidarem de mim. Eu não seria nada sem vocês. Amo eternamente cada um de vocês.

Acknowledgments

The author thankfully acknowledges the financial support provided by Total Energies Brazil through FUNCAMP (processes 23289-2) and the Brazilian National Council for Scientific and Technological Development (grants 305823/2017-5 and 309597/2021-8).

Resumo

As equações de Stokes são usadas para modelar o movimento de fluidos onde termos inerciais podem ser desprezados, como por exemplo na indústria de petróleo. Técnicas tradicionais de elementos finitos, como a formulação de Taylor-Hood, não garantem a conservação local da massa ponto a ponto. Isso pode ser alcançado empregando uma formulação mista com a combinação adequada de espaços H(div) e L^2. Para estudar o impacto de obstruções no fluxo de um fluído, este trabalho apresenta uma nova formulação híbrida-híbrida para resolver as equações de Stokes. Além disso, uma variação do espaço H(div) tradicional, chamada Hdiv-C, é usada para aproximar o campo de velocidade. O espaço Hdiv-C é criado usando conceitos da sequência exata de De Rham e requer menos funções do que os espaços H(div) tradicionais de elementos finitos. Um algoritmo visando a geração automática de malhas é desenvolvido para criar domínios obstruídos. Um protótipo em escala é numericamente estudado para mostrar um procedimento que pode ser adotado para avaliar o melhor tipo de obstrução capaz de impor uma queda de pressão específica no fluxo. Os resultados mostram que a formulação dupla híbrida combinada com o espaço Hdiv-C é adequada para resolver problemas de Stokes, com taxas de convergência ótimas, comparáveis ao elemento de Taylor-Hood.

Palavras-chave: Equações de Stokes, formulação híbrida-híbrida, espaços H(div), geração automática de malhas, domínios obstruídos.

Abstract

The Stokes equations are used to model the motion of fluid flows where inertial terms can be neglected, such as in the production well context. Traditional finite element approaches such as the Taylor-Hood element do not ensure the local conservation pointwise of the mass. This can be achieved by employing a mixed formulation with the proper combination of H(div) and L^2 spaces. To study the impact of obstructed flows, this work presents a new hybrid-hybrid formulation to solve the Stokes equations. In addition, a variation of the traditional H(div) space, called Hdiv-C, is used to approximate the fields. The Hdiv-C space is created using concepts of the exact De Rham sequence and is shown to yield a smaller global system of equations than traditional finite element H(div) spaces. An algorithm aiming the automatic mesh generation is developed to create obstructed domains and verify the impacts of the obstructions on the flow pattern. An in-scale prototype is studied to show a procedure that can be adopted to numerically evaluate the best type of obstruction capable of imposing a specific pressure drop in the flow. The results show that the hybrid-hybrid formulation combined with the Hdiv-C space is suitable for solving Stokes problems, with optimal convergence rates, comparable to the Taylor-Hood element.

Keywords: Stokes equations, hybrid-hybrid formulation, H(div) spaces, automatic mesh generation, obstructed domains.

List of Figures

List of Tables

Contents

Chapter 1

Introduction

Energy demand is rising faster than the capacity of oil production worldwide. To increase production, more advanced technologies can be employed. After the primary extraction level, the secondary and tertiary levels of oil recovery might be applied. The secondary level of extraction consists of, for instance, pumping water into the reservoir to increase reservoir pressure. The tertiary level is about enhancing the oil recovery by using chemicals, thermal procedures, and other sorts of techniques [1].

Water injection, or waterflooding, is a key element in modern processes of oil extraction. To displace the fluid within the reservoir into the production wells, water is injected into the reservoir, through injection wells. Filling the void left by produced oil, which prevents landslides and maintains high reservoir pressure and minimizing environmental impacts (reinjection of produced water) are some of the advantages of water injection [2].

Produced water injection is the most common method to increase oil production [2]. Produced water is co-produced with the oil stream and, due to the traces of oil and other chemicals, its filtration and disposal in nature are not easy tasks. In this context, aspects such as the geometry of the well, and flux pattern might have a significant impact on the injectivity of produced water into the well, and consequently, on the oil production.

Aiming to better investigate the loss of the injectivity of produced water, a project titled "Experimental and numerical study of the loss of injectivity of produced water in reservoir rock with the variation of physical and geometric parameters of the well" financed by TotalEnergies is being developed. The project is divided into experimental analyses and numerical simulations. During the experimental analyses, a 10m module will be built to assess the effects influence of the presence of solid or oil residual on the injectivity loss of the well.

However, since the flux pattern inside the module is not expected to vary significantly, obstructions will be inserted into the module to induce head loss. An in-scale prototype will be used to previously study the effects of different obstructions geometries within the module (see Figure 1.1). The prototype is 1 m long and 9 cm in diameter.

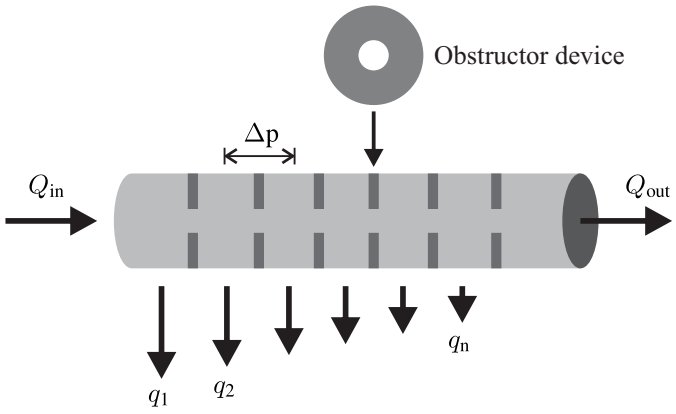

Figure 1.1: Schema for the reduced module.

Scale models might not be representative. In this work, numerical simulations aim to reproduce the fluid flow through the in-scale prototype and assess the effects of different obstructions geometries on the fluid flow.

Assuming a low Reynolds number, the flow is steady and the inertial terms can be neglected. Then, the Navier-Stokes equations can be simplified to the Stokes equations [3]. The Stokes equations are widely used to model fluid motion in various scientific and engineering fields [4–8]. In this work, it is used to model the fluid flow within the wellbore. From a mathematical perspective, the Stokes formulation can be compared to isotropic elasticity theory as both phenomena are governed by similar equations [9, 10].

Over the years, various numerical techniques have been used to solve Stokes' problems. The three main methods for simulating Stokes flow are the Finite Difference Method (FDM), the Finite Volume Method (FVM), and the Finite Element Method (FEM). FEM offers advantages such as the ability to handle irregular geometries, the versatility to impose complex boundary conditions, and work with non-uniform meshes. FEM provides reliable solutions even in the presence of material property discontinuities (in solids or fluids) and external body forces [11, 12].

When solving the Stokes equations using a finite element framework, the commonly used approach is the Galerkin Method (GM). For a comprehensive list of references on this topic, see [4, 9, 13–17]. Among the most popular methods for solving the velocity and pressure unknown fields, the Taylor-Hood formulation [18] is widely employed. The Taylor-Hood element utilizes continuous quadratic piecewise functions to approximate the velocity and continuous linear piecewise functions to approximate the pressure. In other words, both the velocity and pressure are approximated using $H^1(\Omega)$ spaces, as opposed to using discontinuous functions for the pressure ($L^2(\Omega)$ spaces). In this work, the Taylor-Hood element is used for comparison against the proposed method.

As an alternative to the traditional Galerkin Methods (GMs), Discontinuous Galerkin Methods (DGMs) have been developed. Unlike standard GMs, DGMs do not enforce continuity in the velocity components between elements. In this context, stabilization factors and/or sym-

metry terms need to be added to the finite element formulation. Examples of Discontinuous Galerkin methods can be found in [19–25].

The appropriate selection of $H(\mathrm{div}, \Omega)$-$L^2(\Omega)$ for the velocity and pressure fields has been demonstrated to enable local mass conservation of the approximation [26, 27]. This means that, assuming the flow is incompressible and there are no source or sink terms, the divergence of the velocity is zero at each point [28]. However, the tangential component of the velocity is not inherently continuous between elements, when using $H(\mathrm{div}, \Omega)$ functions. Therefore, the adopted formulation must enforce the continuity of the tangential velocity. For more details on $H(\mathrm{div}, \Omega)$ spaces, one refers to the following works [26–31].

The starting point of this work is [27], in which a semi-hybrid formulation is presented to solve Stokes' equations. The semi-hybrid formulation approximates velocity ensuring the continuity of the tangential velocity weakly by applying Lagrange multipliers. In this context, the introduced Lagrange multipliers have the physical meaning of tangential stresses. Although stable from a mathematical point of view, this formulation leads to a saddle-point system with two distinct types of Lagrange multipliers that require more sophisticated algorithms to solve. Therefore, this work proposes a second hybridization of the tangential stress aiming to improve stability and a global matrix with better spectral properties. This new approach is called hybrid-hybrid formulation.

In both the semi-hybrid and hybrid-hybrid formulations, static condensation is employed to i) enhance computational efficiency and ii) recover a symmetric positive semi-definite elemental matrix for the latter. However, there is a distinction between the two formulations in terms of the condensed system's Degrees of Freedom (DoFs). In the semi-hybrid formulation, the system after the condensation includes DoFs from velocity, pressure and traction, whereas, in the hybrid-hybrid formulation, only velocity and pressure DoFs are present.

After the static condensation is applied, the resulting system in the hybrid-hybrid formulation still has a saddle-point structure, but only the Lagrange multipliers associated with the pressure are present. The Lagrange multipliers associated with the velocity no longer yield zeros in the diagonal of the matrix, since the traction is condensed. This leads to a more stable system, from a numerical point of view, when compared to the semi-hybrid formulation. Note that despite the introduction of a new Lagrange multiplier, the total number of DoFs in the condensed system remains the same as in the semi-hybrid formulation.

The current work also aims to verify the hybrid-hybrid formulation when two different types of $H(\mathrm{div}, \Omega)$ spaces are used to approximate velocity. In Section 2 of [32], a methodology to construct a stable space for mixed problems generalized for any polynomial order is presented. The space created by this methodology is herein called Hdiv-S (here S stands for "Standard" because it is the way the space is constructed in the NeoPZ environment by default). For more information on three-dimensional Hdiv-S space, the reader is referred to [33].

The so-called Hdiv-C (C stands for "Constant" since the space is constant divergence) is the other $H(\mathrm{div}, \Omega)$-type space used in this work. One constructs an H(curl) space to filter its

functions whose curl forms a linearly independent set of divergence-free functions. Then, the edge functions from H(curl) are replaced by RT0 (Raviart Thomas zero order) functions with element-wise constant divergence. Hdiv-C space has, therefore, a reduced number of shape functions when compared to Hdiv-S space, which leads to a smaller system of equations. More details for constructing Hdiv-C spaces can be found in Section 3 from [34].

It is well-established that the accuracy and reliability of the solution depend on the choice of velocity-pressure approximation spaces [10, 35]. For example, using equal $H^1(\Omega)$ approximations for both velocity and pressure fields leads to an unstable solution and unphysical pressure oscillations [36]. To ensure the convergence of the method and overcome numerical challenges, it is necessary to satisfy the Babuska-Brezzi condition [37,38]. The approximation spaces available in NeoPZ environment satisfy the De Rham complex and consequently the LBB condition for incompressibility.

This work's main goal is to employ the hybrid-hybrid formulation to simulate fluid flow through obstructed channels. To achieve this, a new algorithm for mesh generation is developed to create meshes for any type of obstruction automatically and efficiently. The results are obtained by solving the Stokes equations, using two different variations of the $H(\mathrm{div}, \Omega)$ space (Hdiv-S and Hdiv-C) to interpolate the velocity field. Both spaces are compared to the traditional Taylor-Hood element and the effect of different obstruction geometries on the fluid flow is studied. The object-oriented programming environment NeoPZ[1] written in C++ is used to implement the numerical simulations.

1.1 Objectives

This work aims to implement the hybrid-hybrid formulation for the Stokes problem and automate mesh generation, using both Hdiv-S and Hdiv-C spaces in problems of industrial interest, more specifically, to simulate fluid flow through obstructed channels.

Specific objectives are:

- Study of the intrinsic phenomena and laws that govern fluid dynamics in the context of the Stokes problems;
- Implementation of the hybrid-hybrid formulation for Stokes problems using $H(\mathrm{div}, \Omega)$ spaces (Hdiv-S and Hdiv-C);
- Two- and three-dimensional code verification, comparing the solutions with analytical solutions and studying rates of convergence;
- Implementation of a Python Gmsh interface, capable of creating meshes with pre-defined obstructions automatically and efficiently; and
- Study of the effect of different obstructions geometries on the fluid flow.

[1] NeoPZ open source platform <https://github.com/labmec/neopz>

1.2 Dissertation Structure

This work is organized into seven chapters. Chapter 2 presents basic concepts widely employed in continuum mechanics such as material derivatives, conservation of mass and balance of momentum equations. The finite element method is properly introduced in Chapter 3, showing the process of creation for Hdiv-S and Hdiv-C shape functions, and methods applied to reduce execution time and impose boundary conditions.

Stokes equations are presented in Chapter 4 along with their weak formulation. Three different formulations are presented: the Taylor-Hood element, a classical mixed formulation approach, the semi-hybrid formulation, and finally the hybrid-hybrid. Chapter 5 shows numerical simulations used to verify the code and study the range of applications of the proposed method.

Chapter 6 presents the mesh generation algorithm, the obstruction geometries studied, and their effects on the fluid flow. Ultimately, Chapter 7 presents the conclusions and future work.

Chapter 2

Basic Concepts of Continuum Mechanics

Continuum mechanics is a branch of mechanics that deals with the study of materials (solids or fluids) as a continuous medium. A continuous medium is a set of infinitesimal particles, grouped and assessed macroscopically. It is supposed that there are no discontinuities between the particles, and the material properties can be described as continuous functions of space and time.

There are two ways to describe the behavior of a continuous medium: from the material point of view (also called Lagrangian description) and from the spatial point of view (also called Eulerian description). The material point of view follows the motion of a particle of the material, while the spatial point of view follows the motion of a fixed point in space. In solid mechanics, the material description is more used, while in fluid mechanics, the spatial description is often preferred.

In this chapter, special attention is given to the conservation and balance equations, fundamental to the understanding of the Stokes governing equations. For a comprehensive text on the topic, the reader is referred to [39–41].

2.1 Mathematical Operators

Physical phenomena are often described by the laws of continuum mechanics, which are in turn expressed in terms of differential equations. In this section, the mathematical operators gradient, divergence, and curl, usually employed in continuum mechanics are defined.

The gradient denotes the directions of the greatest change of a given function. The divergence represents the change in volume of the outward flux of a vector or tensor field from an infinitesimal volume. The curl is a measure of the rotation of a vector field.

Let g, $\boldsymbol{g}$, and $\boldsymbol{G}$ be scalar, vector, and tensor functions, respectively. The gradient, diver-

gence and curl operators are defined, in cartesian coordinates, as follows

$$\nabla g = \left\{ \frac{\partial g}{\partial x}, \frac{\partial g}{\partial y}, \frac{\partial g}{\partial z} \right\}^T, \qquad \nabla \boldsymbol{g} = \begin{bmatrix} \frac{\partial g_x}{\partial x} & \frac{\partial g_x}{\partial y} & \frac{\partial g_x}{\partial z} \\ \frac{\partial g_y}{\partial x} & \frac{\partial g_y}{\partial y} & \frac{\partial g_y}{\partial z} \\ \frac{\partial g_z}{\partial x} & \frac{\partial g_z}{\partial y} & \frac{\partial g_z}{\partial z} \end{bmatrix}, \tag{2.1}$$

$$\nabla \cdot \boldsymbol{g} = \frac{\partial g}{\partial x} + \frac{\partial g}{\partial y} + \frac{\partial g}{\partial z}, \qquad \nabla \cdot \boldsymbol{G} = \begin{bmatrix} \frac{\partial G_{xx}}{\partial x} + \frac{\partial G_{xy}}{\partial y} + \frac{\partial G_{xz}}{\partial z} \\ \frac{\partial G_{yx}}{\partial x} + \frac{\partial G_{yy}}{\partial y} + \frac{\partial G_{yz}}{\partial z} \\ \frac{\partial G_{zx}}{\partial x} + \frac{\partial G_{zy}}{\partial y} + \frac{\partial G_{zz}}{\partial z} \end{bmatrix}. \tag{2.2}$$

$$\nabla \times \boldsymbol{g} = \begin{Bmatrix} \frac{\partial g_z}{\partial y} - \frac{\partial g_y}{\partial z} \\ \frac{\partial g_x}{\partial z} - \frac{\partial g_z}{\partial x} \\ \frac{\partial g_y}{\partial x} - \frac{\partial g_x}{\partial y} \end{Bmatrix}. \tag{2.3}$$

2.2 Equations of Motion

As mentioned before, there are two ways to describe the behavior of a continuous medium: the material or Lagrangian description and the spatial or Eulerian description. Consider the configurations presented in Figure 2.1. The region Ω_0 is referred to as the reference or undeformed configuration, while the region Ω_t is known as the current or deformed configuration.

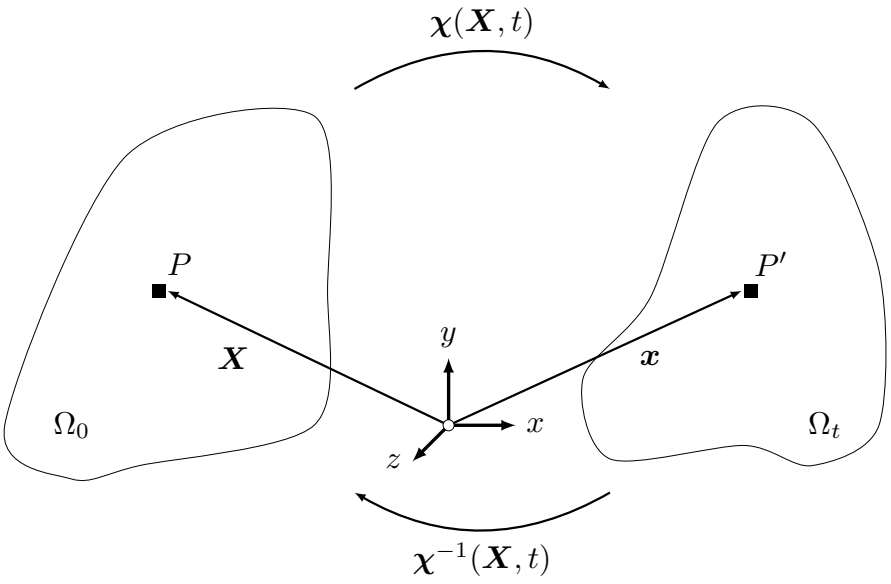

Figure 2.1: Motion and configurations of a continuous medium.

The position vector $\boldsymbol{X}$ defines the coordinates of a given particle occupying position P in the

reference configuration. Assuming that the body moves to a new position Ω_t at time t, vector $\boldsymbol{x}$ defines the coordinates of the particle occupying the spatial point P' in the current configuration. The position of particles can be described by the evolution of their spatial coordinates along time, given by the motion function $\boldsymbol{\chi}$ as follows

$$\boldsymbol{x}(\boldsymbol{X},t) = \begin{cases} \chi(X_1,t) \\ \chi(X_2,t) \\ \chi(X_3,t) \end{cases} \qquad \boldsymbol{X}(\boldsymbol{x},t) = \begin{cases} \chi^{-1}(x_1,t) \\ \chi^{-1}(x_2,t) \\ \chi^{-1}(x_3,t) \end{cases} . \tag{2.4}$$

For $\boldsymbol{\chi}$ to be properly considered as a motion function, some mathematical restrictions must be satisfied. $\boldsymbol{X}$ is the position vector at time $t = 0$. $\boldsymbol{\chi}$ must be continuous since the motion of the particles is continuous. Two particles cannot occupy simultaneously the same position in space and a particle cannot occupy two different positions at the same time.

Any property of the particle can be described in material or spatial terms. Let C and c be material and spatial fields containing the property of interest (e.g. density, velocity, etc) of a given particle. The relation between the material and spatial fields is given by Eq. (2.5)

$$c(\boldsymbol{x},t) = c(\boldsymbol{\chi}(\boldsymbol{X},t),t) = C(\boldsymbol{X},t). \tag{2.5}$$

2.3 Material Time Derivative

The material time derivative is a measure of the rate at which the material field $\mathcal{F}$ changes with time, as seen by an observer moving with the particle. It is the derivative of $\mathcal{F}$ with respect to time, keeping the spatial coordinates constant.

$$\frac{D\mathcal{F}(\boldsymbol{X},t)}{Dt} = \left(\frac{\partial \mathcal{F}}{\partial t}\right)_{\boldsymbol{X}}, \tag{2.6}$$

where the subscript $\boldsymbol{X}$ denotes that the derivative is taken keeping the spatial coordinates constant.

The material time derivative can be also expressed in terms of the derivative of the spatial field f with respect to time, as seen by an observer fixed in space. This is done by the chain rule, as follows

$$\frac{Df(\boldsymbol{\chi}(\boldsymbol{X},t),t)}{Dt} = \left(\frac{\partial f(\boldsymbol{\chi}(\boldsymbol{X},\boldsymbol{t}),\boldsymbol{t})}{\partial t}\right)_{\boldsymbol{\chi}} + \left(\frac{\partial f(\boldsymbol{\chi},t)}{\partial \boldsymbol{\chi}}\right)_{t} \cdot \left(\frac{\partial \boldsymbol{\chi}(\boldsymbol{X},t)}{\partial t}\right)_{\boldsymbol{X}}. \tag{2.7}$$

The velocity field $\boldsymbol{v}$ can be defined by the derivative of χ with respect to time. Then, Eq. (2.7) can be rewritten as

$$\frac{Df(\boldsymbol{\chi}(\boldsymbol{X},t),t)}{Dt} = \frac{\partial f}{\partial t} + \boldsymbol{v} \cdot \nabla f, \tag{2.8}$$

which the first term of the right-hand side is known as the local time derivative and the second term is known as the convective derivative. The local time derivative is a measure of the rate at which the field changes at a given point in space, while the convective derivative is a measure of the rate at which the field changes as the particle moves. Notice that eqs. (2.6) and (2.8) are equivalent.

When the field f is the velocity field $vecv$, the material time derivative yields into the acceleration field

$$\frac{D\boldsymbol{v}}{Dt} = \frac{\partial \boldsymbol{v}}{\partial t} + \boldsymbol{v} \cdot \nabla \boldsymbol{v} = \boldsymbol{a}, \tag{2.9}$$

which is important to the understanding of the balance of linear momentum.

2.4 Conservation of Mass

The amount of material a body contains is described by the mass field m. In classical mechanics, mass cannot be produced or destroyed, which means that in a motion, with the absence of sources (reservoirs that supply mass) or sinks (reservoirs that remove mass), the mass field is conserved. In other words, any particle with mass m at the reference configuration will have the same mass at the current configuration

$$m(\Omega_0) = m(\Omega_t) > 0. \tag{2.10}$$

Hence, the material time derivative of the mass field is zero

$$\frac{D}{Dt} m(\Omega_0) = \frac{D}{Dt} m(\Omega_t) = 0. \tag{2.11}$$

The density ρ_0 is defined as the mass per unit volume at the reference configuration, while the density ρ is defined as the mass per unit volume at the current configuration. Note that, while ρ is a function of space and time, ρ_0 is time-independent. In the differential form, the relation between mass and density is given by Eq. (2.12)

$$m = \int_{\Omega_0} \rho_0(\boldsymbol{X}) dV = \int_{\Omega_t} \rho(\boldsymbol{x}, t) dv = const > 0, \tag{2.12}$$

where dV and dv are the volume elements in the reference and current configurations, respectively. The rate of change of mass is given by Eq. (2.13)

$$\frac{Dm}{Dt} = \frac{D}{Dt} \int_{\Omega_0} \rho_0(\boldsymbol{X}) dV = \frac{D}{Dt} \int_{\Omega_t} \rho(\boldsymbol{x}, t) = 0, \tag{2.13}$$

since the density at the reference ρ_0 does not depend on time, Eq. (2.13) yields

$$\frac{D\rho}{Dt} = 0. \tag{2.14}$$

Eq. (2.14) describes the conservation of mass from a material point of view. To obtain the conservation equation from a spatial point of view, the material derivative presented in Eq. (2.7) is employed

$$\frac{D\rho}{Dt} = \frac{\partial \rho}{\partial t} + \nabla \cdot (\rho \boldsymbol{v}) = 0. \tag{2.15}$$

Considering the case in which ρ is constant, Eq. (2.15) yields

$$\nabla \cdot \boldsymbol{v} = 0. \tag{2.16}$$

2.5 Balance of the Linear Momentum

The balance of the linear momentum equation arises from Newton's first and second principles of motion, in the context of continuum mechanics. Let $\boldsymbol{L}(t)$ be the linear momentum of a body at time t, defined by the product of the mass m and velocity $\boldsymbol{v}(\boldsymbol{x}, t)$

$$\boldsymbol{L}(t) = \int_{\Omega_0} \rho_0(\boldsymbol{X}) \boldsymbol{V}(\boldsymbol{X}) dV = \int_{\Omega_t} \rho(\boldsymbol{x}, t) \boldsymbol{v}(\boldsymbol{x}, t) dv. \tag{2.17}$$

Taking the material time derivative of the linear momentum with respect to time yields the resulting force $\boldsymbol{F}(t)$

$$\frac{D\boldsymbol{L}(\boldsymbol{t})}{Dt} = \frac{D}{Dt} \int_{\Omega_0} \rho_0 \boldsymbol{V} dV = \frac{D}{Dt} \int_{\Omega_t} \rho \boldsymbol{v} dv = \boldsymbol{F}(t). \tag{2.18}$$

Next, the forces acting on the surface of the body are considered. Let $\partial\Omega$ be the boundary of the body at any time t, including at the reference moment. The boundary is subject to tractions $\boldsymbol{t}(\boldsymbol{x}, t, \boldsymbol{n}) = \boldsymbol{\sigma n}$, where $\boldsymbol{\sigma}$ is the Cauchy stress tensor and $\boldsymbol{n}$ is the outward unit normal vector. In addition, the continuum is also subject to body forces $\boldsymbol{f}(\boldsymbol{x}, t)$ so that the total external forces $\boldsymbol{F}(t)$ acting on the body is given by Eq. (2.19)

$$\boldsymbol{F}(t) = \int_{\partial\Omega_t} \boldsymbol{t} dA + \int_{\Omega_t} \boldsymbol{f} dv, \tag{2.19}$$

in which dA is the area element of the boundary $\partial\Omega_t$. By applying the divergence theorem, the traction can be rewritten as

$$\int_{\partial\Omega_t} \boldsymbol{t} dA = \int_{\partial\Omega_t} \boldsymbol{\sigma n} dA = \int_{\Omega_t} \nabla \cdot \boldsymbol{\sigma} dv. \tag{2.20}$$

By plugging Eq. (2.20) into eqs. (2.19) and (2.18)

$$\int_{\Omega_t} \left(\frac{D}{Dt} \rho \boldsymbol{v} - \nabla \cdot \boldsymbol{\sigma} + \boldsymbol{f} \right) dv = \boldsymbol{0}, \tag{2.21}$$

which can only be null if the integrand is null. Therefore, the balance of linear momentum is

properly defined by Eq. (2.22)

$$\frac{D}{Dt}\rho\boldsymbol{v} = \nabla\cdot\boldsymbol{\sigma} + \boldsymbol{f}. \tag{2.22}$$

In the case of steady flows, Eq. (2.22) can be rewritten as

$$\nabla\cdot\boldsymbol{\sigma} + \boldsymbol{f} = \boldsymbol{0}. \tag{2.23}$$

2.6 The Piola Transformation

Vectors and tensors quantities can be described in both the reference and current configurations. When a transformation maps vectors from the material to the spatial configuration, it is called a push-forward operation $\boldsymbol{\chi}_*(\cdot)$. The opposite, when a quantity is mapped from the spatial to the material configuration, it is called a pull-back operation $\boldsymbol{\chi}_*^{-1}(\cdot)$.

The Piola transformation is an example of these operations. Let $\boldsymbol{A}$ be a material vector field and $\boldsymbol{a}$ be the spatial vector field, then the Piola transformation is defined as

$$\boldsymbol{A} = J\boldsymbol{\chi}_*^{-1}(\boldsymbol{a}), \tag{2.24}$$

where $\boldsymbol{\chi}_*^{-1}(\cdot) = \boldsymbol{F}^{-1}(\cdot)$, and $\boldsymbol{F}$ is the deformation gradient tensor defined by

$$\boldsymbol{F} = \nabla\boldsymbol{\chi} = \begin{bmatrix} \frac{\partial\chi_1}{\partial X_1} & \frac{\partial\chi_1}{\partial X_2} & \frac{\partial\chi_1}{\partial X_3} \\ \frac{\partial\chi_2}{\partial X_1} & \frac{\partial\chi_2}{\partial X_2} & \frac{\partial\chi_2}{\partial X_3} \\ \frac{\partial\chi_3}{\partial X_1} & \frac{\partial\chi_3}{\partial X_2} & \frac{\partial\chi_3}{\partial X_3} \end{bmatrix}, \tag{2.25}$$

J is the determinant of $\boldsymbol{F}$, also known as the volume ratio or the Jacobian of the transformation and can be seen as a scale factor for the transformation.

It can be shown that the Piola transformation conserves the flux of a vector field between the reference and current configurations. This property is important in the applications of the H(div) approximation spaces used in this work (see Section 3.6.4).

Chapter 3

The Finite Element Method

The Finite Element Method (FEM) is a general procedure to find approximated solutions to Boundary Value Problems (BVPs) governed by Partial Differential Equations (PDEs) [42]. It has emerged from engineering fields based on divide-and-conquer techniques, discretizing the continuum domain into a finite amount of partitions with defined behavior [43]. The system's solution arises from the assembly of each partition, followed by the imposition of Boundary Conditions (BCs) on the previous continuum domain [11]. In the following sections, the basic concepts of the FEM are presented, including the approximation spaces, the weak statement, the Galerkin method, and the shape functions used in the current work.

3.1 Approximation Spaces

In this section, the $\mathrm{L}^2(\Omega)$, $\mathrm{H}^1(\Omega)$, and $\mathrm{H}(\mathrm{div}, \Omega)$ spaces are formally defined, along with their respective inner products and norms.

3.1.1 The Lebesgue Space

For scalar functions u, the $\mathrm{L}^2(\Omega)$ space can be defined by:

$$\mathrm{L}^2(\Omega) = \left\{ u : \int_\Omega u^2 \, d\Omega < \infty \right\}. \tag{3.1}$$

The inner product and norm of the space $\mathrm{L}^2(\Omega)$ are defined respectively by:

$$(u, v)_{\mathrm{L}^2} = (u, v) = \int_\Omega u \, v \, d\Omega, \tag{3.2}$$

$$\|u\|_{\mathrm{L}^2} = \|u\| = (u, u)^{\frac{1}{2}}. \tag{3.3}$$

For vector functions $\boldsymbol{u}$, the $\mathrm{L}^2(\Omega)$ space is defined by

$$\left[\mathrm{L}^2(\Omega)\right]^d = \left\{ \boldsymbol{u} : \int_\Omega \left(\sum_{i=1}^{d} u_i^2 \right)^{\frac{1}{2}} \, d\Omega < \infty \right\}, \tag{3.4}$$

with $d \in \{2, 3\}$ and u_i being the components of the vector function $\boldsymbol{u}$. The respective norm is defined by

$$\|\boldsymbol{u}\|_{[\mathrm{L}^2(\Omega)]^d} = \|\boldsymbol{u}\| = \left(\sum_{i=1}^{d} u_i^2 \right)^{\frac{1}{2}}. \tag{3.5}$$

3.1.2 The Hilbert Space

The $\mathrm{H}^1(\Omega)$ space comprises the functions u of $\mathrm{L}^2(\Omega)$ that have the first derivative square-integrable as well. It is defined by

$$\mathrm{H}^1(\Omega) = \left\{ u \in \mathrm{L}^2(\Omega) : \nabla u \in \left[\mathrm{L}^2(\Omega)\right]^d \right\}. \tag{3.6}$$

Eqs. (3.7) and (3.8) describe the $\mathrm{H}^1(\Omega)$ inner product and norm

$$(u, v)_{\mathrm{H}^1} = (u, v) + (\nabla u, \nabla v), \tag{3.7}$$

$$\|u\|_{\mathrm{H}^1} = \left(\|u\|^2 + \|\nabla u\|^2 \right)^{\frac{1}{2}}. \tag{3.8}$$

3.1.3 The H(div, Ω) Space

In $\mathrm{H}(\mathrm{div}, \Omega)$ spaces, the divergence of a vector function $\boldsymbol{u}$ must be square-integrable

$$\mathrm{H}(\mathrm{div}, \Omega) = \left\{ \boldsymbol{u} \in [\mathrm{L}^2(\Omega)]^d : \nabla \cdot \boldsymbol{u} \in \mathrm{L}^2(\Omega) \right\}. \tag{3.9}$$

The inner product and associated norm are defined as follows:

$$(\boldsymbol{u}, \boldsymbol{v})_{\mathrm{H(div,\,\Omega)}} = (\boldsymbol{u}, \boldsymbol{v}) + (\nabla \cdot \boldsymbol{u}, \nabla \cdot \boldsymbol{v}), \tag{3.10}$$

$$\|\boldsymbol{u}\|_{\mathrm{H(div,\,\Omega)}} = \left(\|\boldsymbol{u}\|^2 + \|\nabla \cdot \boldsymbol{u}\|^2 \right)^{\frac{1}{2}}. \tag{3.11}$$

3.1.4 The H(curl, Ω) Space

The $\mathrm{H}(\mathrm{curl}, \Omega)$ space is defined by

$$\mathrm{H}(\mathrm{curl}, \Omega) = \left\{ \boldsymbol{u} \in [\mathrm{L}^2(\Omega)]^d : \nabla \times \boldsymbol{u} \in \mathrm{L}^2(\Omega) \right\}. \tag{3.12}$$

The inner product and norm of the $\mathrm{H}(\mathrm{curl}, \Omega)$ space are defined by

$$(\boldsymbol{u}, \boldsymbol{v})_{\mathrm{H(curl,\,\Omega)}} = (\boldsymbol{u}, \boldsymbol{v}) + (\nabla \times \boldsymbol{u}, \nabla \times \boldsymbol{v}), \tag{3.13}$$

$$\|\boldsymbol{u}\|_{\mathrm{H(curl,\,\Omega)}} = \left(\|\boldsymbol{u}\|^2 + \|\nabla \times \boldsymbol{u}\|^2\right)^{\frac{1}{2}}. \tag{3.14}$$

3.2 Weak Statement

Let $\Omega \subset \mathbb{R}^d$, $d \in \{2, 3\}$, be a polygonal domain with border $\partial\Omega \subset \mathbb{R}^{d-1}$, $\boldsymbol{n}$ being an unit normal vector pointing outwards Ω, and $\boldsymbol{t}$ the associated tangent vector. The domain is divided into shape-regular partitions $\mathcal{T} = \{\Omega_e, e = 1, ..., N\}$ of Ω, formed by elements Ω_e with usual geometries (triangular, quadrilateral, tetrahedral, hexahedral) and boundary $\partial\Omega_e$.

The mesh skeleton comprises all element edges E that form the set ε. The set of internal edges is denoted by $\varepsilon_0 = \{E \in \varepsilon : E \subset \Omega\}$. To each internal edge, a unit normal $\boldsymbol{n_E}$ and tangent $\boldsymbol{t_E}$ vectors are associated forming a right-hand coordinate system. Over interfaces $E \in \varepsilon_0$ between to consecutive elements Ω_1 and Ω_2, the jump operator of a function v is defined by

$$[\![v]\!] = v_2|_E - v_1|_E, \tag{3.15}$$

in which $v_i = v|_{\Omega_i}$.

Poisson's equation is here used to illustrate how to obtain the weak statement of a model problem. The Poisson problem consists of finding u such that

$$\nabla \cdot \boldsymbol{\sigma} = f \text{ in } \Omega, \tag{3.16}$$

$$\boldsymbol{\sigma} = -K_p \nabla u \text{ in } \Omega, \tag{3.17}$$

$$u = u_D \text{ on } \partial\Omega_D, \tag{3.18}$$

$$\boldsymbol{\sigma n} = \sigma_N \text{ on } \partial\Omega_N, \tag{3.19}$$

in which $\boldsymbol{\sigma}$ is the flux, f is the body force, u is the state variable, u_D is the Dirichlet BC, σ_N is the Neumann BC, and K_p is a scalar. In Darcy's problems K_p is the permeability of the media, in heat conduction it is the conductibility, etc. Note that the boundary $\partial\Omega$ is divided into the Dirichlet $\partial\Omega_D$ and Neumann $\partial\Omega_N$ parts, on which the respective boundary conditions are imposed.

The first step to obtain the weak formulation is to apply the Weighted Residual Method, multiplying the PDE by a test function v and integrating over the domain Ω

$$\int_\Omega \nabla \cdot (\boldsymbol{\sigma}) v \, d\Omega = \int_\Omega f v \, d\Omega, \tag{3.20}$$

using Green's theorem to the left-hand side of Eq. (3.20), and replacing $\boldsymbol{\sigma}$ by its definition, the

weak formulation of the Poisson problem is obtained. The Poisson's problem then reads: find $u \in \mathbb{U} = \{u | u \in \mathrm{H}^1(\Omega), u = u_D \text{ on } \partial\Omega_D\}$ such that

$$\int_\Omega -K_p \nabla u \cdot \nabla v \, d\Omega = \int_\Omega f v \, d\Omega + \int_{\partial\Omega} \sigma_N v \, ds \quad \forall v \in \mathbb{V} \tag{3.21}$$

is satisfied, where $\mathbb{V} = \{v | v \in \mathrm{H}^1(\Omega), v = 0 \text{ on } \partial\Omega_D\}$. The Dirichlet BC is strongly imposed, while the Neumann BC is weakly enforced by the last term of the right-hand side of Eq. (3.21).

3.3 The Galerkin Method

If the weak formulation of Eq. (3.21) is solved for all $v \in \mathbb{V}$, the solution obtained is the same as the one obtained solving the strong form of Eq. (3.17). However, the approximation space $\mathbb{V}$ has an infinite number of basis functions, which makes it computationally unfeasible to solve.

The Galerkin Method proposes a methodology to solve the weak formulation, using no longer the infinite-dimensional space $\mathbb{V}$, but a finite-dimensional subspace. In this context, functions u and v are replaced by their approximations: the trial function u_h and the test function v_h, respectively

$$u \approx u_h = \sum_{i=1}^{n} \alpha_i \phi_i, \quad v \approx v_h = \sum_{j=1}^{n} \beta_j \phi_j, \tag{3.22}$$

where ϕ_i is the set of shape functions of a given approximation space, α_i and β_j are unknown coefficients, and n is the approximation space's number of equations. Replacing Eq. (3.22) in Eq. (3.21) the Poisson's problem weak formulation becomes

$$\sum_{i=1}^{n} \sum_{j=1}^{n} \left(\int_\Omega -K_p \nabla \phi_i \cdot \nabla \phi_j \, d\Omega \right) \alpha_j = \sum_{i=1}^{n} \int_\Omega \phi_i f \, d\Omega + \int_{\partial\Omega_N} \phi_i \sigma_N \, ds \quad \forall \phi_i \in \mathbb{V}. \tag{3.23}$$

The original PDE is now transformed into a linear system. Eq (3.23) can be written in a matrix form as:

$$\mathbf{K}\boldsymbol{\alpha} = \mathbf{f}, \tag{3.24}$$

in which the stiffness matrix coefficients $\mathbf{K}_{ij}$, the unknown coefficients α_i, and the load vector coefficients $\mathbf{f}_i$ are defined as follows

$$\begin{aligned}
\mathbf{K}_{ij} &= \sum_{i=1}^{n} \sum_{j=1}^{n} \left(\int_\Omega -K_p \nabla \phi_i \cdot \nabla \phi_j \, d\Omega \right), \\
\boldsymbol{\alpha} &= \left[\alpha_i, \alpha_{i+1}, ..., \alpha_n \right]^T, \\
\mathbf{f} &= \left[\sum_{i=1}^{n} \int_\Omega \phi_i f \, d\Omega + \int_{\partial\Omega_N} \phi_i \sigma_N \, ds \right]^T.
\end{aligned}$$

One key characteristic of the Galerkin Method is that it proposes to approximate both the trial and test functions using the same set of basis functions. This fact assigns to the stiffness matrix important properties, such as symmetry. Ultimately, the solution for the coefficients α can be found by solving the linear system of Eq. (3.24), and the solution to the original BVP can be evaluated once the coefficients are known (Eq. (3.22)).

Naturally, the quality of the solution depends directly on the choice of the approximation space. FEM is applied to provide a systematic technique to construct the shape functions for Galerkin approximations.

3.4 Master and Deformed Elements

As previously discussed, the strong form of a BVP is turned into a linear system that represents the weak formulation approximated by the Galerkin Method. The stiffness matrix is obtained through the evaluation of integrals defined over the element domain. However, each element has a different domain, which makes it difficult to propose a set of shape functions ϕ that can be generically applied to all elements.

A way to overcome this issue is to map the element domain Ω_e into a master element domain $\hat{\Omega}$, using linear transformations. Over the master element, the integrals are no longer evaluated in the cartesian coordinates system (x, y, z), instead, they are evaluated in the parametric coordinates system (ξ, η, ζ). Figure 3.1 illustrates both linear transformations $T_e : \hat{\Omega} \rightarrow \Omega_e$, and $T_e^{-1} : \Omega_e \rightarrow \hat{\Omega}$.

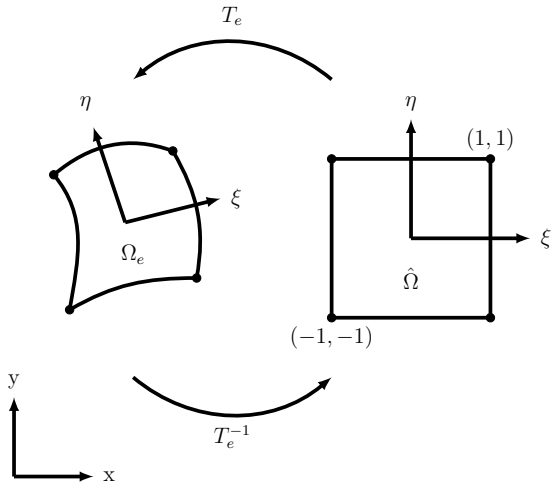

Figure 3.1: Geometrical transformations T_e and T_e^{-1}.

These linear transformations are defined in three dimensions as follows:

$$T_e : \begin{cases} x = x(\xi, \eta, \zeta) \\ y = y(\xi, \eta, \zeta) \\ z = z(\xi, \eta, \zeta) \end{cases} \quad ; \quad T_e^{-1} : \begin{cases} \xi = \xi(x, y, z) \\ \eta = \eta(x, y, z) \\ \zeta = \zeta(x, y, z) \end{cases} , \tag{3.25}$$

along with the mapping function:

$$x = \sum_{n=1}^{nF} x_i \hat{\phi}_i(\xi, \eta, \zeta); \qquad y = \sum_{n=1}^{nF} y_i \hat{\phi}_i(\xi, \eta, \zeta), \qquad z = \sum_{n=1}^{nF} z_i \hat{\phi}_i(\xi, \eta, \zeta), \tag{3.26}$$

in which x_i, y_i, and z_i are the nodal coordinates of the deformed element related to the shape function $\hat{\phi}_i$ defined in the master element, and nF is the number of functions defined over the master element used in the mapping function. Unless it is said otherwise, the mapping function used in this work only considers linear shape functions. More information about the set of shape functions can be found in Section 3.6.

Triangular and quadrilateral master elements are depicted in Figure 3.2,

Figure 3.2: Triangle and Quadrilateral master elements.

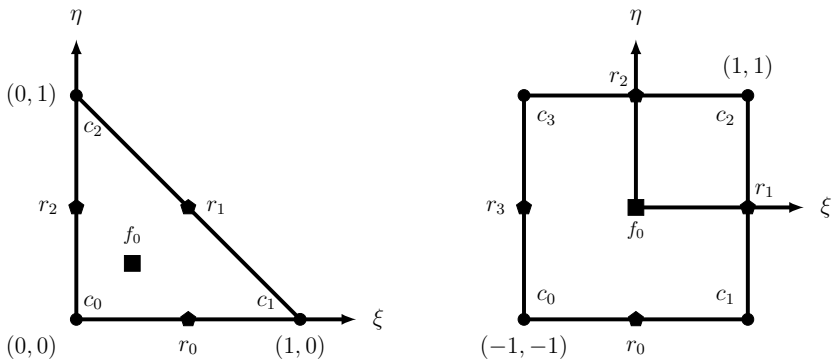

in which, circles illustrate the vertices, pentagons the edges, and squares the faces. In three-dimensional elements, there is also the volume. All these master elements' characteristics are, herein, called "sides". In this work, triangle, quadrilateral, tetrahedral, and hexahedral elements are considered, of which master element's geometry is defined by [44] as follows:

- for triangles: $\hat{\Omega} = \{(\xi, \eta);\ \xi \geq 0,\ \eta \geq 0,\ \xi + \eta \leq 1\}$;
- for quadrilaterals: $\hat{\Omega} = [-1, 1] \times [-1, 1]$;
- for tetrahedral: $\hat{\Omega} = \{(\xi, \eta, \zeta);\ \xi \geq 0,\ \eta \geq 0,\ \zeta \geq 0,\ \xi + \eta + \zeta \leq 1\}$;
- for hexahedral: $\hat{\Omega} = [-1, 1] \times [-1, 1] \times [-1, 1]$;

3.5 Numerical Integration

Numerical integration is used to evaluate the stiffness matrix, load vector, and compute error. The Gaussian Quadrature

$$\int_{\Omega} f(x, y, z)\, d\Omega \approx \sum_{i=1}^{nPoints} |det(\boldsymbol{J})| f(\boldsymbol{x}(\xi_i, \eta_i, \zeta_i)) w_i, \tag{3.27}$$

is employed in this framework to integrate quadrilateral and hexahedral elements. In Eq. (3.27), $nPoints$ is the Gaussian Quadrature number of points for a given polynomial order with respective weights w_i, f is the function to be integrated, (x, y, z) are the cartesian coordinates, (ξ, η, ζ) are the parametric coordinates, and $det(\boldsymbol{J})$ is the determinant of the Jacobian matrix $\boldsymbol{J}$ defined as

$$\boldsymbol{J} = \begin{bmatrix} \frac{\partial x}{\partial \xi} & \frac{\partial x}{\partial \eta} & \frac{\partial x}{\partial \zeta} \\ \frac{\partial y}{\partial \xi} & \frac{\partial y}{\partial \eta} & \frac{\partial y}{\partial \zeta} \\ \frac{\partial z}{\partial \xi} & \frac{\partial z}{\partial \eta} & \frac{\partial z}{\partial \zeta} \end{bmatrix}. \tag{3.28}$$

For triangular elements, the Hammer Quadrature detailed in [45] is used.

3.6 Shape Functions

Shape functions are composed according to the approximation space, the element type, and the polynomial approximation order. The following sections discuss the particularities of $\mathrm{H}^1(\Omega)$ and $\mathrm{H}(\mathrm{div}, \Omega)$ approximation spaces.

3.6.1 $\mathrm{H}^1(\Omega)$-conforming Scalar Shape Functions

A systematic way to construct shape functions for $\mathrm{H}^1(\Omega)$-conforming spaces is proposed by [44]. The shape functions employed by NeoPZ are hierarchical, rather than Lagrangian. Hierarchical functions consider all the polynomial orders up to a given k in a single set of shape functions, while Lagrangian functions consider only the polynomial order k. In the literature, other types of shape functions can be found. To obtain an approximation space of continuous functions, the authors enumerate the following properties:

1. A shape function cannot be associated with two or more sides of the same element;
2. A side of non-null dimension has zero or more shape functions associated with it;
3. A shape function related to a side of dimension d is non-zero on this side and null on any other side of dimension $< d$;
4. Each shape function of a given element is associated with its sides.

Taking these properties into account, the shape functions can be divided into four categories: vertex, edge, face, and internals. Each one of them is briefly commented below.

- **Vertex Shape Functions:** denoted by $\hat{\phi}_{ci}$. They are composed of Lagrangian first-order shape functions. Unitary on the vertex c_i and null on any other vertex, edges, and faces not sharing the vertex c_i.

- **Edge Shape Functions:** denoted by $\hat{\phi}^n_{r_i}$. Non-zero on the edge r_i. They vanish in all other edges and faces not sharing the edge r_i;
- **Face Shape Functions:** denoted by $\hat{\phi}^{n_0,n_1}_{f_i}$. Non-zero on the face f_i. They are null on all other faces not sharing the face f_i;
- **Volume Shape Functions:** denoted by $\hat{\phi}^{n_0,n_1,n_2}_{v_i}$. They vanish in all vertices, edges, and faces.

• Triangle Elements

Consider the triangle master element depicted in Figure 3.2. For a given polynomial approximation order k, the number of shape functions associated with this element can be seen in Table 3.1.

Table 3.1: Number of $\mathrm{H}^1(\Omega)$-conforming shape functions on triangular elements.

Side Type	Number of Shape Functions
Vertex	3
Edge	$3(k-1)$ with $k \geq 2$
Face	$\frac{(k-2)(k-1)}{2}$ with $k \geq 3$

- Vertex functions $\hat{\phi}_{c_i}$:

$$\hat{\phi}_{c_0}(\xi,\eta) = 1-\xi-\eta, \qquad \hat{\phi}_{c_1}(\xi,\eta) = \xi, \qquad \hat{\phi}_{c_2}(\xi,\eta) = \eta. \tag{3.29}$$

- Edge functions $\hat{\phi}^n_{r_i}$:

$$\begin{aligned}
\hat{\phi}^n_{r_0}(\xi,\eta) &= \hat{\phi}_{c_0}(\xi,\eta)\hat{\phi}_{c_1}(\xi,\eta)f_n(\eta+2\xi-1),\\
\hat{\phi}^n_{r_1}(\xi,\eta) &= \hat{\phi}_{c_1}(\xi,\eta)\hat{\phi}_{c_2}(\xi,\eta)f_n(\eta-\xi),\\
\hat{\phi}^n_{r_2}(\xi,\eta) &= \hat{\phi}_{c_2}(\xi,\eta)\hat{\phi}_{c_0}(\xi,\eta)f_n(1-2\eta-\xi),
\end{aligned} \tag{3.30}$$

for $n = 0, ..., k-2$.

- Face functions $\hat{\phi}^{n_0,n_1}_{f_0}$:

$$\hat{\phi}^{n_0,n_1}_{f_0}(\xi,\eta) = \hat{\phi}_{c_0}(\xi,\eta)\hat{\phi}_{c_1}(\xi,\eta)\hat{\phi}_{c_2}(\xi,\eta)f_{n_0}(2\xi-1)f_{n_1}(2\eta-1), \tag{3.31}$$

where $f_n(\cdot) = \cos(n\ arccos(\cdot))$ are the Chebychev polynomials, in which $0 < n_0+n_1 < k-3$.

• Quadrilateral Elements

Consider now, the quadrilateral master element in Figure 3.2. The numbers of its shape functions, for a given k, are listed in Table 3.2.

Table 3.2: Number of $H^1(\Omega)$-conforming shape functions on quadrilateral elements.

Side Type	Number of Shape Functions
Vertex	4
Edge	$4(k-1)$, with $k \geq 2$
Face	$(k-1)^2$, with $k \geq 2$

- Vertex functions $\hat{\phi}_{c_i}$:

$$\begin{aligned} \hat{\phi}_{c_0}(\xi,\eta) &= \frac{(1-\xi)(1-\eta)}{4}, \qquad \hat{\phi}_{c_1}(\xi,\eta) = \frac{(1+\xi)(1-\eta)}{4}, \\ \hat{\phi}_{c_2}(\xi,\eta) &= \frac{(1+\xi)(1+\eta)}{4}, \qquad \hat{\phi}_{c_3}(\xi,\eta) = \frac{(1-\xi)(1+\eta)}{4}. \end{aligned} \tag{3.32}$$

- Edge functions $\hat{\phi}_{r_i}$:

$$\begin{aligned} \hat{\phi}^n_{r_0}(\xi,\eta) &= 4\hat{\phi}_{c_0}(\xi,\eta)[\hat{\phi}_{c_1}(\xi,\eta) + \hat{\phi}_{c_2}(\xi,\eta)]f_n(\xi), \\ \hat{\phi}^n_{r_1}(\xi,\eta) &= 4\hat{\phi}_{c_1}(\xi,\eta)[\hat{\phi}_{c_2}(\xi,\eta) + \hat{\phi}_{c_3}(\xi,\eta)]f_n(\eta), \\ \hat{\phi}^n_{r_2}(\xi,\eta) &= 4\hat{\phi}_{c_2}(\xi,\eta)[\hat{\phi}_{c_3}(\xi,\eta) + \hat{\phi}_{c_0}(\xi,\eta)]f_n(-\xi), \\ \hat{\phi}^n_{r_3}(\xi,\eta) &= 4\hat{\phi}_{c_3}(\xi,\eta)[\hat{\phi}_{c_0}(\xi,\eta) + \hat{\phi}_{c_1}(\xi,\eta)]f_n(-\eta), \end{aligned} \tag{3.33}$$

for $n = 0, ..., k-2$.

- Face functions $\hat{\phi}_{f_i}$:

$$\hat{\phi}^{n_0,n_1}_{f_0} = 16\hat{\phi}_{c0}(\xi,\eta)\hat{\phi}_{c_2}(\xi,\eta)f_{n_0}(\xi)f_{n_1}(\eta), \tag{3.34}$$

in which $0 < n_0, n_1 < k-2$.

For hexahedral elements, the number of scalar shape functions for $H^1(\Omega)$-conforming spaces is given by Table 3.3.

Table 3.3: Number of $H^1(\Omega)$-conforming shape functions on hexahedral elements.

Side Type	Number of Shape Functions
Vertex	8
Edge	$12(k-1)$, with $k \geq 2$
Face	$6(k-1)^2$, with $k \geq 2$
Volume	$(k-1)^2$, with $k \geq 2$

The creation of three-dimensional elements is similar to the process aforementioned. More details of the shape functions for tetrahedral and hexahedral elements can be found in Sections

4.4 and 4.7 of [44], respectively. Table 3.4 summarizes the set of shape functions for $\mathrm{H}^1(\Omega)$-conforming spaces in two- and three-dimensional elements.

Table 3.4: Set of shape functions for $\mathrm{H}^1(\Omega)$-conforming spaces.

Element dimension	Shape Functions
2D	$\hat{\phi}_{c_i}$, $\hat{\phi}_{r_i}$, $\hat{\phi}_{f_i}$
3D	$\hat{\phi}_{c_i}$, $\hat{\phi}^n_{r_i}$, $\hat{\phi}_{f_i}$, $\hat{\phi}_{v_i}$

in which $\hat{\phi}_{v_i}$ is the volume shape function.

3.6.2 H(div, Ω) Hierarchical Vector Shape Functions

The creation of two- and three-dimensional hierarchical vector shape functions for $\mathrm{H}(\mathrm{div}, \Omega)$ spaces adopted in this work is proposed in [32, 33]. Since the procedures for two and three dimensions are different, they are treated separately.

• Two-Dimensional Vector Fields at Master Element

The creation of $\mathrm{H}(\mathrm{div}, \Omega)$ space shape functions proposed by [32] is based on the multiplication of scalar shape functions by vector fields. To each side, two vectors are connected. These vectors can be defined using the canonical orthonormal vectors $\boldsymbol{e_1} = \{1, 0, 0\}$, $\boldsymbol{e_2} = \{0, 1, 0\}$, and $\boldsymbol{e_3} = \{0, 0, 1\}$. Figure 3.3 depicts the two-dimensional vector fields associated with the creation of $\mathrm{H}(\mathrm{div}, \Omega)$ shape functions.

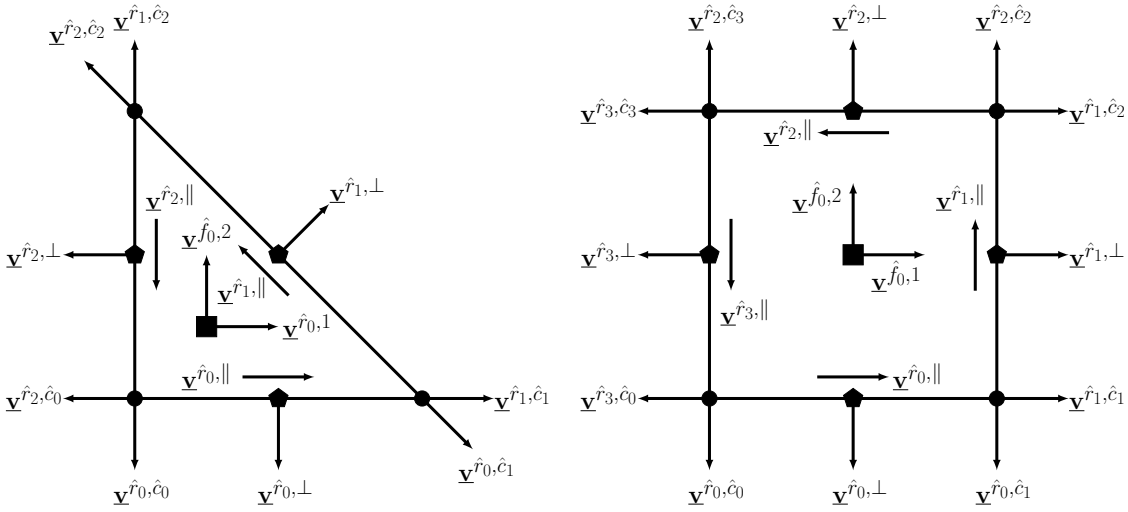

Figure 3.3: Vector fields at two-dimensional reference elements.

For two dimensions, vector fields $\underline{\mathbf{v}}$ can be defined as follows:

1. $\underline{\mathbf{v}}^{\hat{r}_i,\hat{c}_j}$ - vectors associated with a vertex $\hat{c}_j$ on the edge $\hat{r}_i$. Each $\underline{\mathbf{v}}^{\hat{r}_i,\hat{c}_j}$ should be aligned to the adjacent edge, that also shares the vertex $\hat{c}_j$.

2. $\underline{\mathbf{v}}^{\hat{r}_i,\perp}$ - an outward normal vector to the edge r_i;

3. $\underline{\mathbf{v}}^{\hat{r}_i,\parallel}$ - tangent to the edge r_i;

4. $\underline{\mathbf{v}}^{\hat{f}_0,i}$, with $i = \{1, 2\}$ - the orthonormal vectors e_i associated with the face $\hat{f}_0$.

Sets 1 and 2 listed above configure the so-called "Edge vectors" and, thus, are responsible for creating the edge shape functions of the $\mathrm{H}(\mathrm{div}, \Omega)$ space. Sets 3 and 4, conversely, are called "Internal Vectors" and generate the internal shape functions, i.e., functions without normal components.

• Two-Dimensional Elements

For both triangle and quadrilateral elements, the $\mathrm{H}(\mathrm{div}, \Omega)$ generation process of shape functions is the same, the product of scalar $\mathrm{H}^1(\Omega)$ shape functions and $\underline{\mathbf{v}}$, as follows.

- **Edge Functions:**

$$\hat{\boldsymbol{\phi}}^{\hat{r}_i,\hat{c}_j} = \hat{\phi}_{\hat{c}_j}\, \underline{\mathbf{v}}^{\hat{r}_i,\hat{c}_j}, \tag{3.35}$$

$$\hat{\boldsymbol{\phi}}^{\hat{r}_i,n} = \hat{\phi}^n_{\hat{r}_i}\, \underline{\mathbf{v}}^{\hat{r}_i,\perp}. \tag{3.36}$$

For Eq. (3.35), it is mandatory to verify that, if $\hat{c}_j$ is a vertex of $\hat{r}_k$ and $\hat{r}_i \neq \hat{r}_k$, with $\hat{r}_i$ adjacent to $\hat{r}_k$, then the product $\hat{\boldsymbol{\phi}}^{\hat{r}_k,\hat{c}_j} \cdot \boldsymbol{n}_k$ shall be null. Over the edge $\hat{r}_i$, the normal component is $\hat{\boldsymbol{\phi}}^{\hat{r}_i,\hat{c}_j} \cdot \boldsymbol{n}_i = \hat{\phi}_{c_i}$. Eq. (3.36) vanishes at any $\hat{r}_k \neq \hat{r}_i$ and has normal component equal to $\hat{\boldsymbol{\phi}}^{\hat{r}_i,n} \cdot \boldsymbol{n}_i = \hat{\phi}^n_{\hat{r}_i}$.

- **Internal Functions:**

$$\hat{\boldsymbol{\phi}}^{\hat{f}_0,\hat{r}_i,n} = \hat{\phi}^n_{\hat{r}_i}\, \underline{\mathbf{v}}^{\hat{r}_i,\parallel}, \tag{3.37}$$

$$\hat{\boldsymbol{\phi}}^{\hat{f}_0,n_0,n_1}_i = \hat{\phi}^{n_0,n_1}_{\hat{f}_0}\, \underline{\mathbf{v}}^{\hat{f}_0,i}. \tag{3.38}$$

For any edge $\hat{r}_k \neq \hat{r}_i$, Eq. (3.37) vanishes. Over the edge $\hat{r}_i$, its normal component shall be null. On every edge of the face $\hat{f}_0$, Eq. (3.38) vanishes. There exist $(k+1)(k+2)$, and $2(k+1)^2$ shape functions in a triangular and quadrilateral, respectively. To these sets, are added functions of which the divergence has the same polynomial order as k. $\mathrm{H}(\mathrm{div}, \Omega)$ functions have continuous normal components across element interfaces [46].

• Three-Dimensional Vector Fields at Master Element

The creation of $\mathrm{H}(\mathrm{div}, \Omega)$ shape functions for three-dimensional elements is proposed by [33]. The vector fields are defined as follows

1. $\underline{\mathbf{v}}^{\hat{f}_i,\hat{c}}$ - vectors associated with the vertices $\hat{c}$ of face $\hat{f}_i$;

2. $\underline{\mathbf{v}}^{\hat{f}_i,\hat{r}}$ - vectors associated with the edges $\hat{r}$ of face $\hat{f}_i$;

3. $\underline{\mathbf{v}}^{\hat{f}_i,\perp}$ - normal vector associated with the face $\hat{f}_i$;

4. $\underline{\mathbf{v}}^{\hat{r}_i,\parallel}$ - aligned vectors to the edge $\hat{r}_i$;

5. $\underline{\mathbf{v}}_j^{\hat{f}_i,\parallel}$, with $j = \{1, 2\}$ - tangent vectors to the face $\hat{f}_i$;

6. $\underline{\mathbf{v}}_j^{\hat{v}_i}$, with $j = \{1, 2, 3\}$ - orthonormal vectors e_j associated with the volume $\hat{v}$.

Sets 1, 2, and 3 listed above configure the face vector field. Thus they are responsible for creating the face shape functions for the $\mathrm{H}(\mathrm{div}, \Omega)$ space. Sets 4, 5, and 6, conversely, compose the internal vector field and generate the internal shape functions, i.e., functions without normal components.

• Three-Dimensional Elements

The process of creation for three-dimensional elements is similar to the two-dimensional case. The multiplication of scalar $\mathrm{H}^1(\Omega)$ shape functions and $\underline{\mathbf{v}}$ is performed as follows.

- **Face Functions:**

$$\hat{\boldsymbol{\phi}}^{\hat{f}_i,\hat{c}} = \hat{\phi}_{\hat{c}}\ \underline{\mathbf{v}}^{\hat{f}_i,\hat{c}}, \tag{3.39}$$

$$\hat{\boldsymbol{\phi}}^{\hat{f}_i,\hat{r},n} = \hat{\phi}^n_{\hat{r}}\ \underline{\mathbf{v}}^{\hat{f}_i,\hat{r}}, \tag{3.40}$$

$$\hat{\boldsymbol{\phi}}^{\hat{f}_i,n_0,n_1} = \hat{\phi}^{n_0,n_1}_{\hat{f}_i}\ \underline{\mathbf{v}}^{\hat{f}_i,\perp}. \tag{3.41}$$

The normal component of Eq. (3.39), vanishes at any face $\hat{f}_k \neq \hat{f}_i$ that shares the vertex $\hat{c}$. Over the face $\hat{f}_i$, the normal component is $\hat{\boldsymbol{\phi}}^{\hat{f}_i,\hat{c}} \cdot \boldsymbol{n}_i = \hat{\phi}_{\hat{c}}$. In faces whose edges do not include $\hat{r}_i$ Eq. (3.40) vanishes. The normal component of Eq. (3.40) is $\hat{\boldsymbol{\phi}}^{\hat{f}_i,\hat{r},n} \cdot \boldsymbol{n}_i = \hat{\phi}^n_{\hat{r}}$. Eq. (3.41) vanishes at any face $\hat{f}_k \neq \hat{f}_i$ and over face $\hat{f}_i$ has normal component equal to $\hat{\boldsymbol{\phi}}^{\hat{f}_i,n_0,n_1} \cdot \boldsymbol{n}_i = \hat{\phi}^{n_0,n_1}_{\hat{f}_i}$.

- **Internal Functions:**

$$\hat{\boldsymbol{\phi}}^{\hat{v}_i,\hat{r},n} = \hat{\phi}^n_{\hat{r}}\ \underline{\mathbf{v}}^{\hat{r},\parallel}, \tag{3.42}$$

$$\hat{\boldsymbol{\phi}}_j^{\hat{v}_i,\hat{f},n_0,n_1} = \hat{\phi}_{\hat{f}}\ \underline{\mathbf{v}}_j^{\hat{f},\parallel}, \tag{3.43}$$

$$\hat{\boldsymbol{\phi}}_j^{\hat{v}_i,n_0,n_1,n_2} = \hat{\phi}^{n_0,n_1,n_2}_{\hat{v}_i}\ \underline{\mathbf{v}}_j^{\hat{v}_i}. \tag{3.44}$$

On all edges that do not share the edge $\hat{r}_i$, Eq. (3.42) vanishes. Over the edge $\hat{r}_i$, the normal component is null. Eq. (3.44) vanishes on all faces of the volume $\hat{v}_i$.

Table 3.5 summarizes the set of shape functions for $\mathrm{H}(\mathrm{div}, \Omega)$ spaces in two- and three-dimensional elements. More details about the creation of $\mathrm{H}(\mathrm{div}, \Omega)$ shape functions for three-dimensional elements can be found in Appendix A of [33].

Table 3.5: Set of shape functions for $\mathrm{H}(\mathrm{div}, \Omega)$ spaces.

Element dimension	Shape Functions
2D	$\hat{\boldsymbol{\phi}}^{\hat{r}_i,\hat{c}_j}$, $\hat{\boldsymbol{\phi}}^{\hat{r}_i,n}$, $\hat{\boldsymbol{\phi}}^{\hat{f}_0,\hat{r}_i,n}$, $\hat{\boldsymbol{\phi}}_i^{\hat{f}_0,n_0,n_1}$
3D	$\hat{\boldsymbol{\phi}}^{\hat{f}_i,\hat{c}}$, $\hat{\boldsymbol{\phi}}^{\hat{f}_i,\hat{r},n}$, $\hat{\boldsymbol{\phi}}^{\hat{f}_i,n_0,n_1}$, $\hat{\boldsymbol{\phi}}^{\hat{v}_i,\hat{r},n}$, $\hat{\boldsymbol{\phi}}_j^{\hat{v}_i,\hat{f},n_0,n_1}$, $\hat{\boldsymbol{\phi}}_j^{\hat{v}_i,n_0,n_1,n_2}$

The hierarchical $\mathrm{H}(\mathrm{div}, \Omega)$ space created following the aforementioned procedure is herein called Hdiv-S (refers to [32, 33] for deeper pieces of information). One goal of this work is to compare the performance of the Hdiv-S space with a constant divergence space, herein called Hdiv-C. The next section explains how the Hdiv-C space is created.

3.6.3 A Constant Divergence H(div, Ω) Space

The Hdiv-C space is introduced in Section 3 of [34]. It is created from the De Rham exact sequence theory, which is defined for two and three dimensions by eqs. (3.45) and (3.46), respectively

$$\mathbb{R} \rightarrow \mathrm{H}^1(\Omega) \xrightarrow{\nabla\times} \mathrm{H}(\mathrm{div}, \Omega) \xrightarrow{\nabla\cdot} \mathrm{L}^2(\Omega) \rightarrow \{0\}, \tag{3.45}$$

$$\mathbb{R} \rightarrow \mathrm{H}^1(\Omega) \xrightarrow{\nabla} \mathrm{H}(\mathrm{curl}, \Omega) \xrightarrow{\nabla\times} \mathrm{H}(\mathrm{div}, \Omega) \xrightarrow{\nabla\cdot} \mathrm{L}^2(\Omega) \rightarrow \{0\} \tag{3.46}$$

where, for two-dimensional scalar functions, the curl operator is also known as the rotated gradient operator.

Let ϕ^{H^1} be a scalar function in the $\mathrm{H}^1(\Omega)$ space, $\boldsymbol{\phi}^{\mathrm{hcurl}}$ a vector function in $\mathrm{H}(\mathrm{curl}, \Omega)$, $\boldsymbol{\phi}^{\mathrm{hdiv}}$ a vector function in $\mathrm{H}(\mathrm{div}, \Omega)$, and ϕ^{L^2} a scalar function in $\mathrm{L}^2(\Omega)$. Then the following relations are valid

$$\{\nabla\phi^{\mathrm{H}^1}\} = \{\boldsymbol{\phi}^{\mathrm{hcurl}} | \nabla \times \boldsymbol{\phi}^{\mathrm{hcurl}} = \mathbf{0}\} \tag{3.47}$$

$$\{\nabla \times \boldsymbol{\phi}^{\mathrm{hcurl}}\} = \{\boldsymbol{\phi}^{\mathrm{hdiv}} | \nabla \cdot \boldsymbol{\phi}^{\mathrm{hdiv}} = 0\} \tag{3.48}$$

$$\{\nabla \cdot \boldsymbol{\phi}^{\mathrm{hdiv}}\} = \{\phi^{\mathrm{L}^2}\} \tag{3.49}$$

Taking these relations into account, the procedures for creating the Hdiv-C space for two- and three-dimensional functions are explained. For two dimensions, the rotated gradient of $\mathrm{H}^1(\Omega)$ functions is taken as the basis for the $\mathrm{H}(\mathrm{div}, \Omega)$ space. The edge functions of the just created $\mathrm{H}(\mathrm{div}, \Omega)$ space are then replaced by RT0 functions (Ravian-Tomas zero order) [47], which leads to a constant divergence space.

For three dimensions, the space $\mathrm{H}(\mathrm{curl}, \Omega)$ by multiplying the $\mathrm{H}^1(\Omega)$ functions by the tangent vector field of the faces. From the $\mathrm{H}(\mathrm{curl}, \Omega)$ functions, those that have zero divergence are filtered out, leading to the creation of the $\mathrm{H}(\mathrm{div}, \Omega)$ space. The face functions are then replaced by the RT0 functions, which are constant by element.

An advantage of this procedure is that all functions of $\mathrm{H}(\mathrm{div}, \Omega)$ with divergence equal to zero are obtained directly from the $\mathrm{H}(\mathrm{curl}, \Omega)$ functions. Moreover, the De Rham exact

sequence allows the creation of approximation spaces for higher polynomial orders.

Divergence-free problems, such as the Stokes equations for incompressible fluids, can be approximated with a very efficient constant $\mathrm{H}(\mathrm{div}, \Omega)$ basis. The Hdiv-C space is key for optimizing the iterative methods for solving the global system of equations.

3.6.4 H(div, Ω) Shape Functions with Piola Transformation

The current work employs $\mathrm{H}(\mathrm{div}, \Omega)$ spaces to interpolate velocity and solve the Stokes equations. One of the main characteristics of $\mathrm{H}(\mathrm{div}, \Omega)$ spaces is that only the normal component of the velocity is continuous across elements. The linear transformation presented in Section 3.4, however, is not able to conserve normal components in vector fields such as $\mathrm{H}(\mathrm{div}, \Omega)$.

To overcome this issue, the Piola Transformation (see Section 2.6) is employed to map the shape functions evaluated in the master element to the deformed element.

$$T^{div} : \boldsymbol{\phi} = \frac{1}{|\det(\boldsymbol{J})|} \boldsymbol{J} \hat{\boldsymbol{\phi}}. \tag{3.50}$$

in which J is the Jacobian matrix of the transformation.

Moreover, it is verified that, for vector fields mapped by Eq. (3.50), the following property is also valid [46]

$$\nabla \cdot \boldsymbol{\phi} = \frac{1}{|\det(\boldsymbol{J})|} \nabla \cdot \hat{\boldsymbol{\phi}}. \tag{3.51}$$

3.7 Static Condensation

Static condensation is a method that aims to reduce the size of linear systems by condensing the number of Degrees of Freedom (DoF) of the system. The term was first employed to condense the DoF of statical structural analysis, grouping the equations into different subsets [48, 49].

Let α_i be linear coefficients related to internal shape functions, which are associated with one element without interacting with other elements; and the coefficients α_e, conversely, being related to shape functions that interact between elements. In this context, the static condensation as proposed by [50] compacts and solves the linear system of Eq. (3.52)

$$\left(\begin{array}{c|c} K_{ii} & K_{ie} \\ \hline K_{ei} & K_{ee} \end{array}\right) \left\{\begin{array}{c} \alpha_i \\ \hline \alpha_e \end{array}\right\} = \left\{\begin{array}{c} F_i \\ \hline F_e \end{array}\right\}, \tag{3.52}$$

where the stiffness matrix in Eq. (3.24) is divided into four submatrices: K_{ii}, K_{ie}, K_{ei}, and K_{ee}, and the load vector is divided into F_i and F_e, according to internal and external DoFs (see Section 4.4 for more details).

By isolating α_i yields to Eq. (3.53)

$$\alpha_i = K_{ii}^{-1}(F_i - K_{ie}\alpha_e), \tag{3.53}$$

and replacing α_i in the second equation of Eq. (3.52), the condensed system is obtained as shown in Eq. (3.54)

$$\underbrace{(K_{ee} - K_{ei}K_{ii}^{-1}K_{ie})}_{K^*}\,\alpha_e = \underbrace{F_e - K_{ei}K_{ii}^{-1}F_i}_{F^*}, \tag{3.54}$$

in which K^* is the condensed stiffness matrix, and F^* is the condensed load vector.

It is noted that the global system of equations has a smaller number of equations. The procedure can lead to a significant decrease in computational time during the solver step.

3.8 The Penalty Method

Let B be a big number, significantly greater than the entries in the stiffness matrix, but not big enough to compromise numerical stability. Then this big number B can be used to impose the Dirichlet BC [51].

Imposing a Dirichlet BC, the weak formulation for Poisson's problem reads: find $u \in \mathbb{U}$ such that

$$\int_\Omega -K_p \nabla u \cdot \nabla v \, d\Omega + B \int_{\partial\Omega_D} uv \, ds = \int_\Omega fv \, d\Omega + \int_{\partial\Omega} \sigma_N v \, ds + B \int_{\partial\Omega_D} u_D v \, ds, \tag{3.55}$$

is satisfied. It is noted that the stiffness matrix remains symmetric after the penalty method is applied.

Chapter 4

The Stokes Equations

In this chapter, the Stokes equations are presented. The problem statement is formalized, and its weak formulation is derived. Three mixed formulations with different FEM approaches to solving the Stokes equations are discussed: the Taylor-Hood element, the semi-hybrid, and the hybrid-hybrid method. For the last two, the local mass conservation is discussed.

4.1 The Problem Statement

The motion of a fluid flow can be defined, in a general way, by the Navier-Stokes equations, composed of a balance of momentum (Eq. (4.1)) and a mass conservation equation (Eq. (4.2)), in which ρ is the fluid density; ∂_t the partial derivative with respect to time; $\boldsymbol{u}$ the velocity vector field; μ the fluid viscosity; p the fluid pressure; and $\boldsymbol{f}$ the body forces. It can be employed to solve problems in the fields of aeronautical engineering, the petroleum industry, and even biological studies in problems such as the bloodstream flow [52].

$$\overbrace{\rho(\underbrace{\partial_t \boldsymbol{u}}_{\text{Variation}} + \underbrace{\boldsymbol{u}\cdot\nabla\boldsymbol{u}}_{\text{Convection}})}^{\text{Inertial Terms}} - \overbrace{\underbrace{\mu\Delta\boldsymbol{u}}_{\text{Diffusion}} + \underbrace{\nabla p}_{\text{Internal Source}}}^{\text{Divergence of stress}} = \overbrace{\boldsymbol{f}}^{\text{Source Terms}}, \tag{4.1}$$

$$\partial_t \rho + \rho\nabla\cdot(\boldsymbol{u}) = 0. \tag{4.2}$$

The convection term configures the nonlinearity of the Navier-Stokes problem. If the flow is said to be in a steady state, then velocity does not vary over time. For flows with a very low Reynolds number, the convection parcel can be neglected. Knowing that the flow is incompressible, the density is constant and therefore does not vary over time as well. These assumptions simplify the Navier-Stokes equations into the Stokes equations reads: find the velocity $\boldsymbol{u}$ and

the pressure p such that:

$$-\nabla \cdot \boldsymbol{\sigma} = \boldsymbol{f} \text{ in } \Omega, \tag{4.3}$$

$$\nabla \cdot \boldsymbol{u} = 0 \text{ in } \Omega, \tag{4.4}$$

$$\boldsymbol{u} = \boldsymbol{u_D} \text{ on } \partial\Omega_D, \tag{4.5}$$

$$\boldsymbol{\sigma n} = \boldsymbol{\sigma_N} \text{ on } \partial\Omega_N. \tag{4.6}$$

Eq. (4.3) represents the divergence of the Cauchy stress, whose constitutive law is given by Eq. (4.7)

$$\boldsymbol{\sigma} = 2\mu\boldsymbol{\varepsilon}(\boldsymbol{u}) - p\boldsymbol{I}, \tag{4.7}$$

$$\boldsymbol{\varepsilon} = \frac{1}{2}\left(\nabla \boldsymbol{u} + \nabla \boldsymbol{u}^T\right), \tag{4.8}$$

where $\boldsymbol{I}$ is the second order identity tensor and $\boldsymbol{\varepsilon}$ is the symmetric strain rate tensor. Eq. (4.4) is the conservation of mass law, assuming that the flow is incompressible. Equations (4.5) and (4.6) represent the Dirichlet and Neumann BCs, respectively, imposed on the Dirichlet boundary $\partial\Omega_D$ and the Neumann boundary $\partial\Omega_N$.

Depending on the method, pressure and velocity can be approximated by different spaces. Let $\mathbb{Q}_e$ be the polynomial space composed of scalar functions and $\vec{\mathbb{V}}_e$ be the polynomial space composed of vector functions. The local approximation spaces for pressure and velocity are defined in the following sections.

4.2 The Taylor-Hood Approximation

Among the many approaches to solving the Stokes equations employing the FEM, the Taylor-Hood [18] element is the most widely used. In Taylor-Hood schemes, both velocity and pressure are approximated by continuous piecewise polynomials interpolated by $\mathrm{H}^1(\Omega)$ spaces:

$$\mathbb{Q}_c = \left\{ q \in \mathrm{L}^2(\Omega) \cap \mathrm{H}^1(\Omega) : q|_{\Omega_e} \in \mathbb{Q}_e \; \forall \Omega_e \in \mathcal{T} \right\}, \tag{4.9}$$

$$[\mathbb{Q}_c]^d = \left\{ \boldsymbol{v} \in \left[\mathrm{H}^1(\Omega)\right]^d : \boldsymbol{v}|_{\Omega_e} \in [\mathbb{Q}_e]^d \; \forall \, \Omega_e \in \mathcal{T} : \boldsymbol{v} \cdot \boldsymbol{n}|_{\Omega_D} = 0 \right\}. \tag{4.10}$$

To obtain the weak formulation of the Stokes problem, the procedure explained in Section 3.2 is employed. Equations 4.3 and 4.4 are multiplied by test functions $\boldsymbol{v}$ and q and integrated over the discretized domain

$$\sum_{\Omega_e \in \mathcal{T}} \int_{\Omega_e} \boldsymbol{v} \cdot (\nabla \cdot \boldsymbol{\sigma}) \, d\Omega_e = \sum_{\Omega_e \in \mathcal{T}} \int_{\Omega_e} \boldsymbol{v} \cdot \boldsymbol{f} \, d\Omega_e \;\; \forall \, \boldsymbol{v} \in [\mathbb{Q}_c]^d, \tag{4.11}$$

$$\sum_{\Omega_e \in \mathcal{T}} \int_{\Omega_e} q \, \nabla \cdot \boldsymbol{u} \, d\Omega_e = 0 \;\; \forall \, q \in \mathbb{Q}_c. \tag{4.12}$$

Integrating by parts and applying the Divergence theorem in Eq. (4.11) yields

$$\sum_{\Omega_e \in \mathcal{T}} \int_{\Omega_e} \boldsymbol{\sigma} \cdot \nabla \boldsymbol{v} \, d\Omega_e = \sum_{\Omega_e \in \mathcal{T}} \left(\int_{\Omega_e} \boldsymbol{v} \cdot \boldsymbol{f} \, d\Omega_e + \int_{\partial\Omega_e \cap \Omega_N} (\boldsymbol{\sigma n}) \cdot \boldsymbol{v} \, ds \right). \tag{4.13}$$

Replacing the stress definition in Eq. 4.13, the Stokes weak formulation for Taylor-Hood elements reads: find $\boldsymbol{u} \in \mathbb{U}$ and $p \in \mathrm{H}^1(\Omega)$ such that:

$$\begin{aligned} \sum_{\Omega_e \in \mathcal{T}} \left(\int_{\Omega_e} 2\mu \boldsymbol{\varepsilon}(\boldsymbol{u}) \cdot \boldsymbol{\varepsilon}(\boldsymbol{v}) \, d\Omega_e - \int_{\Omega_e} p \nabla \cdot \boldsymbol{v} \, d\Omega_e \right) = \\ \sum_{\Omega_e \in \mathcal{T}} \left(\int_{\Omega_e} \boldsymbol{v} \cdot \boldsymbol{f} \, d\Omega_e + \int_{\partial\Omega_e \cap \partial\Omega_N} (\boldsymbol{\sigma n}) \cdot \boldsymbol{v} \, ds \right) \quad \forall \, \boldsymbol{v} \in [\mathbb{Q}_c]^d, \end{aligned} \tag{4.14}$$

$$\sum_{\Omega_e \in \mathcal{T}} - \int_{\Omega_e} q \nabla \cdot \boldsymbol{u} \, d\Omega_e = 0 \quad \forall \, q \in \mathbb{Q}_c, \tag{4.15}$$

where $\mathbb{U} = \left\{ \boldsymbol{u} | \boldsymbol{u} \in \mathrm{H}^1(\Omega), \boldsymbol{u} = \boldsymbol{u_D} \text{ on } \partial\Omega_D \right\}$.

Since both velocity and pressure fields are approximated simultaneously, the weak formulation of eqs. (4.14) and (4.15) must satisfy the inf-sup condition [37, 38]. The inf-sup condition is a necessary and sufficient condition for the stability of the mixed formulation. Taylor-Hood elements are proven to satisfy the inf-sup condition, ensuring stability when the velocity approximation order is equal to k and the pressure approximation order is equal to $k-1$. In this work, velocity is quadratic and pressure is linear.

4.2.1 Boundary Conditions

In the Taylor-Hood element, the boundary conditions are applied as follows:

- **Dirichlet BC:** Both components of velocity are weakly imposed and can be calculated by the use of the Penalty method (Sec. 3.8);
- **Neumann BC:** surface traction is weakly imposed by the right-hand side of Eq. (4.14).

4.3 The Semi-Hybrid Approach

The Taylor-Hood methodology is commonly used, but it does not guarantee a divergence-free approximation, which means that mass conservation may not be preserved locally. To address this issue, the semi-hybrid formulation is employed.

4.3.1 Finite Dimension Spaces

To achieve the weak formulation for the Stokes equations using $\mathrm{H}(\mathrm{div}, \Omega)$ spaces as interpolating, three approximation spaces are herein defined: one for velocity, one for pressure, and

the last one for the Lagrange multiplier used to ensure the continuity of the tangential velocity.

Given a macro portion $\mathcal{T} = \{\Omega_e\}$ of Ω, the velocity approximation space $\vec{\mathbb{V}}_{div}$ is defined by [31] as follows

$$\vec{\mathbb{V}}_d = \left\{ \boldsymbol{v} \in \mathrm{H}(\mathrm{div}, \Omega) : \boldsymbol{v}|_{\Omega_e} \in \vec{\mathbb{V}}_e \; \forall \Omega_e \in \mathcal{T} \right\}, \tag{4.16}$$

$$\vec{\mathbb{V}}_{div} = \vec{\mathbb{V}}_d \cap \mathrm{H}^1(\mathcal{T}, \mathbb{R}^d), \tag{4.17}$$

and pressure approximation space $\mathbb{Q}_d$ as follows

$$\mathbb{Q}_d = \left\{ q \in \mathrm{L}^2(\Omega_e) : q|_{\Omega_e} \in \mathbb{Q}_e \; \forall \Omega_e \in \mathcal{T} \right\}. \tag{4.18}$$

A very important property of these spaces is that $\nabla \cdot \vec{\mathbb{V}}_{div} = \mathbb{Q}_d$, which leads to the method's De Rham compatibility (see Section 2.1 of [34] and eqs. (3.45) and (3.46)). The Lagrange multiplier space, also known as the tangential traction space, is defined as

$$\Lambda = \left\{ \boldsymbol{\sigma}\boldsymbol{n}|_{\partial\Omega_e} \in \mathrm{H}^{-1/2}(\partial\Omega_e, \mathbb{R}^d), \;\; \forall \Omega_e \in \mathcal{T} : \boldsymbol{\sigma} \in \mathrm{H}(\mathrm{div}, \Omega) \right\}. \tag{4.19}$$

Recalling that the Lagrange multiplier $\boldsymbol{\lambda}$ has the physical meaning of tangential stress, the space Λ is decomposed into two subspaces: one for the normal component of the stress $\boldsymbol{\Lambda}^n$ and the other for the tangential component $\boldsymbol{\lambda}^t$

$$\Lambda^n = \{\boldsymbol{\lambda^n} = (\boldsymbol{\lambda} \cdot \boldsymbol{n})\boldsymbol{n}, \; \boldsymbol{\lambda} \in \Lambda\}, \qquad \Lambda^t = \left\{\boldsymbol{\lambda}^t = \boldsymbol{\lambda} - (\boldsymbol{\lambda} \cdot \boldsymbol{n})\boldsymbol{n}, \; \boldsymbol{\lambda} \in \Lambda\right\}. \tag{4.20}$$

4.3.2 H(div, Ω) Weak Formulation

Once the approximation spaces are properly defined, the semi-hybrid formulation for the Stokes problem can be derived. The procedure is first presented by [27]. Since the tangential velocity is no longer continuous, due to $\mathrm{H}(\mathrm{div}, \Omega)$ space, the first term on the right-hand side of Eq. (4.14) can be rewritten in terms of the normal and tangential components as follows

$$\int_{\partial\Omega_e} (\boldsymbol{\sigma}\boldsymbol{n}) \cdot \boldsymbol{v} \, ds = \int_{\partial\Omega_e} (\boldsymbol{n} \otimes \boldsymbol{n})(\boldsymbol{\sigma}\boldsymbol{n}) \cdot \boldsymbol{v} \, ds + \int_{\partial\Omega_e} (\boldsymbol{I} - \boldsymbol{n} \otimes \boldsymbol{n})(\boldsymbol{\sigma}\boldsymbol{n}) \cdot \boldsymbol{v} \, ds \tag{4.21}$$

However, it is known that $[\![\boldsymbol{v} \cdot \boldsymbol{n}]\!] = 0$ for all $\boldsymbol{v} \in \vec{\mathbb{V}}_{div}$. Therefore, the traction on interfaces is expressed only by its tangential component

$$\sum_{\Omega_e \in \mathcal{T}} \int_{\partial\Omega_e} (\boldsymbol{n} \otimes \boldsymbol{n})(\boldsymbol{\sigma}\boldsymbol{n}) \cdot \boldsymbol{v} \, ds = \sum_{E \in \varepsilon^0} \int_E (\boldsymbol{\sigma}\boldsymbol{n} \cdot \boldsymbol{n})[\![\boldsymbol{v} \cdot \boldsymbol{n}]\!] \, dE = 0, \tag{4.22}$$

$$\sum_{\Omega_e \in \mathcal{T}} \int_{\partial\Omega_e} (\boldsymbol{\sigma}\boldsymbol{n}) \cdot \boldsymbol{v} \, ds = \sum_{\Omega_e \in \mathcal{T}} \int_{\partial\Omega_e} (\boldsymbol{I} - \boldsymbol{n} \otimes \boldsymbol{n})(\boldsymbol{\sigma}\boldsymbol{n}) \cdot \boldsymbol{v} \, ds. \tag{4.23}$$

Replacing the tangential traction by the Lagrange multiplier $\boldsymbol{\lambda}^t$, Eq. (4.23) becomes

$$\sum_{\Omega_e \in \mathcal{T}} \int_{\partial\Omega_e} \boldsymbol{\lambda}^t \cdot \boldsymbol{v}\, ds = \sum_{E \in \varepsilon^0} \int_E \boldsymbol{\lambda}^t \cdot [\![\boldsymbol{v}]\!]\, dE + \sum_{E \in \partial\Omega_N} \int_{\partial\Omega_e} \boldsymbol{\lambda}^t \cdot \boldsymbol{v}\, ds. \tag{4.24}$$

By summing up all the contributions from each element, the semi-hybrid formulation for the Stokes problem reads: find $\boldsymbol{u}, p$, and $\boldsymbol{\lambda}^t \in \vec{\mathbb{V}}_{div} \times \mathbb{Q}_d \times \Lambda^t$ such that

$$\begin{aligned} \sum_{\Omega_e \in \mathcal{T}} \left(\int_{\Omega_e} 2\mu\boldsymbol{\varepsilon}(\boldsymbol{u}) \cdot \boldsymbol{\varepsilon}(\boldsymbol{v})\, d\Omega_e - \int_{\Omega_e} p\nabla \cdot (\boldsymbol{v})\, d\Omega_e \right) - \sum_{E \in \varepsilon^0} \int_E \boldsymbol{\lambda}^t \cdot [\![\boldsymbol{v}]\!]\, dE = \\ \sum_{\Omega_e \in \mathcal{T}} \left(\int_{\Omega_e} \boldsymbol{v} \cdot \boldsymbol{f}\, d\Omega_e + \int_{\partial\Omega_e \cap \partial\Omega_N} (\boldsymbol{\sigma}\boldsymbol{n} \cdot \boldsymbol{n})(\boldsymbol{v} \cdot \boldsymbol{n})\, ds \right) \quad \forall \boldsymbol{v} \in \vec{\mathbb{V}}_{div}, \end{aligned} \tag{4.25}$$

$$\sum_{\Omega_e \in \mathcal{T}} - \int_{\Omega_e} q\nabla \cdot (\boldsymbol{u})\, d\Omega_e = \boldsymbol{0} \quad \forall q \in \mathbb{Q}_d, \tag{4.26}$$

$$\sum_{E \in \varepsilon^0} \int_E \boldsymbol{\eta}^t \cdot [\![\boldsymbol{u}]\!]\, dE = \sum_{\Omega_e \in \mathcal{T}} \int_{\partial\Omega_e \cap \partial\Omega_N} \boldsymbol{\eta}^t \cdot (\boldsymbol{u} - \boldsymbol{u_D})\, ds \quad \forall \boldsymbol{\eta}^t \in \Lambda^t, \tag{4.27}$$

4.3.3 Boundary Conditions

Dirichlet BCs $\boldsymbol{u} = \boldsymbol{u_D}$ are decomposed into its normal and tangential components, as follows

- **Normal velocity:** is weakly imposed through the use of the penalty method, applying the expression $\int_{\partial\Omega_D} B(\boldsymbol{u} \cdot \boldsymbol{n} - \boldsymbol{u_D} \cdot \boldsymbol{n})(\boldsymbol{v} \cdot \boldsymbol{n})\, ds = 0$, where B is the penalization constant (see Section 3.8).
- **Tangential velocity:** weakly imposed using Eq. (4.27).

Neumann BCs are imposed in terms of stresses $\boldsymbol{\theta}_N$. Following the same done to Dirichlet BCs, decomposing $\boldsymbol{\theta}_N$ into normal and shear stresses, the BCs are enforced as follows

- **Normal stress:** weakly imposed by the term Eq. (4.25).
- **Shear stress:** the tangential stress $\boldsymbol{\theta}_N$ is weakly imposed by the penalization method through the expression $\int_{\partial\Omega_N} B(\boldsymbol{\lambda}^t \cdot \boldsymbol{t} - \boldsymbol{\theta}_N \cdot \boldsymbol{t})(\boldsymbol{\eta}^t \cdot \boldsymbol{t})\, ds = 0$

4.4 The Hybrid-Hybrid Approach

The semi-hybrid approach has been proven to be mathematically consistent in [26], however, some of its properties must be highlighted. After eliminating the internal velocities and higher order pressures from the global system, it originates a saddle-point problem with

two different constraints: a mean pressure per element $p \in L^2(\Omega)$ and the shear stresses $\boldsymbol{\lambda}^t \in H^{-1/2}(\partial\Omega_e)$ over the element interfaces.

The decomposition of such matrices is complicated from the numerical point of view, as a specific permutation must be employed to avoid zero pivots when decomposing the Lagrange multipliers degrees of freedom. Additionally, the usage of the penalty method to impose shear stress boundary conditions has been demonstrated to introduce numerical instabilities which compromise the accuracy of the formulation.

Under these circumstances, and aiming to derive an equivalent formulation but with better spectral properties, a second hybridization of the tangential stresses is proposed to recover the primal form. Introducing the space $\mathcal{L}^t \subset H^{1/2}(\partial\Omega_e)$ for the tangential velocity, defined over the interfaces $E \in \varepsilon^0$, the hybrid form thus reads: find $\{\boldsymbol{u}, p, \boldsymbol{\lambda}^t, \boldsymbol{u}^t\} \in \vec{\mathbb{V}}_{div} \times \mathbb{Q}_d \times \Lambda^t \times \mathcal{L}^t$ such that for all $\boldsymbol{v}, q, \boldsymbol{\eta}^t, \boldsymbol{v}^t \in \vec{\mathbb{V}}_{div} \times \mathbb{Q}_d \times \Lambda^t, \mathcal{L}^t$, the following equations are satisfied:

$$\sum_{\Omega_e \in \mathcal{T}} \left(\int_{\Omega_e} 2\mu\boldsymbol{\varepsilon}(\boldsymbol{v}) \cdot \boldsymbol{\varepsilon}(\boldsymbol{u}) d\Omega_e - \int_{\Omega_e} p(\nabla \cdot \boldsymbol{v}) d\Omega_e - \int_{\partial\Omega_e} \boldsymbol{\lambda}^t \cdot \boldsymbol{v} ds \right) = \sum_{\Omega_e \in \mathcal{T}} \left(\int_{\Omega_e} \boldsymbol{v} \cdot \boldsymbol{f} d\Omega_e + \int_{\partial\Omega_e \cap \partial\Omega_N} (\boldsymbol{\sigma}\boldsymbol{n} \cdot \boldsymbol{n})(\boldsymbol{v} \cdot \boldsymbol{n}) ds \right) \tag{4.28}$$

$$\sum_{\Omega_e \in \mathcal{T}} - \int_{\Omega_e} q(\nabla \cdot \boldsymbol{u}) d\Omega_e = \boldsymbol{0} \tag{4.29}$$

$$\sum_{\Omega_e \in \mathcal{T}} - \int_{\partial\Omega_e} \boldsymbol{u} \cdot \boldsymbol{\eta}^t d\partial\Omega_e - \sum_{E \in \varepsilon^0} \int_E [\![\boldsymbol{\eta}^t]\!] \cdot \boldsymbol{u}^t dE = \boldsymbol{0} \tag{4.30}$$

$$\sum_{E \in \varepsilon^0} - \int_E [\![\boldsymbol{\lambda}^t]\!] \cdot \boldsymbol{v}^t dE = \sum_{\Omega_e \in \mathcal{T}} \int_{\partial\Omega_e \cap \Omega_N} \boldsymbol{v}^t \cdot (\boldsymbol{\lambda}^t - \boldsymbol{\theta}_N) \, ds, \tag{4.31}$$

where Eq. (4.31) was introduced to impose the continuity of the tangential traction across ε^0. Even though an additional constraint is introduced, $\boldsymbol{\lambda}^t$ is now associated with a single element therefore it can be statically condensed and eliminated from the global system. Also, its condensation into the tangential velocities gives rise to a symmetric-positive-semi-definite block. The elemental matrix is then left with contributions from normal velocities, tangential velocities, and a single pressure, thus having better spectral properties and being easier to solve compared to Eqs. (4.25), (4.26) and (4.27).

4.4.1 Boundary Conditions

Dirichlet BCs $\boldsymbol{u} = \boldsymbol{u_D}$ are decomposed into its normal and tangential components. Differently from the semi-hybrid formulation, in the hybrid-hybrid formulation, both components of the velocity are weakly imposed by the Penalty Method. The BCs are applied as follows

- **Normal velocity:** is weakly imposed through the use of the penalty method, applying the expression $\int_{\partial\Omega_D} B(\boldsymbol{u} \cdot \boldsymbol{n} - \boldsymbol{u_D} \cdot \boldsymbol{n})(\boldsymbol{v} \cdot \boldsymbol{n}) \, ds$.

- **Tangential velocity:** weakly imposed applying the penalty method given by the expression $\int_{\partial\Omega_D} B(\boldsymbol{u}\cdot\boldsymbol{t} - \boldsymbol{u_D}\cdot\boldsymbol{t})(\boldsymbol{v}\cdot\boldsymbol{t})\, ds$.

Following the same done to Dirichlet BCs, decomposing $\boldsymbol{\theta}_N$ into normal and shear stresses, the BCs are enforced as follows

- **Normal stress:** weakly imposed by Eq. (4.28).
- **Shear stress:** weakly imposed by Eq. (4.31).

Figure 4.1 depicts the Lagrange multipliers created for each formulation. Note that the Taylor-Hood element does not require the use of Lagrange multipliers (displayed in red and blue), having continuous velocity between elements.

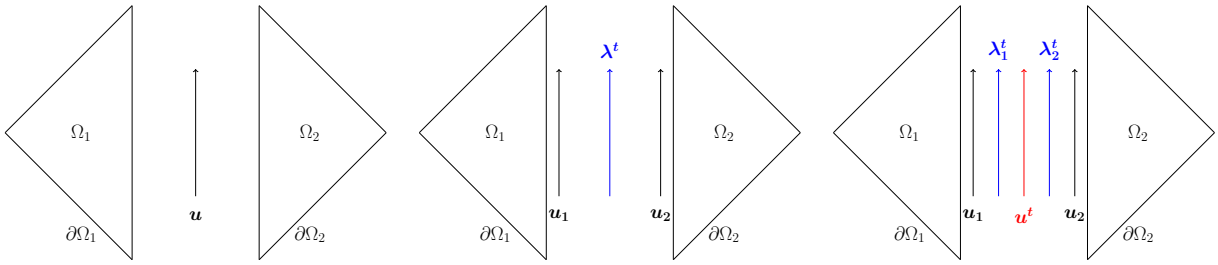

(a) Taylor-Hood. (b) Semi-hybrid (c) Hybrid-hybrid

Figure 4.1: Lagrange multiplier and elements E for each weak formulation.

4.5 Local Mass Conservation

As already mentioned, the semi-hybrid and the hybrid-hybrid formulations with the pair H(div, Ω)-L$^2(\Omega)$ guarantee local mass conservation. The conservation of mass must hold for any test function $q \in \mathbb{Q}_d$. Choosing $q = \nabla\cdot\boldsymbol{u}$ yields to:

$$-\int_\Omega (\nabla\cdot\boldsymbol{u})^2\, d\Omega = 0, \tag{4.32}$$

which can only be satisfied if $\nabla\cdot\boldsymbol{u} = 0$. This is the definition of local mass conservation for incompressible flows.

4.6 Computational Aspects

This section aims to briefly discuss the main impacts of this work on the NeoPZ library, as well as the computational aspects of the hybrid-hybrid formulation implementation.

To be able to simulate Stokes flows with the hybrid-hybrid formulation, four classes are developed in the NeoPZ library: ProblemData, TPZMeshOperator, TPZStokesMaterial, and TPZStokesMaterialTH. ProblemData creates an object that contains all the necessary data for

the simulation. The TPZMeshOperator class works on mesh methods, creating computational and geometrical meshes, inserting interfaces, and condensing elements. The TPZMeshOperator also contains methods responsible for working and dealing with one of the main goals of this work: obstructed domains. These functions can identify the elements belonging to the obstruction so that their equations are filtered and not considered in the global system.

The other two classes contain the implementation of the weak statement for the hybrid-hybrid and Taylor-Hood formulations of the Stokes equations, respectively. All these classes are incorporated into the NeoPZ library, which can be used in the future for other people aiming to simulate Stokes flows with the hybrid-hybrid formulation.

4.6.1 ProblemData

The ProblemData class is used to create an object that stores all the information required by the simulation. The class has the following attributes:

- MeshName;
- HdivType;
- VelpOrder;
- TracpOrder;
- Dim;
- Resolution;
- StaticCondensation;
- Domain;
- NormalBoundary;
- TangentialBoundary;
- InterfaceID;
- LambdaID;
- HasAnalyticSolution;

Each one of these attributes can be set on a JSON file, that is read by the ProblemData class, and assigned to the object. MeshName contains the gmsh file where the mesh information is, HdivType is an integer, where 0 indicates Hdiv-S and 1 Hdiv-C, VelpOrder and TracpOrder is the approximation order used in the simulation (more details in Table 4.1), and Dim stores the simulation dimension. Resolution is a post process attribute, indicating the resolution of the graphic result, and StaticCondensation is a bool that employs the static condensation.

The information about the domain, such as the viscosity value, is passed in the Domain attribute. The same is valid for the boundary conditions, which are stored in the NormalBoundary and TangentialBoundary attributes. For Taylor-Hood simulations, only the TangentialBoundary is used due to the way the boundary conditions are imposed.

The InterfaceID and LambdaID are used to identify the interfaces and Lagrange multipliers that are going to be inserted and created during the simulation. Finally, the HasAnalyticSolution attribute is used to indicate whether the simulation has an analytical solution or not.

4.6.2 TPZMeshOperator

The TPZMeshOperator class only has static methods, which means that no object of this class is created to use its methods. The methods are called directly from the main function or other parts of the code.

As shown in Figure 4.2, the TPZMeshOperator class's methods can be divided into three major groups: mesh creation, interfaces and static condensation, and filter and transfinite interpolation. The mesh creation group contains the methods responsible for creating the geometrical and computational meshes for each state variable (velocity, pressure, Lagrange multipliers, mean pressure, and mean flux if needed). The multiphysics mesh is created for the code to be able to handle multiple state variables.

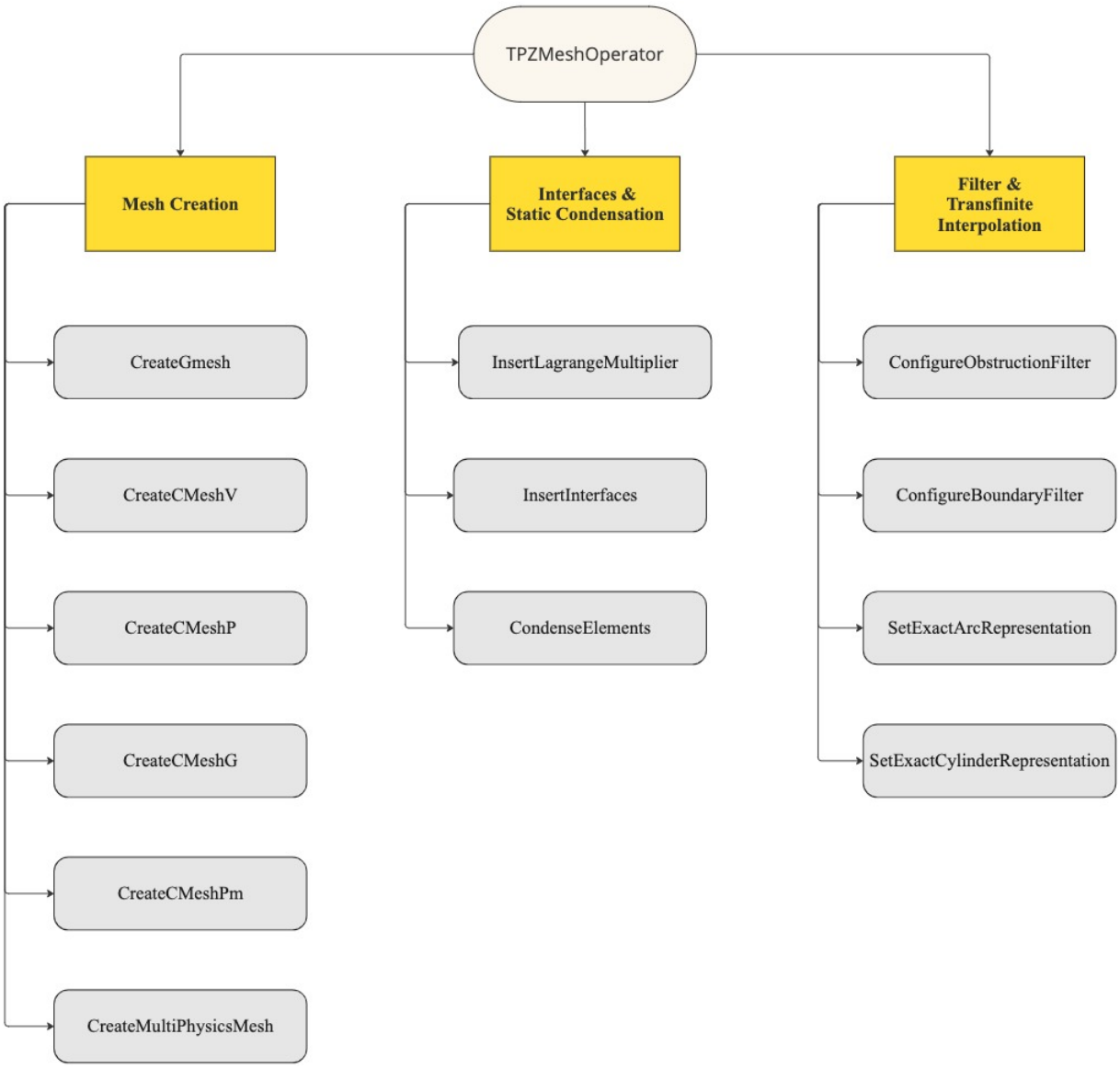

Figure 4.2: Methods of the TPZMeshOperator class.

During the creation of the velocity and pressure meshes, the polynomial order must be cho-

sen properly to ensure the stability and convergence of the method. For $\mathrm{H}(\mathrm{div}, \Omega)$ spaces, a difference is made between the polynomial order used for the facet and inner velocity. This is because the inner velocity is enriched depending on whether the hybrid or semi-hybrid formulation is employed and on the type of employed $\mathrm{H}(\mathrm{div}, \Omega)$ space. So is the pressure, in the case of employing Hdiv-S.

Let k be the polynomial approximation order for the facet velocity, then Table 4.1 shows the relation between the polynomial order for the velocities, facet and inner, pressure, and traction.

Table 4.1: Polynomial orders for the hybrid-hybrid and semi-hybrid formulations.

Method	**Facet Velocity**	**Inner Velocity**	**Pressure**		**Tangential Velocity and Traction**
			Hdiv-S	**Hdiv-C**	
Taylor-Hood[1]	k	k	-	-	-
Semi-hybrid	k	$k+1$	$k+1$	0	$k-1$
Hybrid-hybrid	k	$k+2$	$k+2$	0	$k-1$

[1] Taylor-Hood formulation does not employ $\mathrm{H}(\mathrm{div}, \Omega)$ spaces for the velocity. In this case, no distinction is made between the inner and facet velocity, and the pressure approximation order is equal to $k-1$. No Lagrange multiplier is used.

The insert interfaces and static condensation group is the group of methods that aims at the insertion of all the interfaces required by the hybrid-hybrid formulation (see Figure 4.3). Between each tangential traction and tangential velocity, one interface is created. Over these interfaces, the jump of the Lagrange multipliers is evaluated. The CondenseElements method is responsible for condensing the DoFs that are not shared between the elements. For the semi-hybrid, internal velocities and discontinuous pressures, while for the hybrid-hybrid, internal velocities, discontinuous pressures, and tangential tractions.

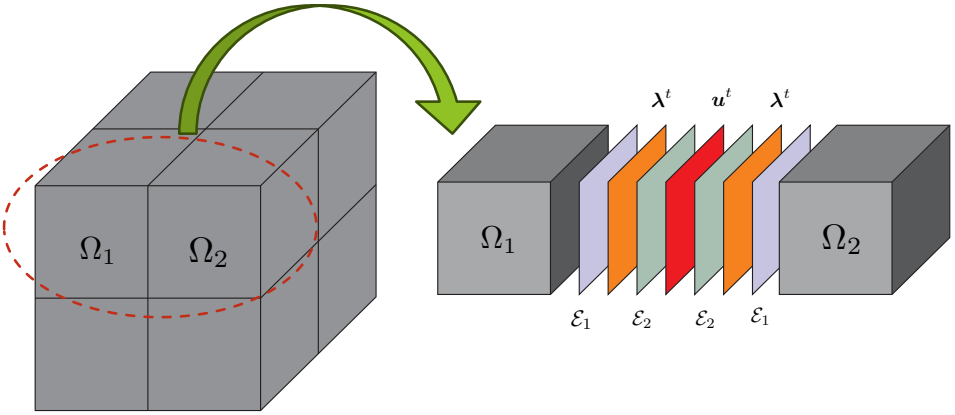

Figure 4.3: Interfaces inserted during the hybrid-hybrid formulation.

Where, in the hybrid-hybrid formulation, ε_2 evaluates the tangential velocity $\boldsymbol{u}^t$ and the jump of $\boldsymbol{\lambda}^t$ between both elements, ensuring the continuity of the tangential velocity. In the

semi-hybrid formulation, ε_1 evaluates the jump of the velocity between the elements, ensuring the continuity of the tangential traction $\boldsymbol{\lambda}^t$.

The filtering functions are better explained in Chapter 6, where an obstruction device is inserted into the domain to study its impact on the flow pattern. The transfinite interpolator (see Section 5.2.1 for more details) is employed by using the SetExactArcRepresentation method, for two-dimensional meshes, and SetExactCircleRepresentation, for three-dimensional meshes.

4.6.3 TPZStokesMaterial and TPZStokesMaterialTH

Since the TPZStokesMaterial and TPZStokesMaterialTH classes implement the weak statement for the Stokes equations and inherit from the same base class, they are both discussed in this Section. While the TPZStokesMaterial implements the hybrid-hybrid formulation, the TPZStokesMaterialTH implements the Taylor-Hood formulation. Figure 4.4 shows the main methods of the TPZStokesMaterial and TPZStokesMaterialTH classes.

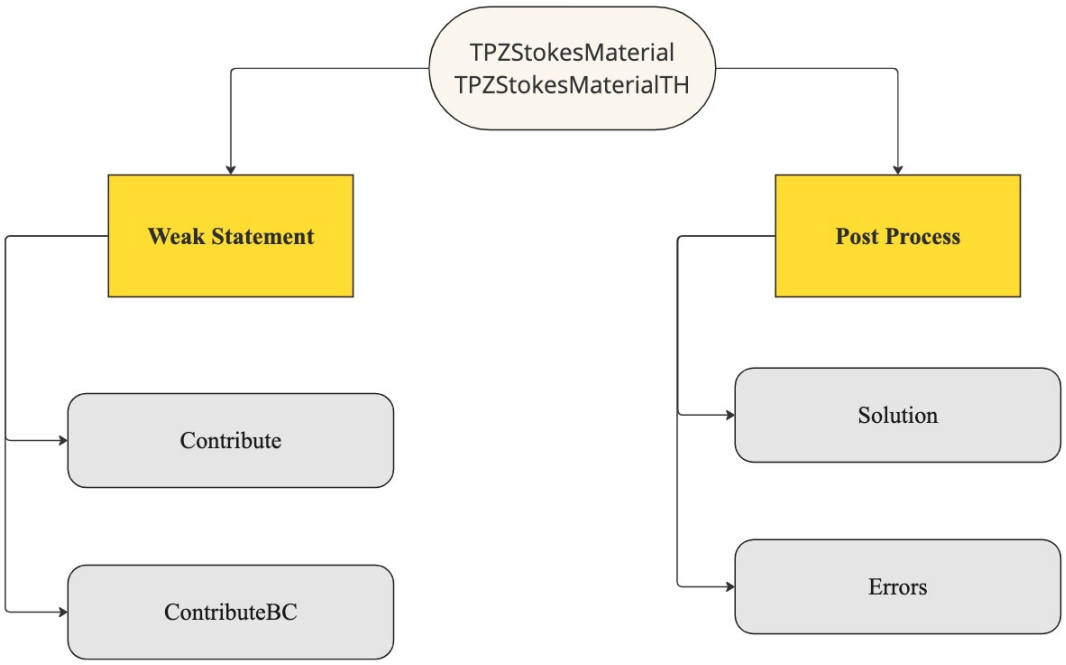

Figure 4.4: TPZStokesMaterial and TPZStokesMaterialTH classes methods.

In these classes, two major groups can be identified: the group of methods responsible for the weak statement, and the group of methods responsible for post-processing the solution. In the Contribute method, the weak statement is implemented for the hybrid-hybrid and Taylor-Hood formulations. The ContributeBC method is responsible for the implementation of the way the boundary conditions are imposed. It is worth mentioning that there are many more methods in the TPZStokesMaterial and TPZStokesMaterialTH classes that help in the implementation of the weak statement. The full code can be found in Appendix A.

The post-process group also is composed of many methods, however, the Solution and Errors methods stand out. The solution method gets as input the solution obtained from the linear system solver and returns the values for pressure, velocity, and stress. It also evaluates the exact solution if it is available and the error between the numerical and exact solutions. The Errors method evaluates the L^2-error norm for each state variable and post-process variables.

Chapter 5

Numerical Simulations

The first part of this section presents the Poiseuille flow problem and the Lid-Driven Cavity problem as a way to verify the hybrid-hybrid formulation. Two- and three-dimensional versions of these problems are presented. Convergence analyses are also performed to verify the rate of convergence of the implemented formulation. For both, two- and three-dimensional problems, the convergence rate and errors are calculated using the L^2-error norm relative to the analytical solution. Posteriorly, the results are compared to the expected rate of convergence (see Table 5.1) and the classical Taylor-Hood element.

Table 5.1: Simulation information for Taylor-Hood and hybrid-hybrid methods.

Method	**Approximation Space**		**L^2-convergence rates**			**Divergence Free**
	for u	**for p**	**in u**	**in p**	**in σ**	
Taylor-Hood	$H^1(\Omega)$	$H^1(\Omega)$	k+1	k	k	No
Hybrid-hybrid	Hdiv-S	$L^2(\Omega)$	k+1	k	k	Yes
	Hdiv-C	$L^2(\Omega)$	k+1	1	1	Yes

For the rates shown in Table 5.1, k is the polynomial order of the approximation space for the facet velocity. A comparison considering the number of condensed Degrees of Freedom (DoFs) and respective errors for Taylor-Hood and hybrid-hybrid formulations is also presented. Finally, application examples are presented to demonstrate the range of flows that can be solved using the hybrid-hybrid formulation.

5.1 Two-Dimensional Flows

Two benchmarks are presented in the current section. The first one is the Poiseuille flow, which represents the flow between two parallel plates. In this case, both plates are fixed and a pressure gradient induces the flow motion. For Poiseuille flows, a linear pressure distribution is

expected along the flow direction and a quadratic velocity profile over the y-direction. Figure 5.1 depicts the expected velocity profile.

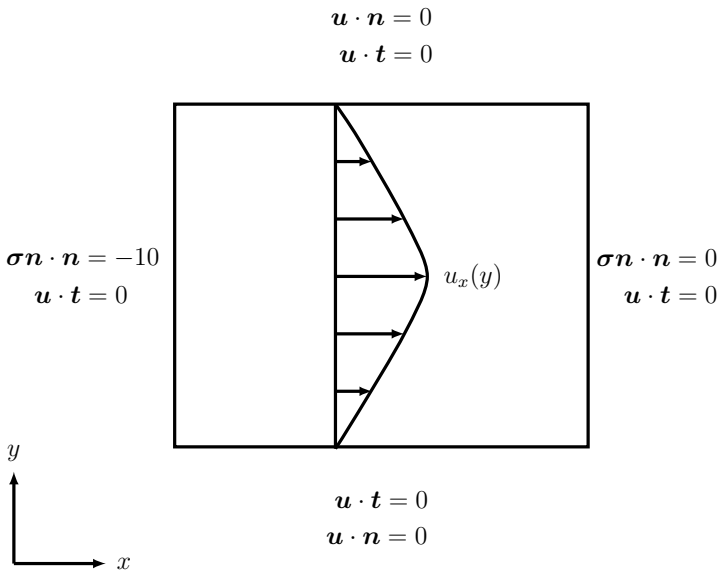

Figure 5.1: Poiseuille flow: boundary conditions and velocity profile.

The domain is given by the unit square $\Omega = [0,1] \times [0,1]$. Boundary conditions are also shown in Figure 5.1. A no-slip ($\boldsymbol{u}\cdot\boldsymbol{t} = 0$) BC is applied on every border, no-penetration ($\boldsymbol{u}\cdot\boldsymbol{n} = 0$) BC is imposed on the upper and lower borders, inlet normal stress ($(\boldsymbol{\sigma n})\cdot\boldsymbol{n} = -10$) is imposed on the left border, and outlet normal stress ($(\boldsymbol{\sigma n})\cdot\boldsymbol{n} = 0$) is imposed on the right border. For simplicity, viscosity μ is set to 1 and the domain is composed of 100 elements (10×10). See eqs. (5.1) to (5.3) for the Poiseuille flow analytical solution under these conditions.

$$p = -10(x-1) \tag{5.1}$$

$$\boldsymbol{u} = \left\{ \frac{\partial p/\partial x}{2\mu}(y - y^2), 0 \right\} \tag{5.2}$$

$$\boldsymbol{\sigma} = \begin{bmatrix} 10(x-1) & \frac{\partial p/\partial x}{2\mu}(1-2y) \\ \frac{\partial p/\partial x}{2\mu}(1-2y) & 10(x-1) \end{bmatrix} \tag{5.3}$$

Figures 5.2 - 5.5 show the pressure, velocity and stress numerical solutions for the Poiseuille flow. Note that two pressure and stress profiles are depicted, one using Hdiv-S space and another using Hdiv-C space to approximate velocity.

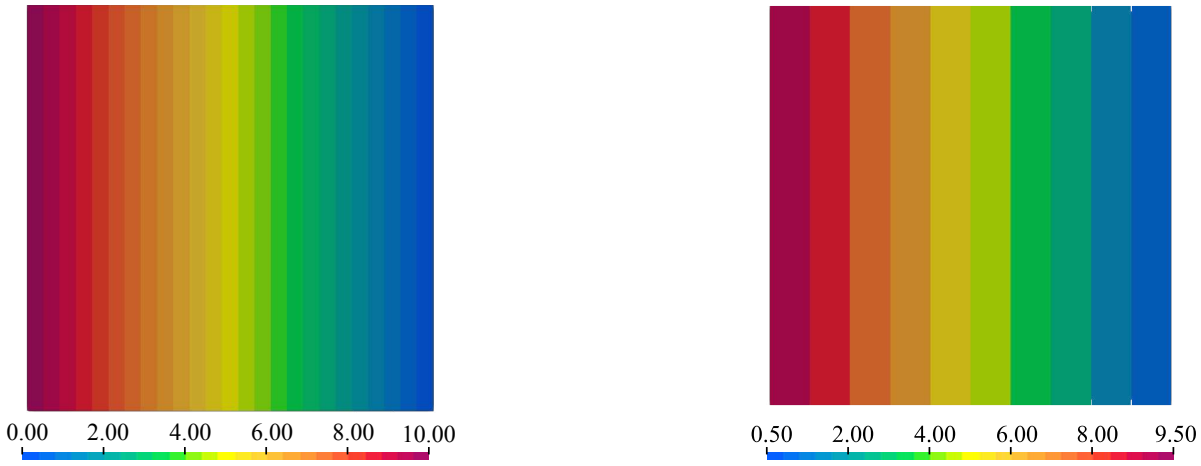

(a) Hdiv-S (b) Hdiv-C

Figure 5.2: 2D Poiseuille flow pressure field.

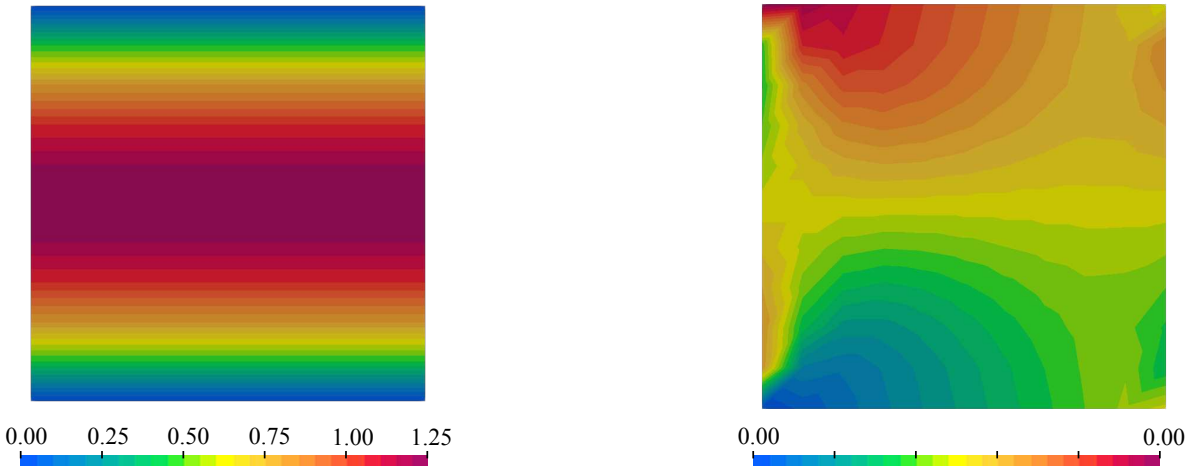

(a) u_x (b) u_y

Figure 5.3: 2D Poiseuille flow velocity field.

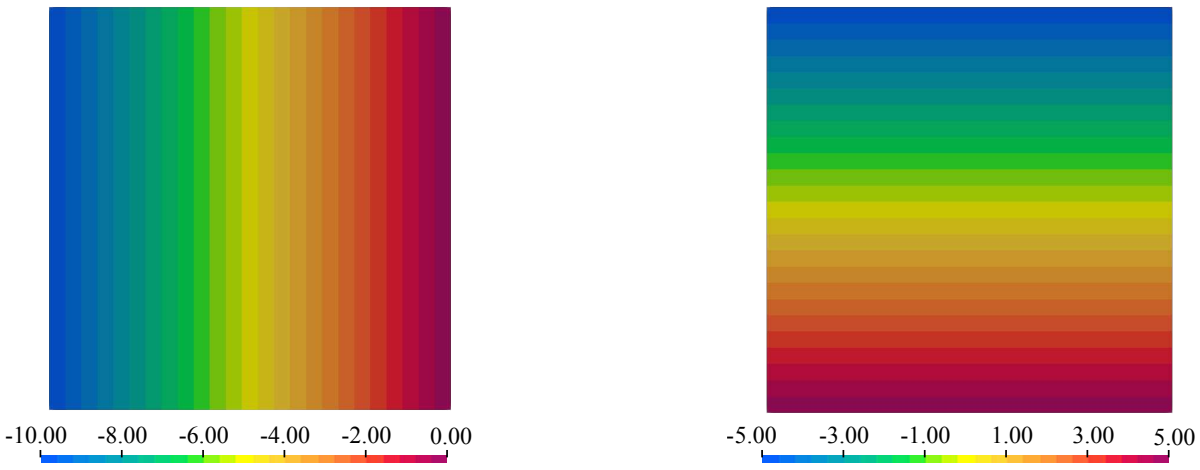

(a) σ_{xx} and σ_{yy} (b) σ_{xy} and σ_{yx}

Figure 5.4: 2D Poiseuille flow stress field - numerical results for Hdiv-S approximation space.

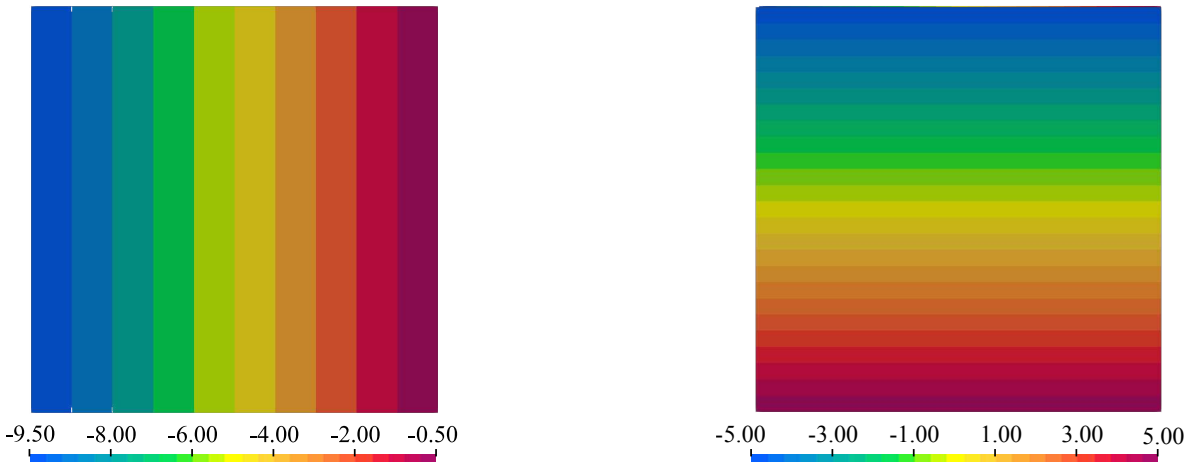

(a) σ_{xx} and σ_{yy} (b) σ_{xy} and σ_{yx}

Figure 5.5: 2D Poiseuille flow stress field - numerical results for Hdiv-C approximation space.

As expected, Hdiv-C space yields an element-wise constant pressure, while Hdiv-S results in a smoother pressure gradient along the domain. The velocity field is also in agreement with the analytical solution, being the u_x component quadratic and the u_y component null. Both spaces Hdiv-S and Hdiv-C yield the same result for the velocity field. When the Hdiv-S space is employed, the analytic stress field is recovered. For Hdiv-C simulations, the deviatoric stress recovers the analytic solution as the Cauchy stress tensor depends on the pressure.

The second benchmark is the Lid-Driven Cavity (LDC) flow. In this scenario, there is no analytical solution available, but the flow behavior is numerically known and widely used in the literature to verify numerical methods. LDC simulations offer a systematic way of comparison between computational and experimental research and consist of a square cavity in which the upper wall is a lid that is dragged at a constant velocity. This motion induces flow and vorticity in the cavity. For more details on the LDC, one refers to [53].

Boundary conditions are as follows: no-penetration ($\boldsymbol{u} \cdot \boldsymbol{n} = 0$) on every border, unit tangential velocity ($\boldsymbol{u} \cdot \boldsymbol{t} = -1$, negative due to the tangential vector orientation) on the top, and slip condition ($(\boldsymbol{\sigma n}) \cdot \boldsymbol{t} = 0$) on the remaining borders (see Figure 5.6). The domain is the unit square $\Omega = [0, 1] \times [0, 1]$ and is composed of 100 elements. Viscosity μ is also set to 1.

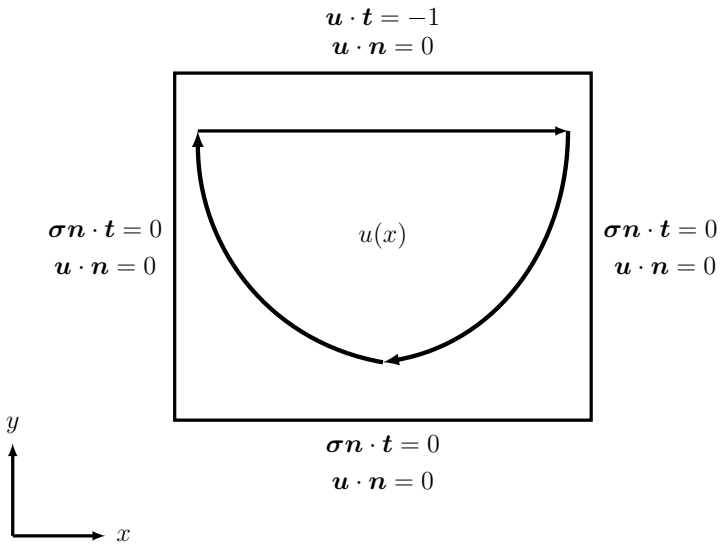

Figure 5.6: Lid-driven cavity flow: boundary conditions and velocity profile.

Velocity field and streamlines are depicted in Figure 5.7, which can be compared to the results presented in [53]. Note that, due to the absence of the convective term, velocity is symmetric along the y-axis. Streamlines show the expected vorticity pattern in the cavity.

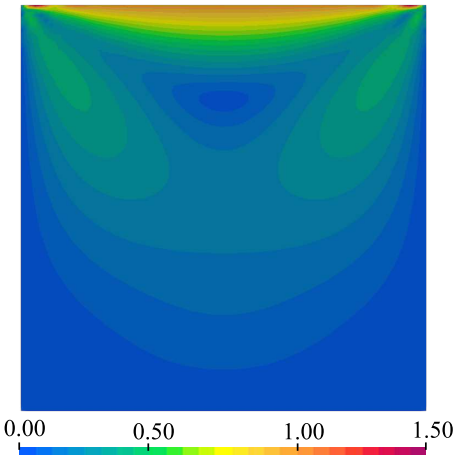

(a) Velocity magnitude.

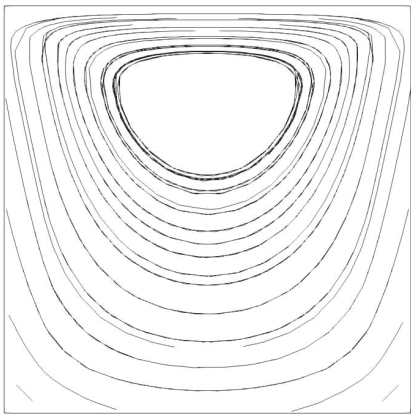

(b) Streamlines.

Figure 5.7: 2D Lid-driven cavity flow velocity field.

Analyzing the pressure (see Figure 5.8), one can observe at the superior corners, the presence of two singularities. Such peaks of pressure are because the velocity is bivalued at these corners, which means that on the lid it is required to be unit, and yet on the lateral walls it must be null.

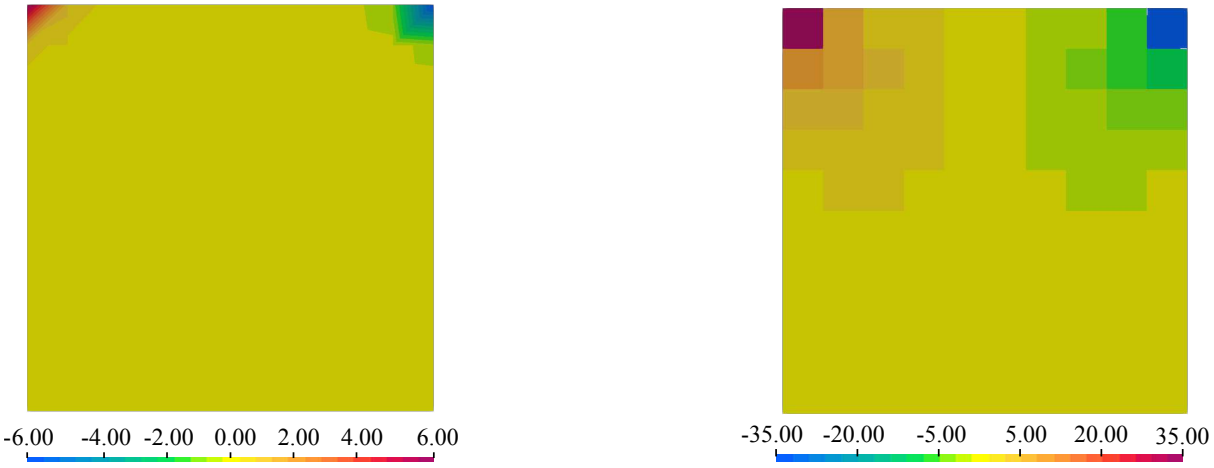

(a) Hdiv-S ($\times 10^2$). (b) Hdiv-C.

Figure 5.8: 2D Lid-driven cavity flow pressure field.

Note that the singularities presented in the pressure field are not the same for both Hdiv-S and Hdiv-C spaces. This is expected since they are not analytical solutions to be achieved, instead, they are singularities caused by a bi-valued velocity on the corner and depend on the approximation space employed. The velocity profile and the streamlines are the same.

To avoid these singularities, the pressure on one of the superior corners can be imposed, avoiding the bivalued velocity. However, the influence of these singularities over the domain does not affect the rest of the solution, and the results remain consistent with the ones observed in experimental studies [54]

Although both Poiseuille and Lid-Driven Cavity flows are used to observe whether the implemented method is working, they do not provide a convergence analysis. Poiseuille flows are too simple, and the analytical solution is a subset of the space used to interpolate velocity. In other words, with only one element, the velocity solution is recovered. On the other hand, LDC flows do not have an analytical solution, and a comparison can be made only qualitatively. Thus, another problem, with an analytical solution complex enough is used to obtain the rate of convergence for the double hyrbrid formulation.

5.1.1 Convergence Analysis for Quadrilateral Elements

A Stokes model with a manufactured solution is adopted to verify two-dimensional problems. The domain is the unit square $\Omega = [0,1] \times [0,1]$ depicted in Figure 5.9. Boundary conditions are applied as follows: tangential velocity ($\boldsymbol{u} \cdot \boldsymbol{t}$) on all edges, normal velocity ($\boldsymbol{u} \cdot \boldsymbol{n}$) on the left, top, and right edges, and normal stress ($\boldsymbol{\sigma n} \cdot \boldsymbol{n}$) on the bottom edge.

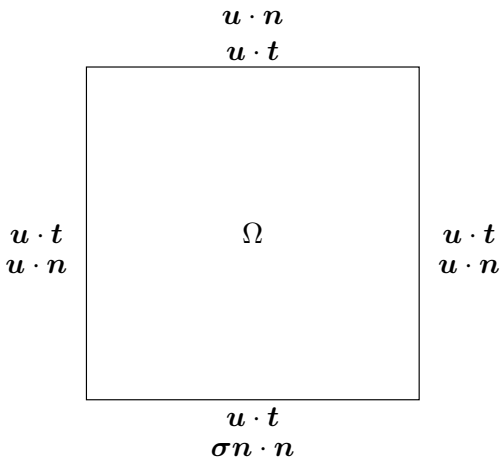

Figure 5.9: Domain and boundary conditions for the two-dimensional verification test.

A similar problem, with a different pressure field, is proposed in [55]. The source term $\boldsymbol{f}$ is chosen such that the eqs. (5.4) and (5.5) describe the solution for the velocity and pressure fields, respectively

$$\boldsymbol{u} = \begin{bmatrix} -256x^2(x-1)^2y(y-1)(y-2) \\ 256y^2(y-1)^2x(x-1)(x-2) \end{bmatrix}, \tag{5.4}$$

$$p = 150\left(x-\frac{1}{2}\right)^2\left(y-\frac{1}{2}\right)^2. \tag{5.5}$$

Convergence analyses are performed for the Hdiv-C and Hdiv-S spaces using structured meshes with $N = 2\times 2$, $N = 4\times 4$, $N = 8\times 8$, and $N = 16\times 16$ elements. For simplicity, fluid viscosity μ is set to 1. The approximation order for the facet velocity is set to $k = 1, 2, 3, 4$. Figure 5.10 shows the solutions for pressure and velocity fields when the Hdiv-C is employed on the most refined mesh, for $k = 4$.

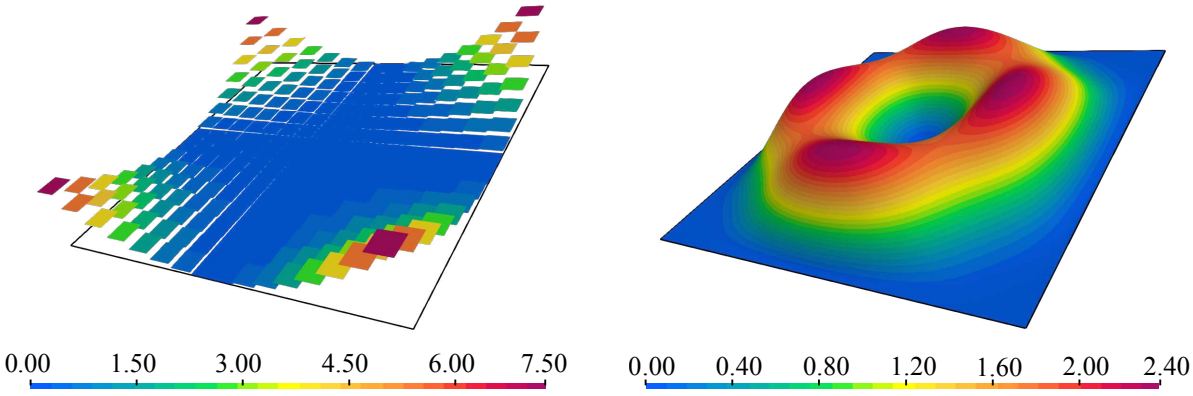

(a) Pressure field: Hdiv-C.

(b) Velocity field.

Figure 5.10: Achieved solution for the two-dimensional problem using $k = 4$, square mesh with $N = 16\times 16$ elements, and Hdiv-C space.

In Fig. 5.10, both pressure and velocity fields are warped so that the field magnitude is

represented on the z-axis. The warp scale for pressure is equal to 0.025, and for velocity, 0.075. Note that the pressure is constant by element, as expected in Hdiv-C simulations. The black square underneath the plots indicates the domain of the problem.

If the Hdiv-S space is employed, the recovered pressure field is not constant by element, resulting in a smoother solution (see Figure 5.11). The velocity field, however, is the same for both spaces. The main reason why to use the Hdiv-C over Hdiv-S is that, for a lesser number of DoFs, the Hdiv-C space yields a velocity solution with the same accuracy as the Hdiv-S space. This is further discussed in Section 5.3.

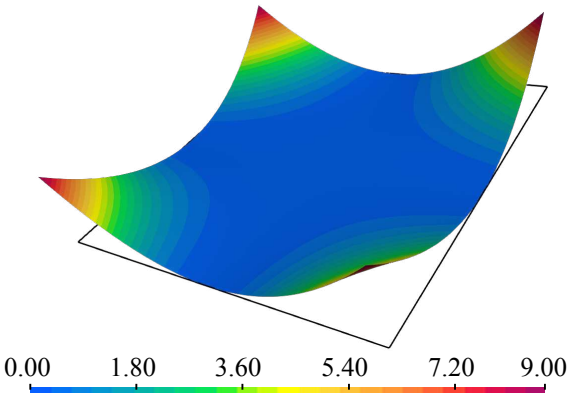

Figure 5.11: Pressure field solution using $k = 4$, square mesh with $N = 16 \times 16$ elements, and the Hdiv-S space.

Rates of convergence for the pressure, velocity, deviatoric stress, and the Cauchy stress fields are displayed in Figures 5.12 - 5.15, respectively. Observe that k_{TH} is the polynomial order of the Taylor-Hood element, which is quadratic for this simulation. The subscript h beside each state variable indicates the numerical solution. In this context, the L^2-norm error is calculated as the difference between the analytical and numerical solutions. Note that every element has the average edge size $h_{el} = 1/N$.

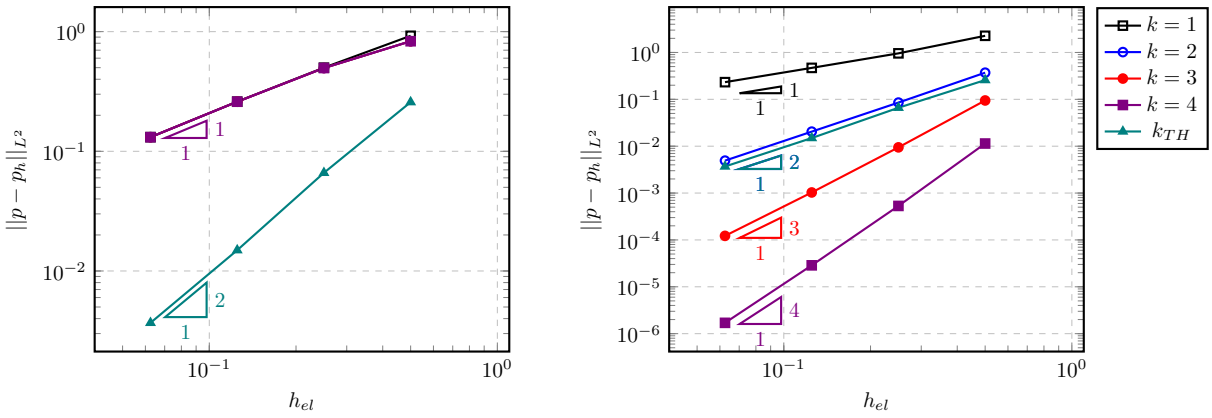

(a) Hdiv-C (b) Hidv-S

Figure 5.12: Two-dimensional verification test: convergence analysis for pressure field.

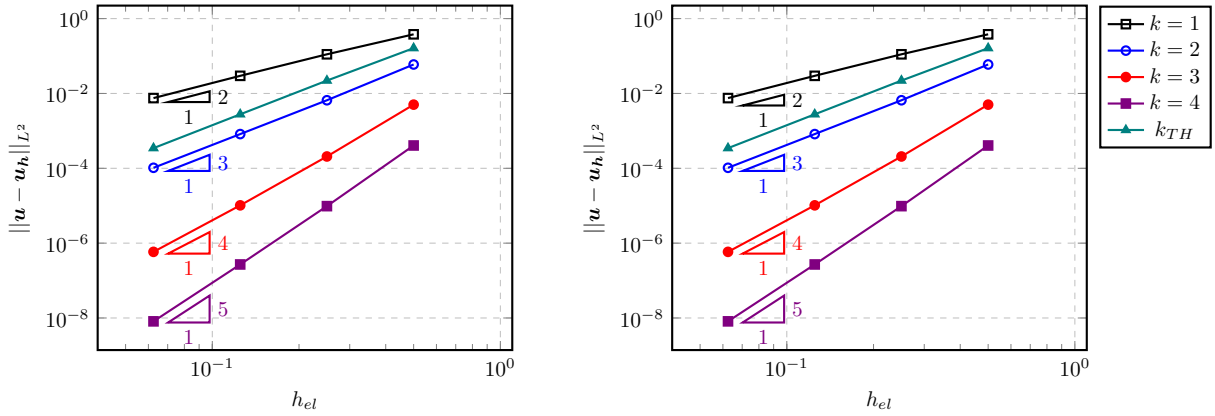

(a) Hdiv-C (b) Hidv-S

Figure 5.13: Two-dimensional verification test: convergence analysis for velocity field

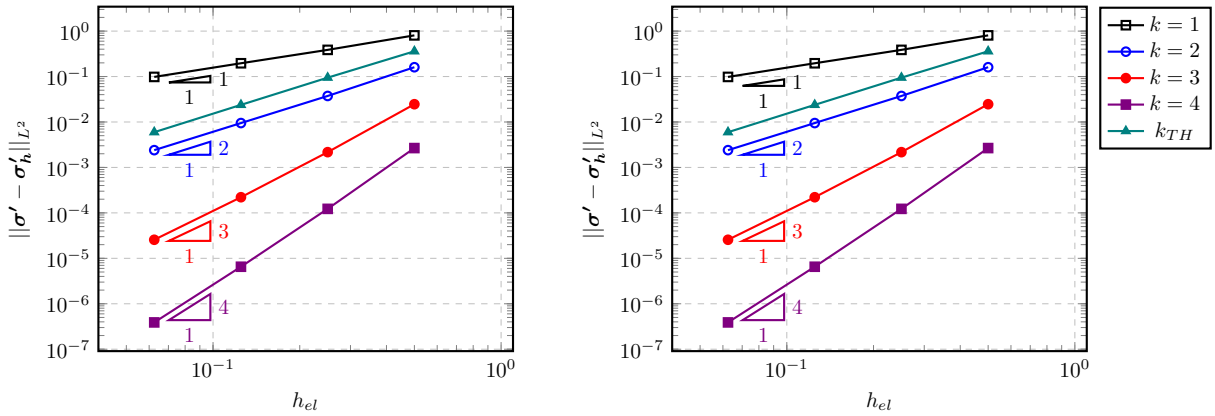

(a) Hdiv-C (b) Hidv-S

Figure 5.14: Two-dimensional verification test: convergence analysis for deviatoric stress.

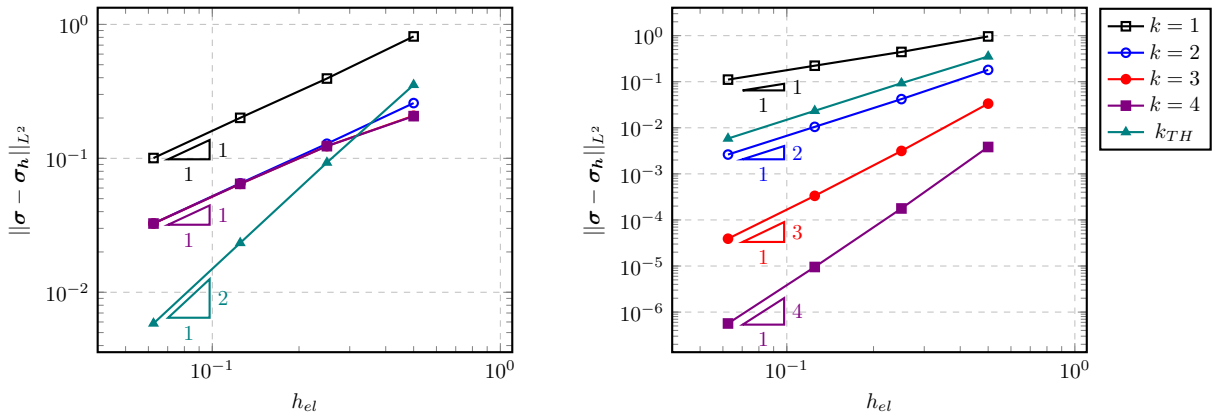

(a) Hdiv-C (b) Hidv-S

Figure 5.15: Two-dimensional verification test: convergence analysis for Cauchy stress.

The convergence rates shown in Figures 5.12 - 5.15 for all evaluated fields align with the expected rates presented in Table 5.1 for both methods. In comparison with Hdiv-C simulations,

Taylor-Hood simulations demonstrate superior performance in terms of pressure field errors. However, when compared to Hdiv-S, there is no difference in pressure errors between the two methods. On the other hand, for the velocity and deviatoric stress fields, the hybrid-hybrid formulation outperforms the Taylor-Hood formulation. Taylor-Hood element excel in the Cauchy stress field due to the influence of pressure. This advantage over Hdiv-C is not observed when compared to Hdiv-S.

The hybrid-hybrid formulation demonstrates its locally conservative property through the L^2-error norm of the velocity divergence, as shown in Table 5.2. The velocity field is perfectly divergence-free, resulting in an error close to machine precision for all simulations.

Table 5.2: L^2-error norms for the divergence of the velocity field for the manufactured solution.

$\|\|\nabla \cdot (u - u_h)\|\|_{L^2}$					
$k = 1$			$k = 2$		
N	**Hdiv-C**	**Hdiv-S**	**N**	**Hdiv-C**	**Hdiv-S**
2	6.60e-16	1.67e-14	2	7.81e-16	4.00e-14
4	8.83e-16	2.10e-14	4	9.14e-16	6.29e-14
8	1.13e-15	4.17e-14	8	1.30e-15	1.28e-13
16	2.14e-15	8.02e-14	16	2.36e-15	2.35e-13
$k = 3$			$k = 4$		
N	**Hdiv-C**	**Hdiv-S**	**N**	**Hdiv-C**	**Hdiv-S**
2	6.40e-16	1.37e-13	2	7.28e-16	3.13e-13
4	5.48e-16	4.51e-13	4	9.73e-16	8.32e-13
8	1.42e-15	7.52e-13	8	1.56e-15	1.58e-12
16	2.71e-15	1.66e-12	16	2.91e-15	3.15e-12

Taylor-Hood elements, however, are not locally conservative yielding significant errors for the divergence of the velocity field (see Table 5.3).

Table 5.3: L^2-error norms and rates of convergence for the divergence of the velocity field using Taylor-Hood elements (manufactured solution).

N	$\|\|\nabla \cdot (u - u_h)\|\|_{L^2}$	**Rate**
2	1.29245	-
4	0.38146	1.76
8	0.09922	1.94
16	0.02509	1.98

Although the quadratic rate of convergence is achieved, the error itself cannot be ignored.

Even with 16 elements per edge, the error in the velocity divergence is still around 0.025, which is significantly higher than the machine precision achieved in the hybrid-hybrid formulation simulations. This should be considered when approximating the Stokes equations in situations where local conservation is important.

5.2 Three-Dimensional Flows

Similar to the two-dimensional flows, the validation of three-dimensional problems is conducted using the Poiseuille and LDC flows, along with the well-established Annular Couette problem.

The three-dimensional Poiseuille flow is simulated within the unit cube $\Omega = [0, 1] \times [0, 1] \times [0, 1]$. Boundary conditions are an extension of the two-dimensional case, with normal stress ($(\boldsymbol{\sigma n}) \cdot \boldsymbol{n} = -10$) on the back surface, null normal stress ($(\boldsymbol{\sigma n}) \cdot \boldsymbol{n} = 0$) on the front surface, no-penetration ($\boldsymbol{u} \cdot \boldsymbol{n} = 0$) on the top, bottom, left and right surfaces, no-slip ($\boldsymbol{u} \cdot \boldsymbol{t} = 0$) on the top, bottom, back and front surfaces, and slip condition ($(\boldsymbol{\sigma n}) \cdot \boldsymbol{t} = 0$) on the left and right surfaces.

The analytical solution is similar to the two-dimensional case (eqs. (5.1) to (5.3)), with the non-null velocity component in the z-direction. The stress tensor is also extended to three dimensions. A mesh with 10 hexahedral elements per edge is used and viscosity μ is set to 1.

Results are depicted in Figs. 5.16 - 5.19.

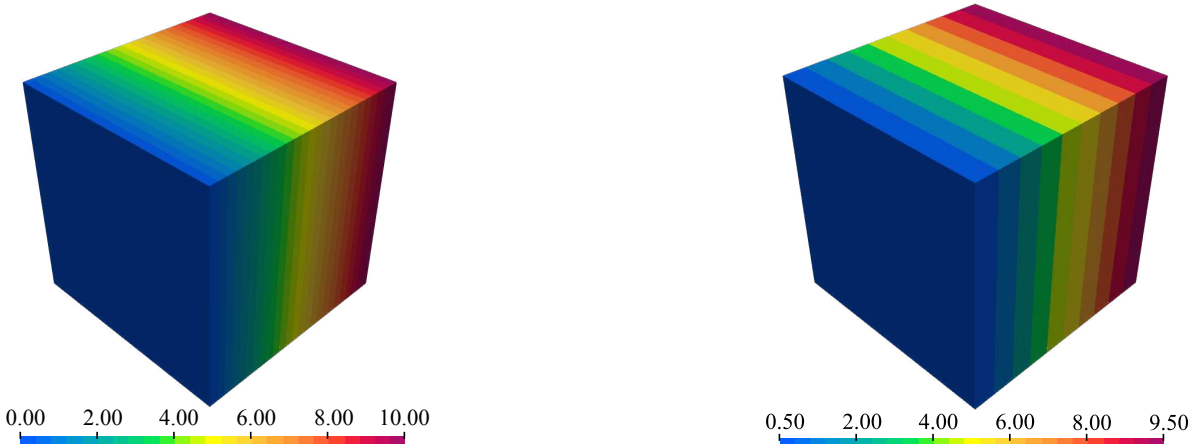

(a) Hdiv-S (b) Hdiv-C

Figure 5.16: 3D Poiseuille flow pressure field.

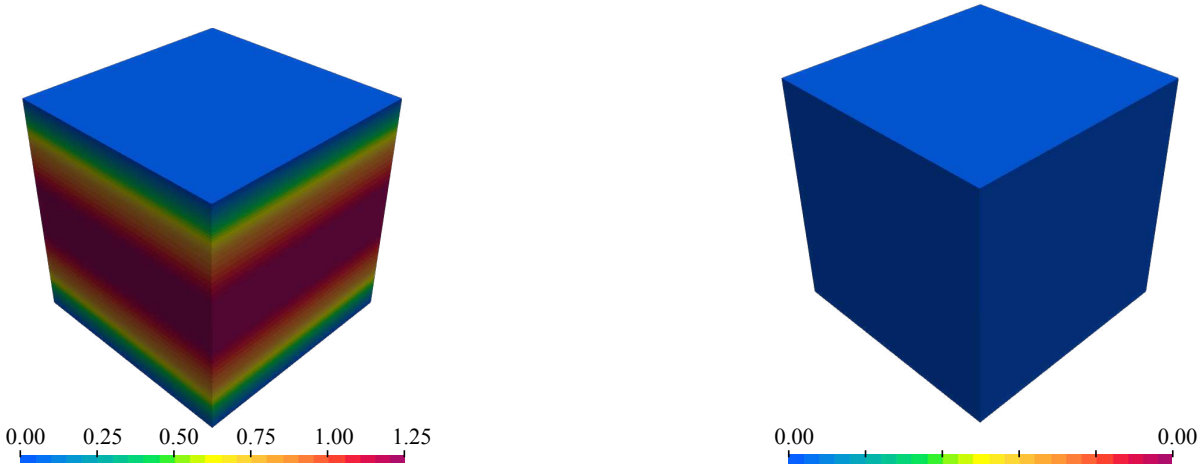

(a) u_z (b) u_x and u_y

Figure 5.17: 3D Poiseuille flow velocity field.

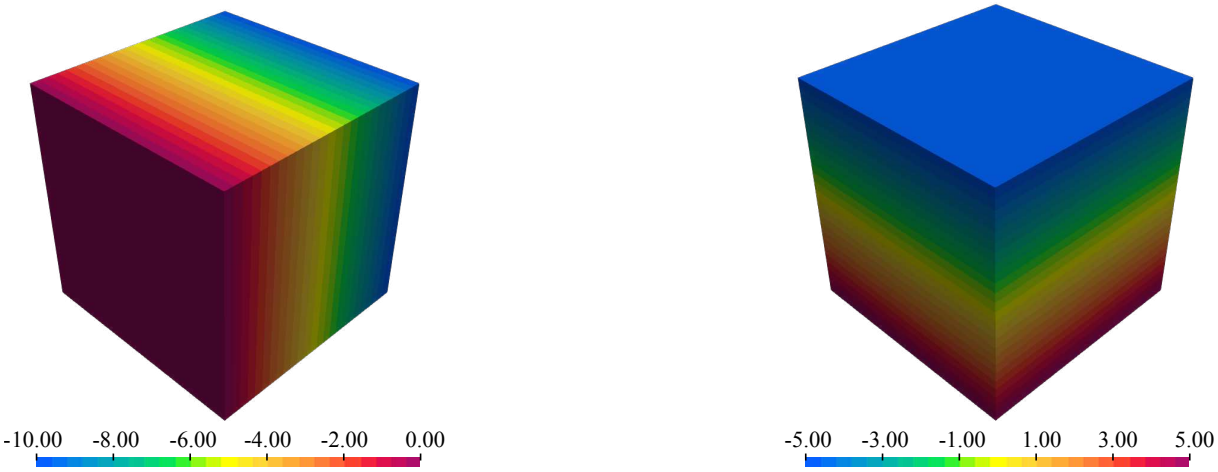

(a) σ_{xx}, σ_{yy}, and σ_{zz} (b) σ_{yz} and σ_{zy}

Figure 5.18: 3D Poiseuille flow stress field with Hdiv-S space.

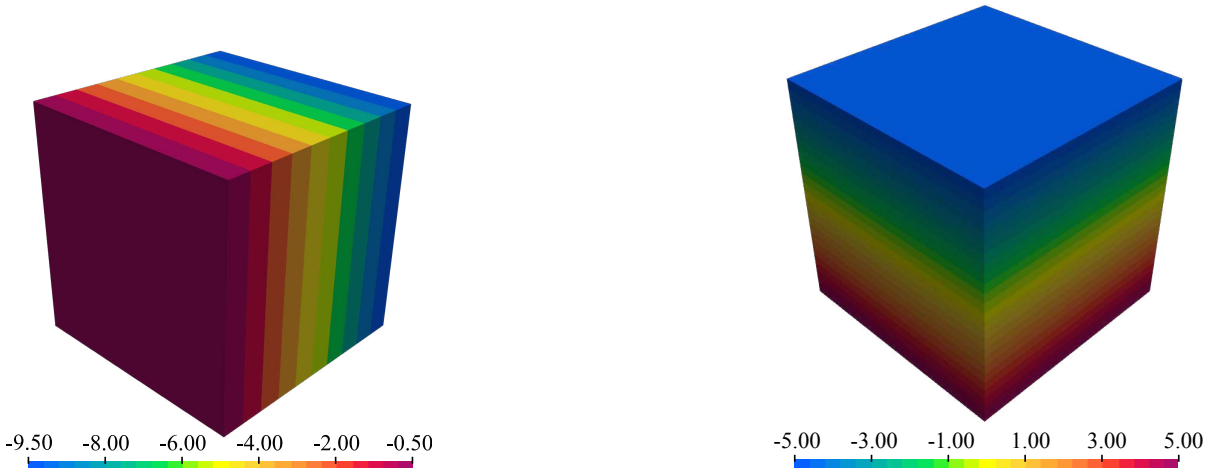

(a) σ_{xx}, σ_{yy}, and σ_{zz} (b) σ_{yz} and σ_{zy}

Figure 5.19: 3D Poiseuille flow stress field with Hdiv-C space.

Note that Poiseuille flows for two and three dimensions reach the same solution, which matches the analytical solution. The velocity field is equal for both Hdiv-S and Hdiv-C, while the pressure field is constant by element for Hdiv-C and smoother for Hdiv-S. The stress σ_{xy}, σ_{yx}, σ_{xz} and σ_{zx} are null, not being represented in the figures.

The LDC is simulated in three dimensions as well. The domain is the unit cube $\Omega = [0,1] \times [0,1] \times [0,1]$. Boundary conditions are no-penetration ($\boldsymbol{u} \cdot \boldsymbol{n} = 0$) on every surface, unit tangential velocity ($\boldsymbol{u} \cdot \boldsymbol{t} = -1$) on the top surface, slip ($\boldsymbol{\sigma n} \cdot \boldsymbol{t} = 0$) on the front, back and bottom surfaces, and no-slip condition ($\boldsymbol{u} \cdot \boldsymbol{t} = 0$) on the left and right surfaces (Figure 5.20).

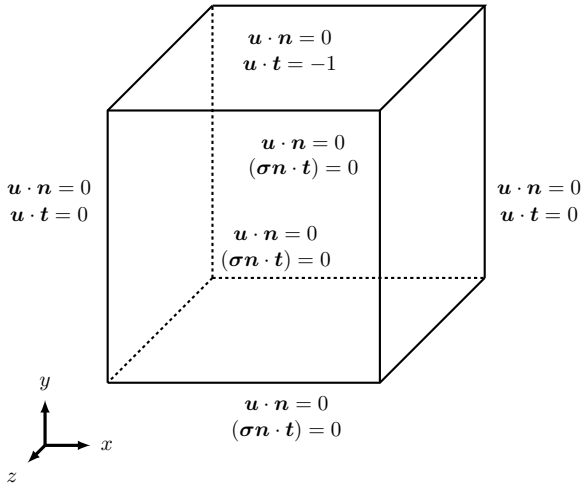

Figure 5.20: Domain and boundary conditions for the three-dimensional Lid-Driven Cavity problem.

The lid is dragged in the z-direction, and the domain is composed of 10 hexahedral elements per edge. Viscosity μ is set to 1 and results for pressure and velocity are depicted in Figure 5.21.

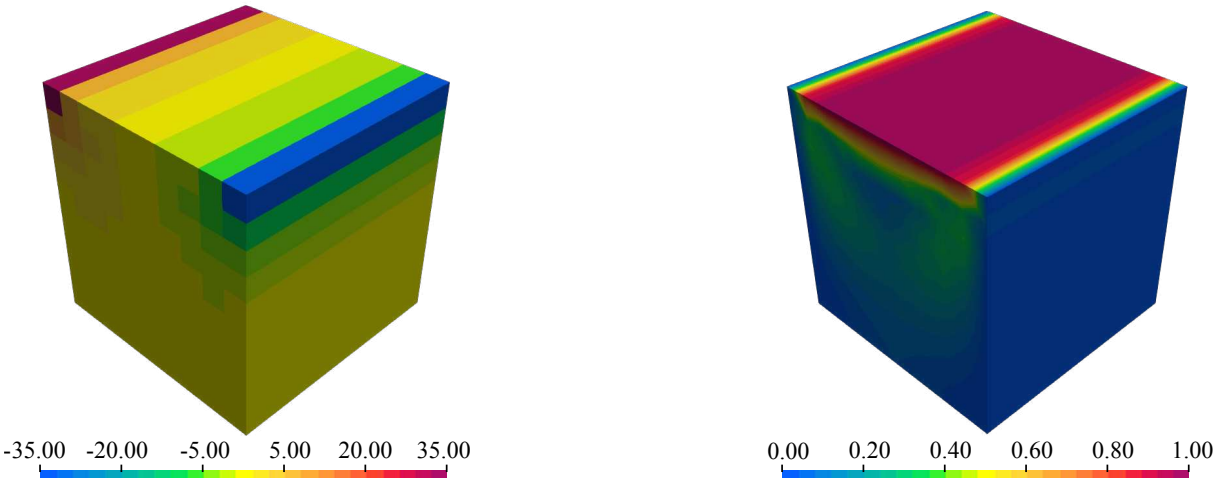

(a) Pressure. (b) Velocity.

Figure 5.21: 3D Lid-driven cavity results for Hdiv-C space.

As can be seen, the solution in the three-dimensional LDC is the same as in the two-

dimensional case. To verify the rate of convergence for the hybrid-hybrid formulation in three dimensions, the Annular Couette flow is used.

5.2.1 Convergence Analysis for Hexahedral Elements

Three-dimensional formulations' rates of convergence are verified using the Annular Couette flow problem. The problem involves two cylinders positioned concentrically. The inner cylinder is pushed in the z-direction with a constant velocity $v_{zinner} = v_\infty$, while the outer cylinder remains stationary with $v_{zouter} = 0$. As a result, the velocity profile in the radial direction follows a logarithmic pattern. The analytical solutions for the velocity and pressure can be described by equations (5.6) and (5.7), respectively

$$\boldsymbol{u} = v_\infty \left(\frac{\log\left(\frac{R_o}{r}\right)}{\log\left(\frac{R_o}{R_i}\right)} \right) \hat{\boldsymbol{k}}, \tag{5.6}$$

$$p = 1, \tag{5.7}$$

in which, r is the radial distance from the center of the annulus, R_o is the radius of the outer cylinder and R_i is the radius of the inner cylinder.

The domain is given by the annulus comprehended between the inner and outer cylinders, with $R_i = 1$ and $R_o = 2$. However, taking advantage of the symmetry of the problem, only a quarter of the annulus is simulated (see Figure 5.22). The boundary conditions are normal stress on the front and back surfaces ($\boldsymbol{\sigma n} \cdot \boldsymbol{n} = 1$), on every surface of the annulus, tangential velocity ($\boldsymbol{u} \cdot \boldsymbol{t}$) as a function of r is applied. Finally, on the inner, outer, and surfaces of symmetry the no penetration condition ($\boldsymbol{u} \cdot \boldsymbol{n} = 0$) is enforced.

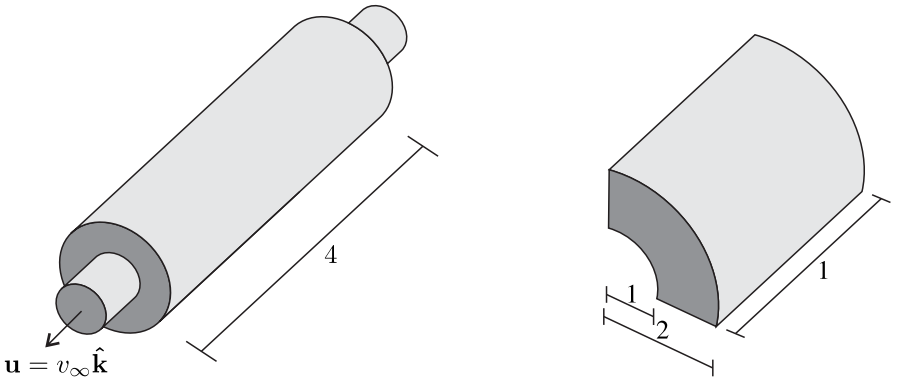

(a) Annular Couette Domain

(b) Annular Couette Domain

Figure 5.22: Domain for the three-dimensional verification test.

As in the two-dimensional test, the convergence analyses are performed for Hdiv-C and Hdiv-S over domains with $N = 2 \times 2 \times 2$, $N = 4 \times 4 \times 4$, $N = 8 \times 8 \times 8$, and $N = 16 \times 16 \times 16$

hexahedral elements per edge (see Fig. 5.23). The approximation order for the facet velocity is set to $k = 1, 2, 3, 4$. Viscosity is set to 1. Note that in the x and y-axis directions, the length of the domain is 1, which is taken into account to calculate the value of $h_e l$. For the Annular Couette flow problem, the average edge size is also given by $1/N$ due to the number of divisions in the x and y-axis directions.

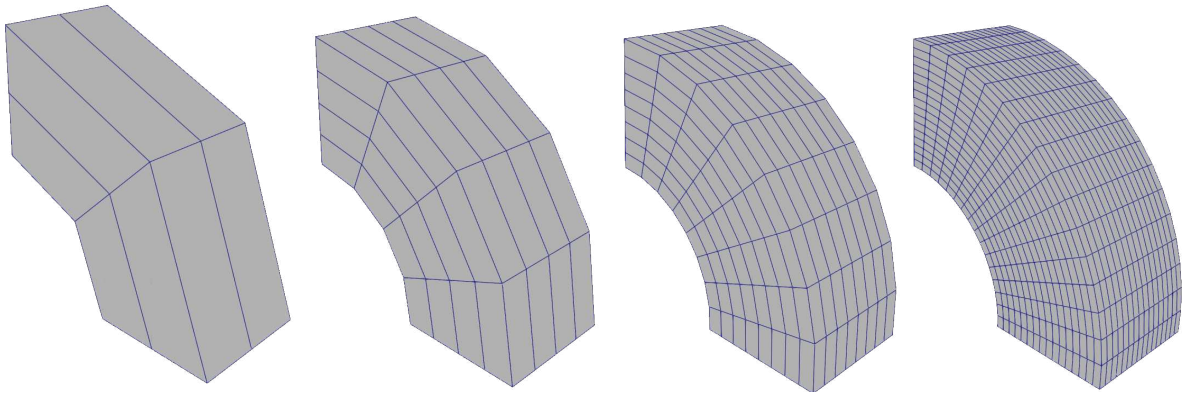

(a) $2 \times 2 \times 2$ Mesh. (b) $4 \times 4 \times 4$ Mesh. (c) $8 \times 8 \times 8$ Mesh. (d) $16 \times 16 \times 16$ Mesh.

Figure 5.23: Meshes for the three-dimensional verification test.

It is important to note that errors due to the circular geometry of the domain may affect the quality of the solution, especially for more poorly refined meshes (figures 5.23a and 5.23b, for instance). To avoid this issue, a transfinite interpolation developed in [56] is employed to ensure that the mesh has the same geometry at any level of refinement. This transfinite interpolation uses the ideas behind the Bilinearly Blended Coons Patches [57] to exactly represent the contours of domains described by analytic functions allowing the element topology to naturally fit the domain boundary.

In this context, Figure 5.24 shows the results for pressure and velocity fields in Hdiv-C simulations. Observe that a whole cylinder is depicted, since after the quarter is simulated, results are mirrored in the other quadrants of the annulus and the $z-$direction until the domain is complete.

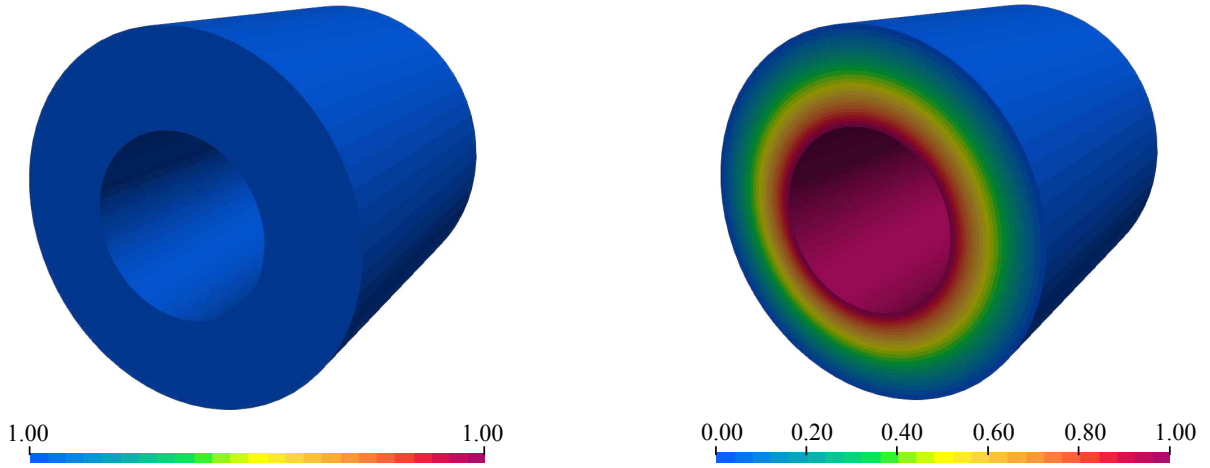

(a) Pressure field (b) Velocity field

Figure 5.24: Achieved solution for the three-dimensional problem using $k = 4$, hexahedral mesh with $N = 16$ elements per edge, and Hdiv-C space.

Since the pressure is constant in the whole domain, only the solution achieved by the Hdiv-C space is shown. The velocity field is the same for both spaces. The rates of convergence for the pressure, velocity, deviatoric stress, and the Cauchy stress fields are displayed in Figures 5.25 - 5.29, respectively.

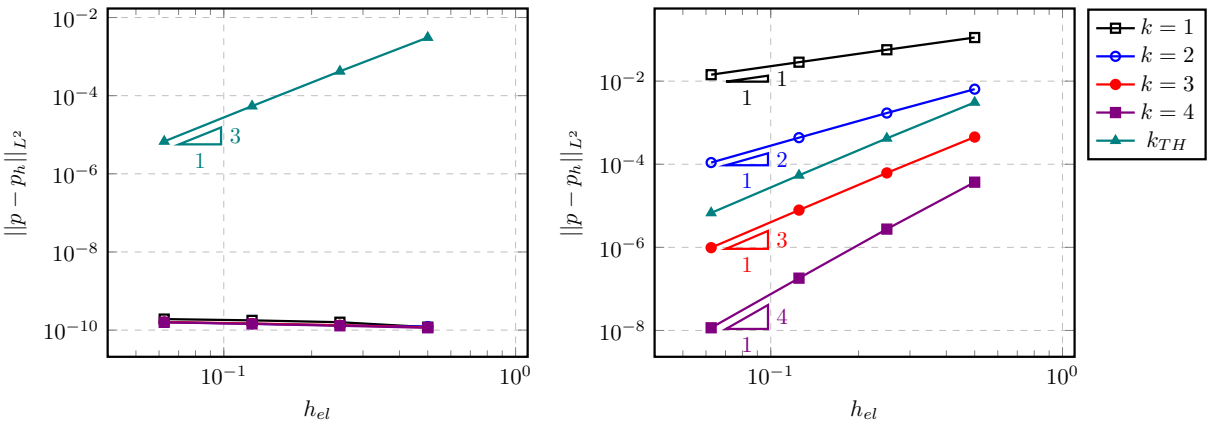

(a) Hdiv-C (b) Hidv-S

Figure 5.25: Three-dimensional verification test: Convergence analysis for pressure.

Because the exact solution is a subset of the shape functions used to approximate the pressure, the integral of the pressure field equals the mean pressure used in Hdiv-S static condensation. However, this pressure is not constant by element, which leads to the apparent different errors from the obtained with Hdiv-C. A way to directly compare both spaces is to analyze the error in the mean pressure field of the Hdiv-S (Figure 5.26).

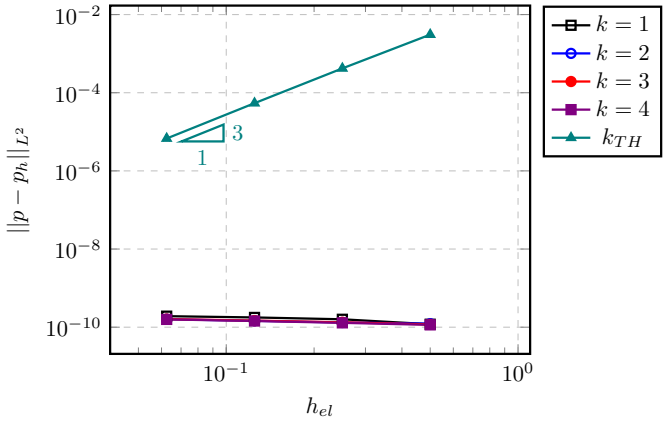

Figure 5.26: Three-dimensional verification test: Convergence analysis for the mean pressure field in Hdiv-S.

As shown by Figure 5.26, the error in the mean pressure field for Hdiv-S is similar to the error in the pressure field for Hdiv-C. The difference in the error between the pressure fields is due to reconstruction errors in the Hdiv-S space.

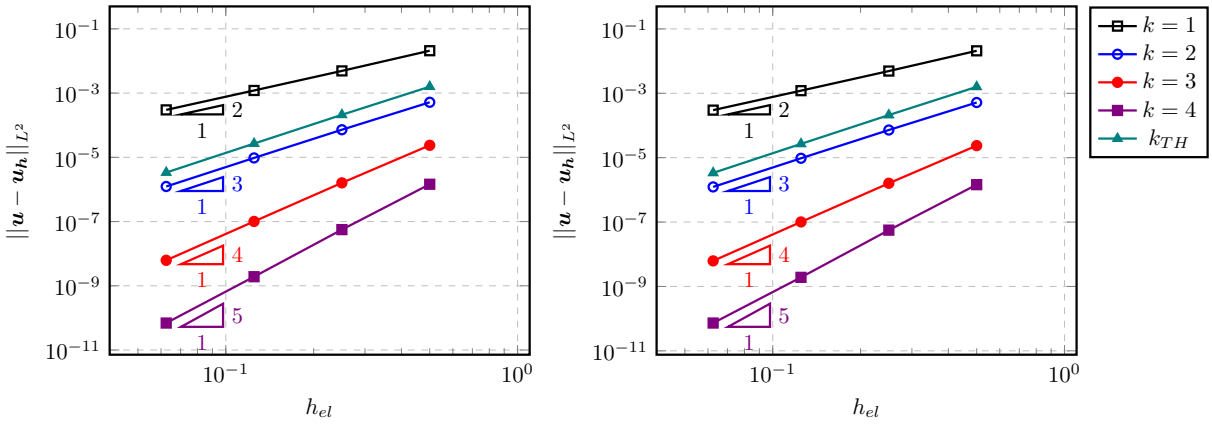

(a) Hdiv-C (b) Hidv-S

Figure 5.27: Three-dimensional verification test: Convergence analysis for velocity

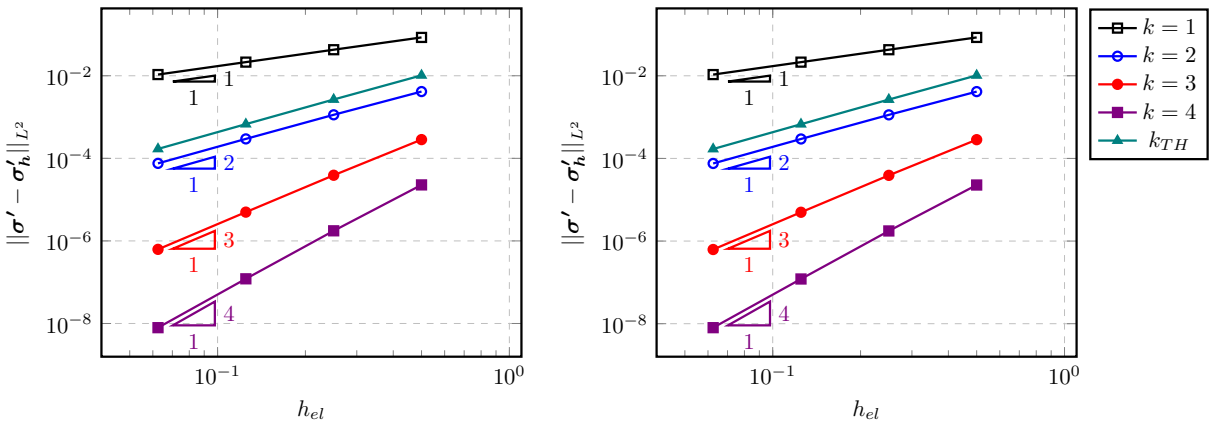

(a) Hdiv-C (b) Hidv-S

Figure 5.28: Three-dimensional verification test: Convergence analysis for deviatoric stress.

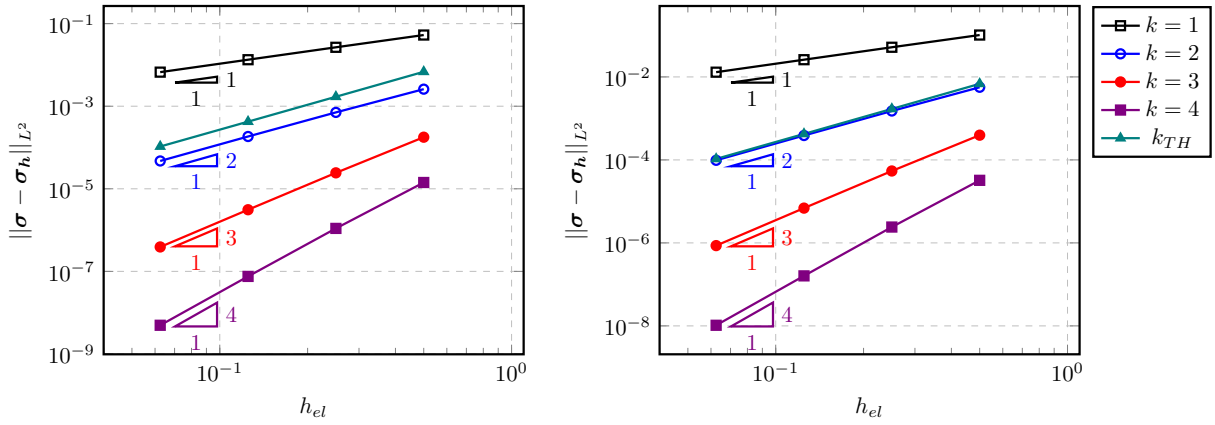

(a) Hdiv-C (b) Hidv-S

Figure 5.29: Three-dimensional verification test: Convergence analysis for stress.

For this three-dimensional problem, the convergence rates for pressure using the Hdiv-C space are super convergent (i.e. more precise than expected). This is possible because the analytical solution is included in the approximation space in the Hdiv-C space. The same is true for the convergence rates of the Taylor-Hood method. For other fields such as velocity and deviatoric stress, the Hdiv-C simulations perform better than Taylor-Hood, achieving the optimum convergence rates. For the Cauchy stress field, the results are similar between Hdiv-S and Taylor-Hood simulations, while Hdiv-C yields slightly better results.

Table 5.4 shows the errors for the divergence of the velocity, confirming that the formulation is locally conservative for three-dimensional problems. The error for the divergence of the velocity with Taylor-Hood simulations is also displayed in Table 5.5.

Table 5.4: L^2-error norms for the divergence of the velocity field for the Annular-Couette flow.

$\|\|\nabla \cdot (u - u_h)\|\|_{L^2}$					
$k = 1$			$k = 2$		
N	**Hdiv-C**	**Hdiv-S**	**N**	**Hdiv-C**	**Hdiv-S**
2	5.62e-16	1.37e-13	2	5.96e-16	3.76e-13
4	1.775e-15	1.74e-13	4	1.83e-15	7.84e-13
8	6.58e-15	3.31e-13	8	6.68e-15	1.33e-12
16	2.52e-14	6.99e-13	16	2.53e-14	2.35e-12
$k = 3$			$k = 4$		
N	**Hdiv-C**	**Hdiv-S**	**N**	**Hdiv-C**	**Hdiv-S**
2	6.53e-16	7.56e-12	2	7.12e-16	1.34e-11
4	1.90e-15	1.16e-11	4	2.01e-15	2.25e-11
8	6.77e-15	2.44e-11	8	6.91e-15	4.50e-11
16	2.55e-14	5.38e-11	16	2.56e-14	9.95e-11

Table 5.5: L^2-error norms and rates of convergence for the divergence of the velocity field using Taylor-Hood elements (Annular Couette flow).

N	$\|\|\nabla \cdot (u - u_h)\|\|_{L^2}$	**Rate**
2	1.69e-3	-
4	3.26e-4	2.37
8	5.76e-5	2.50
16	1.01e-5	2.52

The findings for the Stokes flow align with the results obtained in the previous section. The convergence rate for both two- and three-dimensional problems is in agreement with the expected rates. These outcomes confirm the validity of the hybrid-hybrid method and demonstrate its effectiveness in accurately and reliably solving Stokes' problems.

The number of DoFs in Hdiv-C simulations is considerably smaller than in Hdiv-S simulations. The following section aims to quantitatively compare both spaces in terms of error and DoF number.

5.3 Comparison Between Hdiv-C and Hdiv-S

The main reason to employ Hdiv-C space is that by the intrinsic process of its space creation (Section 3 of [34]), the space has considerably fewer DoFs than the Hdiv-S space. Although both spaces have the same number of equations in the condensed system, the Hdiv-C space has a considerably smaller number of global DoFs. This leads to a faster solution process, which is particularly important for large-scale problems. Additionally, in situations where the pressure field is constant by element, such as in Darcy flows, the Hdiv-C space is a better choice.

Table 5.6 shows the comparison between the number of DoF for the Hdiv-C and Hdiv-S spaces for the two-dimensional with manufactured solution aforementioned.

Table 5.6: Comparison between the number of DoF for the Hdiv-C and Hdiv-S spaces for the manufactured solution problem.

$k=1$				$k=2$			
N	**Before Condensation**		**After Condensation**	**N**	**Before Condensation**		**After Condensation**
	Hdiv-C	**Hdiv-S**			**Hdiv-C**	**Hdiv-S**	
2	92	220	40	2	160	360	64
4	344	856	136	4	600	1400	216
8	1328	3376	496	8	2320	5520	784
16	5216	13408	1888	16	9120	21920	2976
$k=3$				$k=4$			
N	**Before Condensation**		**After Condensation**	**N**	**Before Condensation**		**After Condensation**
	Hdiv-C	**Hdiv-S**			**Hdiv-C**	**Hdiv-S**	
2	236	524	88	2	320	712	112
4	888	2040	296	4	1208	2276	376
8	3440	8048	1072	8	4688	10960	1360
16	13536	31968	4064	16	18464	43552	5152

Note that the Taylor-Hood element is also included in the comparison. When the error is analyzed as a function of the number of DoFs, the expected rates of convergence for pressure and velocity are given by eqs. (5.8) and (5.9).

$$\text{Rate}_p \propto \frac{k}{\text{dim}}, \tag{5.8}$$

$$\text{Rate}_{\boldsymbol{u}} \propto \frac{k+1}{\text{dim}}, \tag{5.9}$$

in which dim is the simulation dimension. Figures 5.30 and 5.31 show the number of DoF after condensation versus the error for the pressure and velocity fields, respectively. Recall that the rate of convergence for pressure in Hdiv-C simulations is proportional to $k = 1$, for any polynomial order.

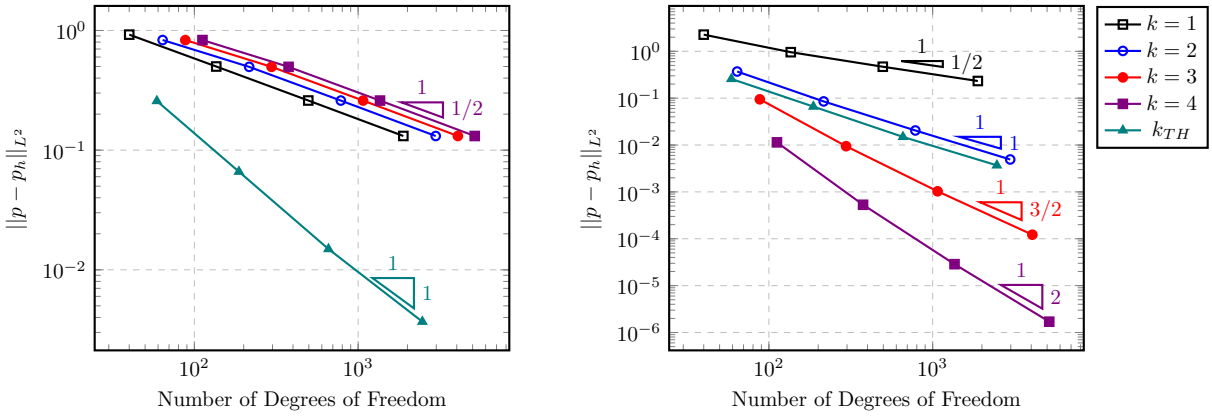

(a) Hdiv-C (b) Hidv-S

Figure 5.30: Two-dimensional comparison between the number of DoF for pressure solution.

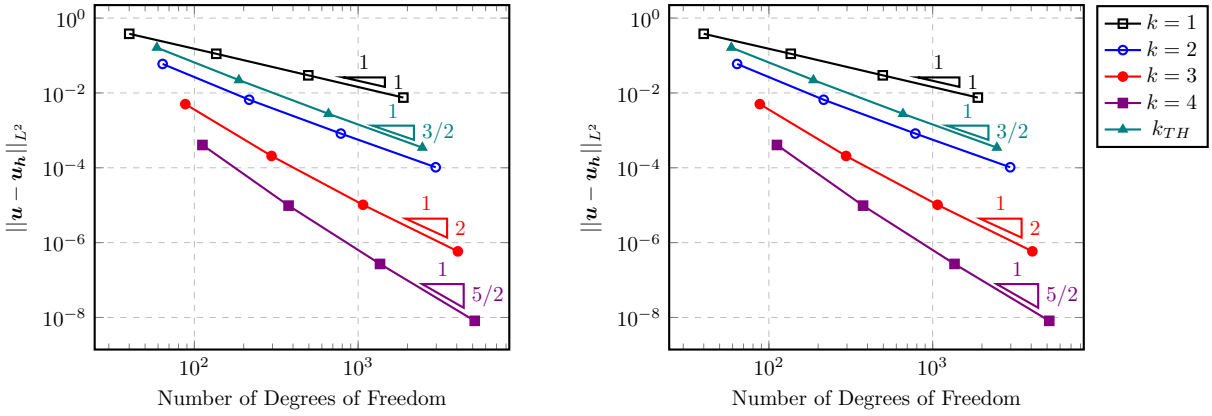

(a) Hdiv-C (b) Hidv-S

Figure 5.31: Two-dimensional comparison between the number of DoF for pressure solution.

Taylor-Hood elements yield, for the same number of equations, a smaller error for pressure than the hybrid-hybrid formulation. Treating velocity, however, the errors for hybrid-hybrid are smaller than the ones obtained by Taylor-Hood. Also, notice that there is a significant reduction (around 40%) in the number of degrees of freedom of Hdiv-S in comparison to Hdiv-C. This fact cannot be neglected when dealing with large-scale problems, especially in three-dimensional simulations, which are computationally more demanding than two-dimensional ones.

The analysis is repeated for the Annular Couette problem, where the number of DoFs for the Hdiv-C and Hdiv-S spaces are compared in Table 5.7. In three-dimensional problems, the reduction in DoFs is even more significant, ranging from 50% to almost 60% compared to the Hdiv-S space.

Table 5.7: Comparison between the number of DoF for the Hdiv-C and Hdiv-S spaces for the Annular Couette flow.

$k=1$				$k=2$			
N	**Before Condensation**		**After Condensation**	**N**	**Before Condensation**		**After Condensation**
	Hdiv-C	**Hdiv-S**			**Hdiv-C**	**Hdiv-S**	
2	968	1992	224	2	2412	4412	620
4	7456	15648	1504	4	18480	34480	4144
8	58496	124032	10880	8	144576	272576	29888
16	463360	987648	82432	16	1143552	2167552	226048
$k=3$				$k=4$			
N	**Before Condensation**		**After Condensation**	**N**	**Before Condensation**		**After Condensation**
	Hdiv-C	**Hdiv-S**			**Hdiv-C**	**Hdiv-S**	
2	4696	8152	1232	2	7916	13404	2060
4	35936	63584	8224	4	60592	104496	13744
8	280960	502144	59264	8	473792	825024	99008
16	2221568	3991040	448000	16	3746560	6556416	748288

Figures 5.32 and 5.34 show the number of DoFs after condensation versus the error for the pressure and velocity fields, respectively for three-dimensional simulations.

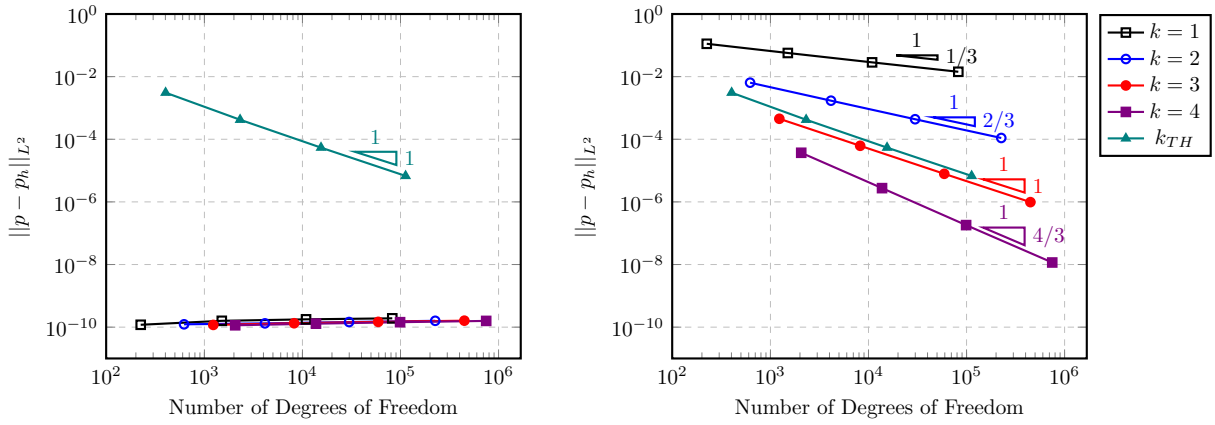

(a) Hdiv-C

(b) Hidv-S

Figure 5.32: Three-dimensional comparison between the number of DoF for pressure solution.

As explained before, the pressure error for Hdiv-S, in this case, is higher due to errors during the pressure field reconstruction from a mean pressure field. To better compare the two spaces, the error in the mean pressure field for Hdiv-S is depicted in Figure 5.33.

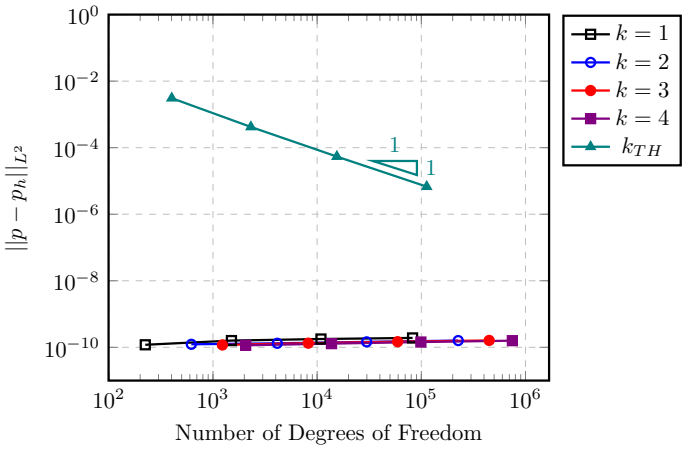

Figure 5.33: Three-dimensional verification test: Convergence analysis for the mean pressure field in Hdiv-S.

As expected, the error in the mean pressure field for Hdiv-S is of the same order of magnitude as the error in the pressure field for Hdiv-C.

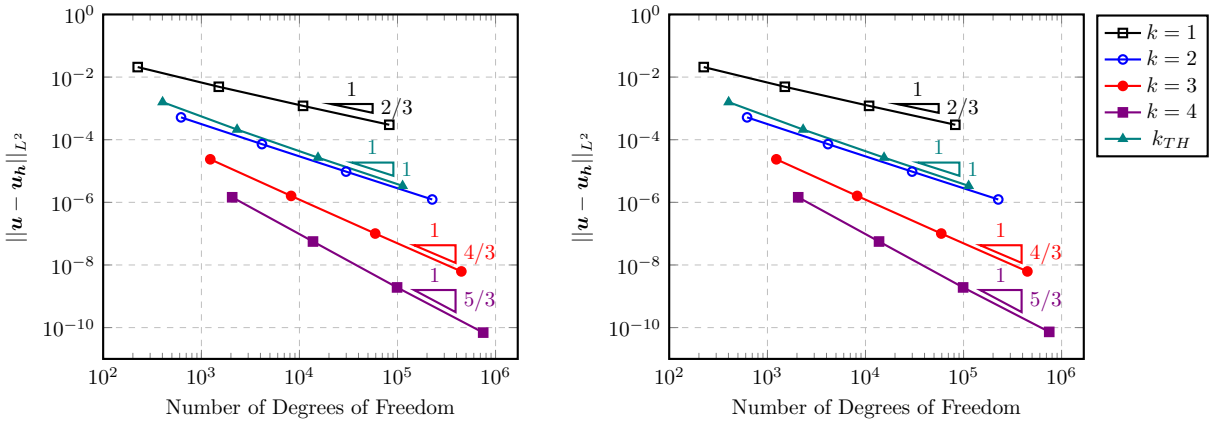

(a) Hdiv-C (b) Hidv-S

Figure 5.34: Three-dimensional comparison between the number of DoF for velocity solution.

The hybrid-hybrid formulation with the Hdiv-C space demonstrates superior performance in terms of both pressure and velocity accuracy. However, it is important to note that the analytical solution for pressure is a subset of the shape functions used in the Hdiv-C space, which may have significantly influenced the results. For the Taylor-Hood formulation, even the rate of convergence seems to be higher than expected, closer to the Hdiv-S results for $k = 3$, instead of $k = 2$.

In terms of velocity, the hybrid-hybrid formulation achieves smaller errors compared to the Taylor-Hood method. However, it is worth mentioning that the difference between Taylor-Hood and hybrid-hybrid formulation results for the three-dimensional analysis is less pronounced than in the two-dimensional case. To summarize, for the same number of equations, the double-hybrid formulation achieved smaller errors for the velocity field than Taylor-Hood, which is

observed in two- and three-dimensional problems. For pressure, the hybrid-hybrid formulation does not perform better than the Taylor-Hood method in either two- or three-dimensional problems.

5.4 Robustuness Tests

This section aims to demonstrate the robustness of the proposed method when solving Stokes problems. The examples are chosen to illustrate the range of Stokes' problems that can be solved using the hybrid-hybrid formulation in many scientific and engineering fields.

5.4.1 Flow past a NACA Profile

The National Advisory Committee for Aeronautics (NACA) was an American agency developed to incentivize, coordinate and institutionalize aeronautical research. The NACA airfoil series is a set of airfoil shapes widely employed in aircraft design. More about the NACA airfoil and its series can be found in [58, 59].

The velocity involving a NACA airfoil does not configure a low Reynolds number regime and therefore is not properly represented by the Stokes equations. However, simulations herein intend to demonstrate the range of problems in which the hybrid-hybrid formulation can be applied to solve Stokes equations. A general idea of the behavior of a wind tunnel test can be drawn, and the method's capacity to deal with voids inside its domain is also verified.

The simulation is carried out in a two-dimensional control volume, involving the NACA airfoil profile. The domain is represented in Figure 5.35. Although the profile is modeled and simulated without units or specific dimensions, the outer domain is 16 units long and 4 units high at its maximum height. The NACA profile is 10 units long and 3.32 units high at its maximum height.

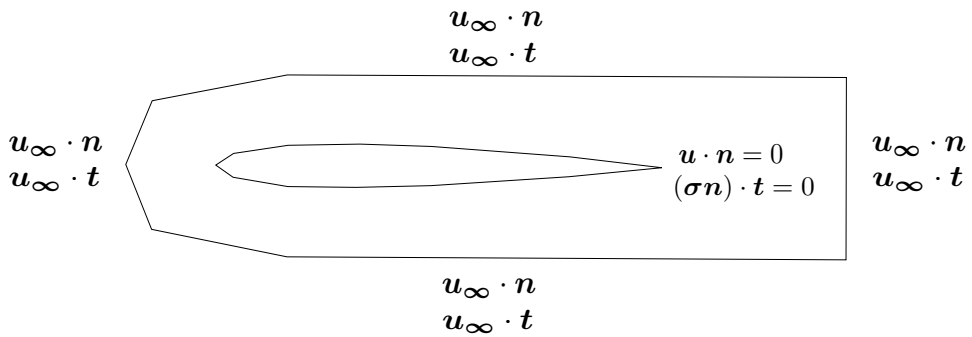

Figure 5.35: Domain for the flow past a NACA profile.

On the profile, no-penetration ($\boldsymbol{u} \cdot \boldsymbol{n} = 0$) and slip condition ($\boldsymbol{\sigma n} \cdot \boldsymbol{t} = 0$) are imposed. On every edge of the outer domain, normal and tangential velocities are imposed so that $\boldsymbol{u_\infty} = \{\frac{\sqrt{2}}{2}, \frac{\sqrt{2}}{2}\}$. The viscosity is set to 1, and the polynomial order for the facet velocity is $k = 2$.

The mesh is unstructured (see Figure 5.36), and the element size is defined to suit the NACA profile's dimensions.

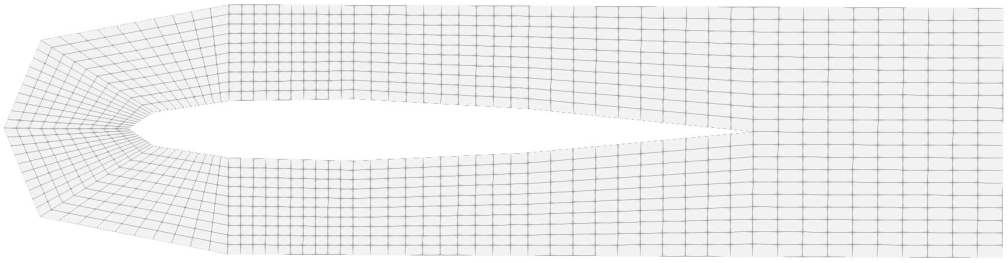

Figure 5.36: Mesh for the flow past a NACA profile.

Figure 5.37 shows the results for the pressure and velocity fields.

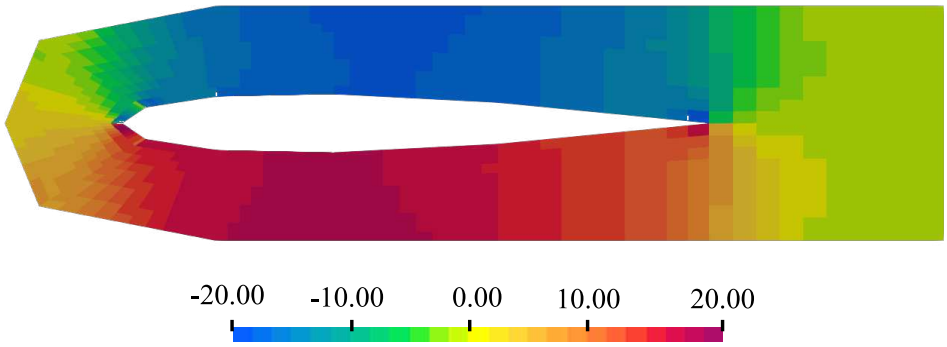

(a) Pressure field.

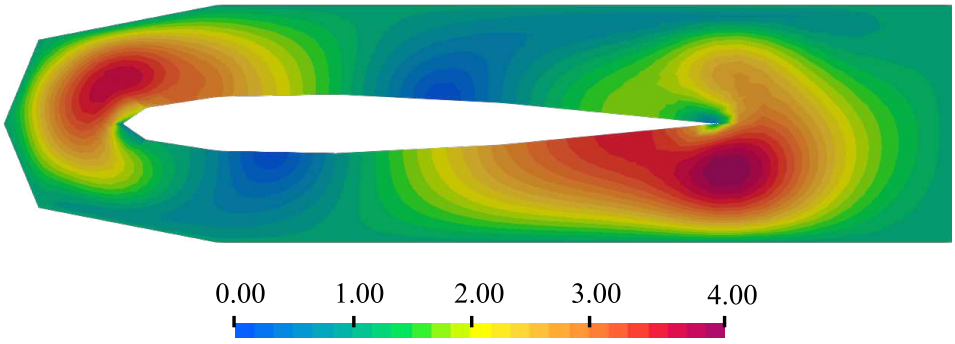

(b) Velocity magintude field.

Figure 5.37: Flow past a Naca profile.

The algorithm not only demonstrates to deal with void regions inside the domain but also represents the NACA profile's response accurately. Results are consistent with the expected behavior of a low Reynolds number fluid flow, with an increase in the velocity in the upper and lower regions around the NACA, followed by a smooth decrease in the outlet region.

5.4.2 Flow through Serpetine's Channels

Stokes flow can be adapted to analyze micromixers in lab-on-chip devices, widely employed in medicine, biological and chemical engineering. Due to the scale of micromixers, usually μm

to mm, they mix one or more fluid streams that are usually under a laminar regime.

Passive mixers mix these streams without any external source, only by the mechanism of the micromixer itself. Inspired by the micromixer's geometries described in [60,61], two serpentine channels are simulated in this section.

The first serpentine, a two-dimensional sinusoidal serpentine, is given by Eq. (5.10)

$$y(x) = 0.8 \sin\left(\frac{2\pi x}{\lambda}\right), \tag{5.10}$$

in which $\lambda = 2.658$ mm. The Serpentine's dimensions and boundary conditions considered for this simulation are depicted in Fig. 5.38. The channel has two inlets and one outlet. On the left of the serpentine, there is a t-shaped inlet on which a normal pressure is applied ($(\boldsymbol{\sigma n})\cdot\boldsymbol{n} = 10$). On the right, there is a straight channel with a normal stress boundary condition ($(\boldsymbol{\sigma n})\cdot\boldsymbol{n} = 0$). The perimeter of the serpentine has no-slip boundary conditions ($\boldsymbol{u}\cdot\boldsymbol{t} = 0$) and on the top and bottom of the sinusoidal channel no-penetration is enforced ($\boldsymbol{u}\cdot\boldsymbol{n} = 0$). Viscosity is set to 1.

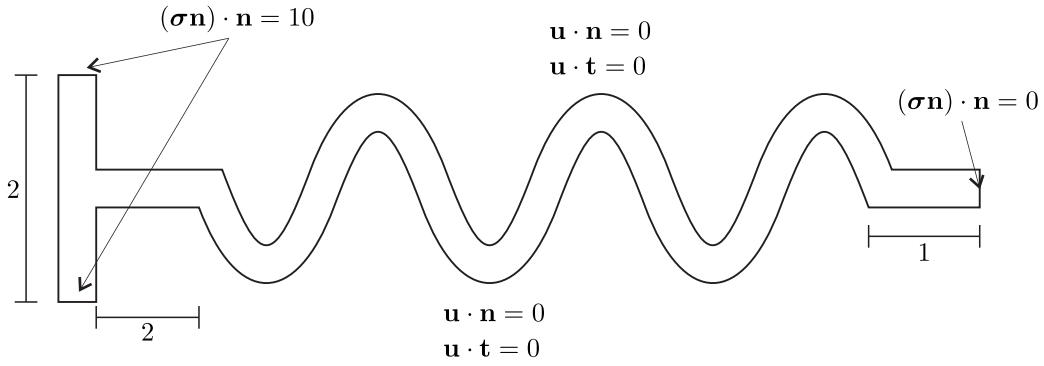

Figure 5.38: Sinusoidal serpentine's geometry and boundary conditions.

Figure 5.39 depicts the results for pressure and velocity fields. It is noted that a velocity profile similar to the Poiseuille flow is achieved within the channel, including the characteristics of the pressure gradient. The results are qualitatively consistent with the expected behavior of a low Reynolds number fluid flow.

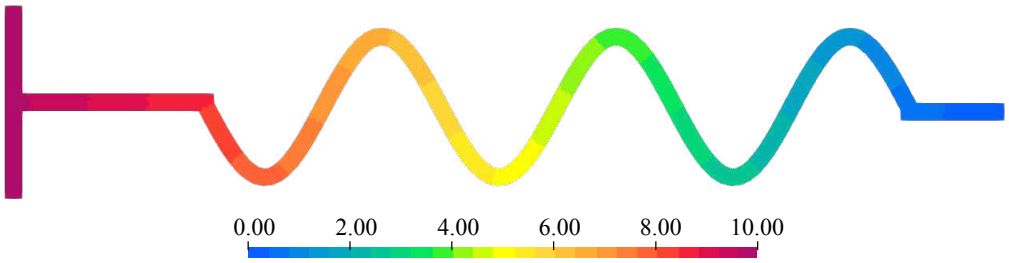

(a) Pressure field.

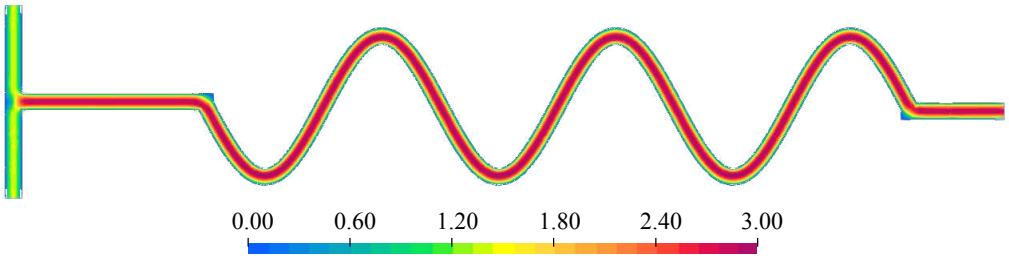

(b) Velocity magnitude.

Figure 5.39: Flow through a 2D serpentine.

The velocity field is then divided into its X and Y components (Figure 5.40). The X component is null in vertical sections of the channel, the same the Y component is null in horizontal sections. Note that, in the apex of the sinusoidal curve, at the point where flow is expected to be totally horizontal, the Y-velocity is null. It is also observed a symmetry in the Y component results, with values with the same magnitude, but in opposite directions.

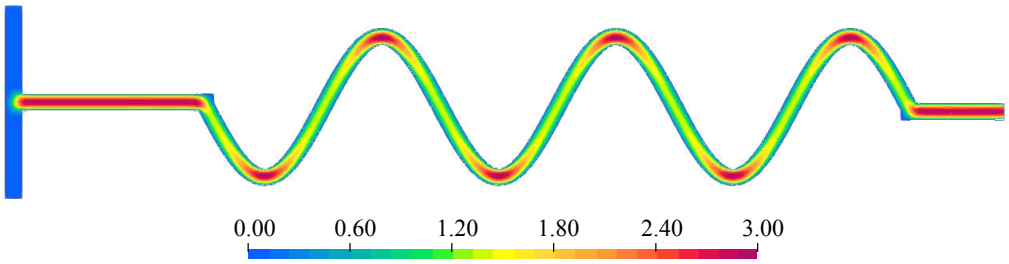

(a) u_x.

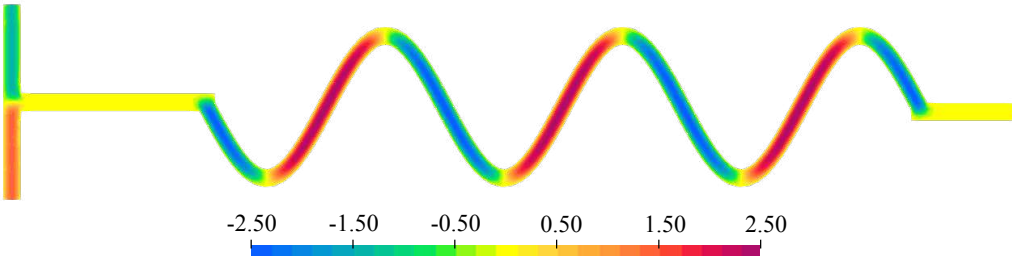

(b) u_y.

Figure 5.40: Velocity components X and Y for the 2D serpentine.

A "bumped" version of the previous serpentine is analyzed as well. Two behaviors are here studied: the velocity increases when the channel's cross-section shrinks keeping the flow rate constant (Figure 5.41), and the pressure gradient between two consecutive bumps (Figure 5.42).

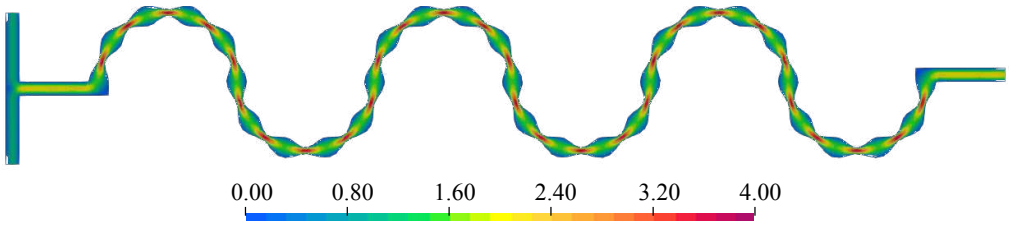

Figure 5.41: Velocity magnitude through a bumped 2D serpentine.

As expected, at the point in which the cross-section area decreases to half, the velocity doubles.

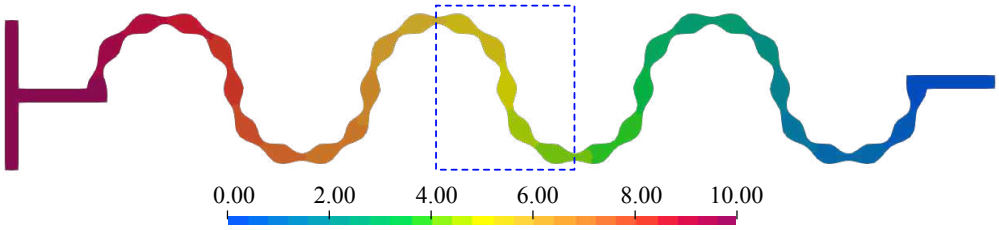

(a) Pressure field.

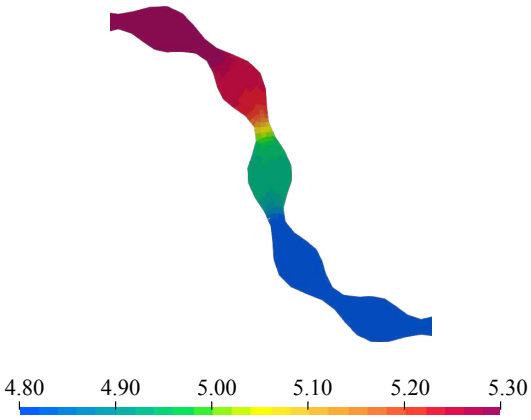

(b) Pressure between bumps.

Figure 5.42: Pressure field through a bumped 2D serpentine.

Between two bumps there is a pressure gradient, small in comparison to the pressure drop in the serpentine's channel as a whole. The pressure gradient is more pronounced in the region where the channel's cross-section is smaller, as expected.

The last serpentine analyzed is a three-dimensional C-shaped serpentine. The following BCs are imposed: no-slip ($\boldsymbol{u} \cdot \boldsymbol{t} = 0$) on every face of the channel, inlet normal stress ($\boldsymbol{\sigma n} \cdot \boldsymbol{n} = 10$), outlet normal stress ($\boldsymbol{\sigma n} \cdot \boldsymbol{n} = 0$), and no-penetration ($\boldsymbol{u} \cdot \boldsymbol{n} = 0$) on the remaining, as depicted in Fig. 5.43.

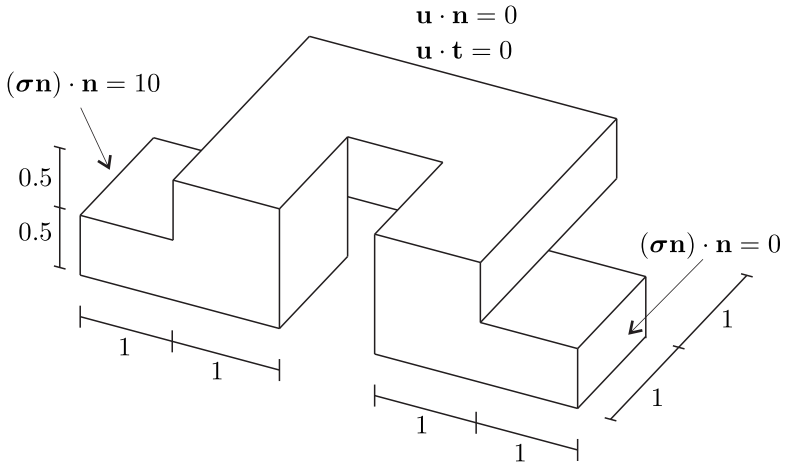

Figure 5.43: C-shaped serpentine's geometry and boundary conditions.

Results are depicted in Figure 5.44.

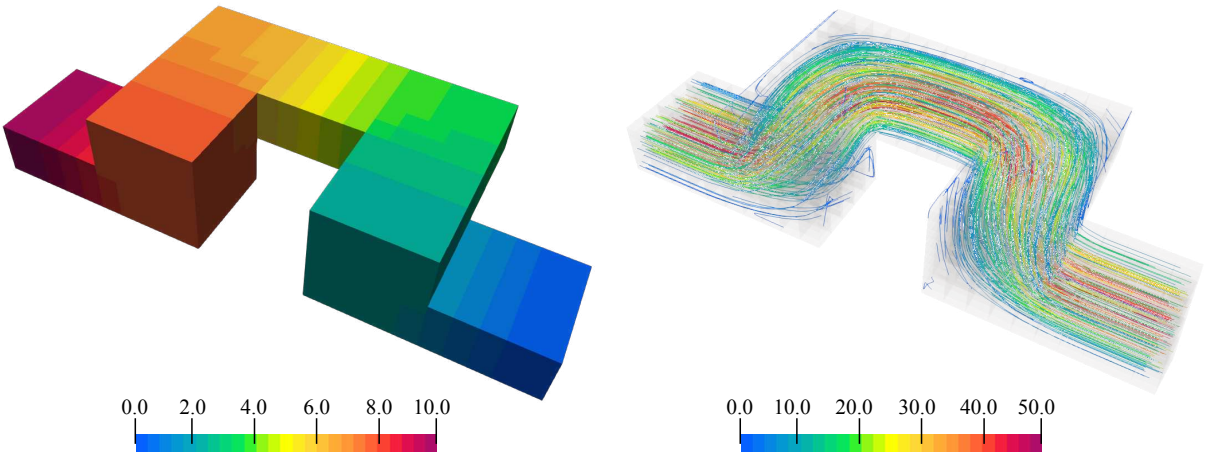

(a) Pressure field. (b) Streamlines for velocity magnitude ($\times 10^{-4}$).

Figure 5.44: C-shaped serpentine results.

The streamlines are shown for the 3D case. It is noted that the flow can pass through the channel even when a different height level is imposed. At the corners, a region of low velocity is observed. The higher the Reynolds number of the flow gets, the more pronounced the vorticity in these regions would become if the full Navier-Stokes equations were to be solved.

Chapter 6

Flow through Obstructed Domains

This chapter presents the framework developed to generate and simulate obstructed domains. First, details of the implementation are discussed. The Gmsh [62] API for Python is used to generate the mesh with obstructions. The code is structured in Object-Oriented Programming (OOP) to facilitate the generation of different types of obstructions. A father class *TPZModuleTypology* (Figure 6.1) is developed to generate the basis of the mesh geometry, i.e., the unobstructed cylinder, given geometric parameters such as radius and length.

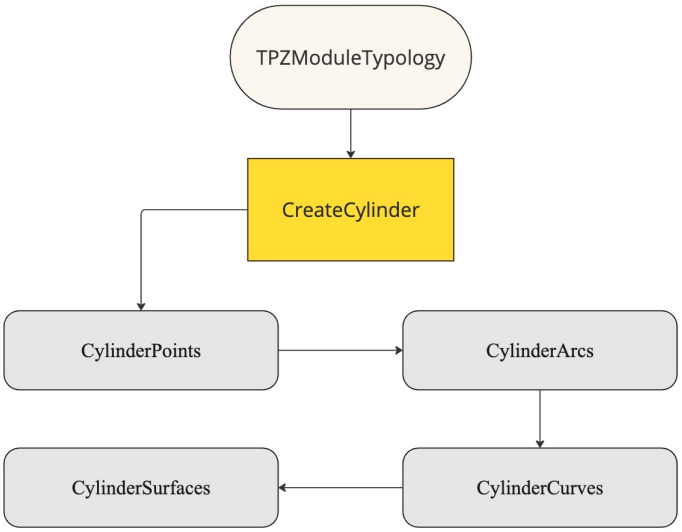

Figure 6.1: Class diagram for the *TPZModuleTypology* class.

The *TPZModuleTypology* class is inherited by the classes that create the obstructions. This way, the obstruction is inserted in a previously conceived geometry, regardless of the obstruction type, avoiding code repetition (see an example in Figure 6.2). A total of 4 geometries are implemented: circular, cross, semi-arcs, and no obstruction. Note, however, that the code is designed to be easily extended to other types of obstructions. New obstructions can be created by modifying the methods *ObstructionPoints*, *ObstructionArcs*, and *CreateObstruction*. If necessary, the obstruction's geometry can be checked by the method *CheckTopology*. The classes aforementioned can be found in Appendix A.

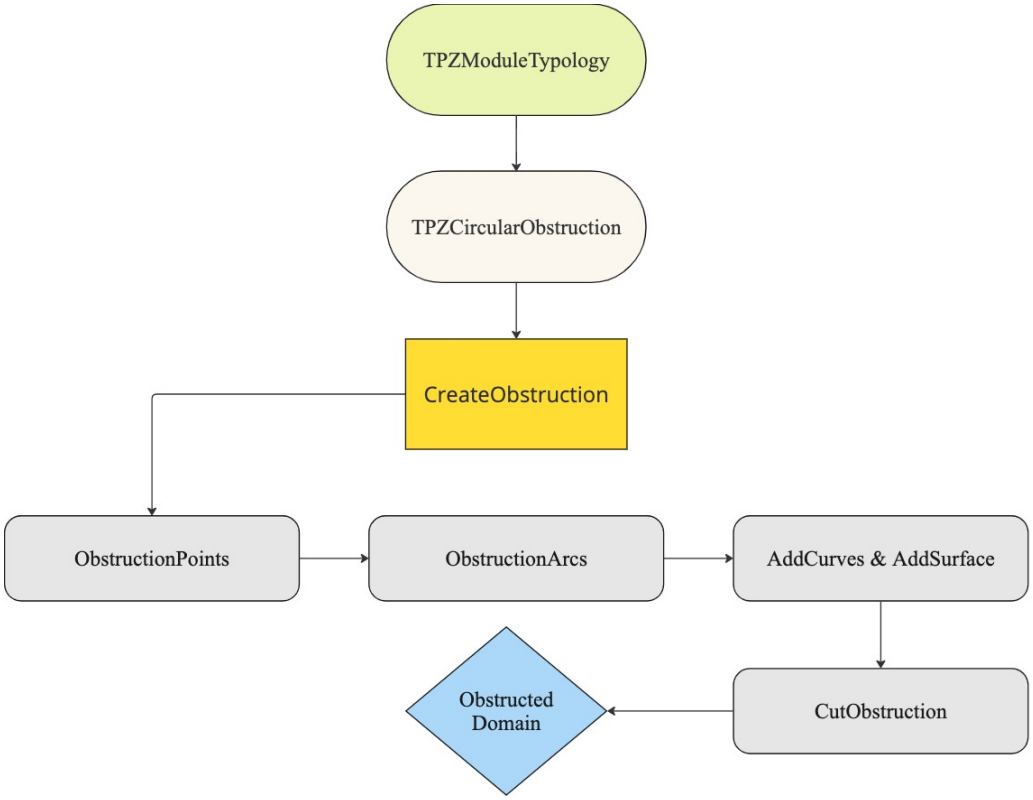

Figure 6.2: Class diagram for an obstruction class.

All simulations are performed using the following BCs: no-slip on every wall ($\boldsymbol{u} \cdot \boldsymbol{t} = 0$), inlet and outlet normal stress ($(\boldsymbol{\sigma n}) \cdot \boldsymbol{n} = 10$ and $(\boldsymbol{\sigma n}) \cdot \boldsymbol{n} = 0$, respectively), and no-penetration along the channel's axis ($\boldsymbol{u} \cdot \boldsymbol{n} = 0$). The obstructions are placed at the center of the channel, and the flux is not allowed to pass through them ($\boldsymbol{u} \cdot \boldsymbol{n} = 0$ and $\boldsymbol{u} \cdot \boldsymbol{t} = 0$).

Filtering methods are developed in the TPZMeshOperator (Section 4.6.2) to remove the equations of velocity related to the obstructions, which do not allow the fluid to pass through them. These methods seek the elements that have the obstruction's material ID and remove the corresponding equations from the global system. A version of the same function can be used when a null normal or tangential velocity is required.

Each channel has a unit length and radius and viscosity is also set to $\mu = 1$ (see Figure 6.3). The simulations are performed using the hybrid-hybrid formulation. When the obstructions are shown, the domain's opacity is set to 0.0015 to allow better visualization of the obstruction's geometry.

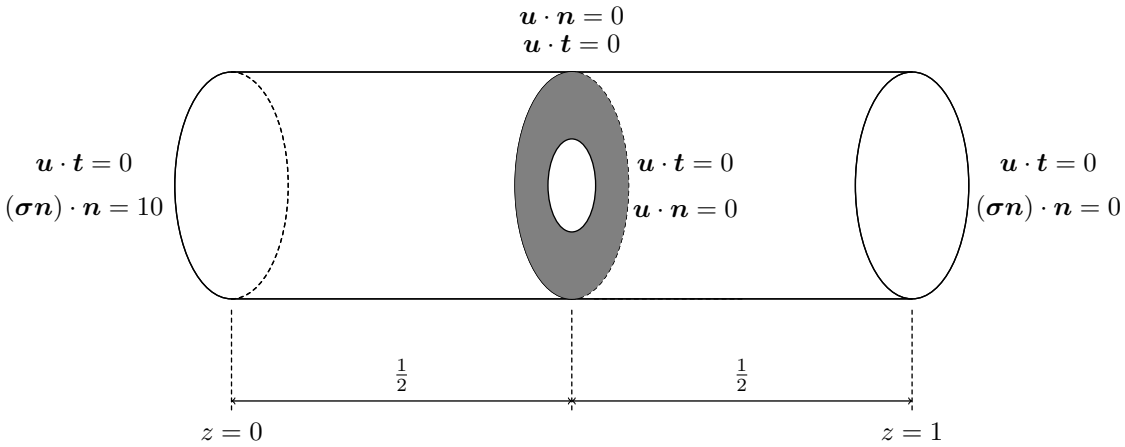

Figure 6.3: Obstructed domain: geometry and boundary conditions.

Although non-unitary values are applied as BC, the quantities do not have a physical meaning, which is the reason why the physical units are not presented. Recall that the behavior of the flow is the main focus of this work, once the Stokes equations are linear and any scaling factor can be applied to the variables.

6.1 Obstructed Domain Examples

Three types of obstructions are implemented to evaluate the flow behavior in obstructed domains: circular, cross, and semi-arcs. The following sections show the results obtained for each type of obstruction. Section 6.1.3 presents the results for cases in which multiple obstructions are inserted in the domain.

6.1.1 Circular Gap

The first obstruction implemented is a circular gap, in which the flow is allowed to pass only through a circular region in the center of the channel. Figure 6.4 shows the geometry of the circular gap.

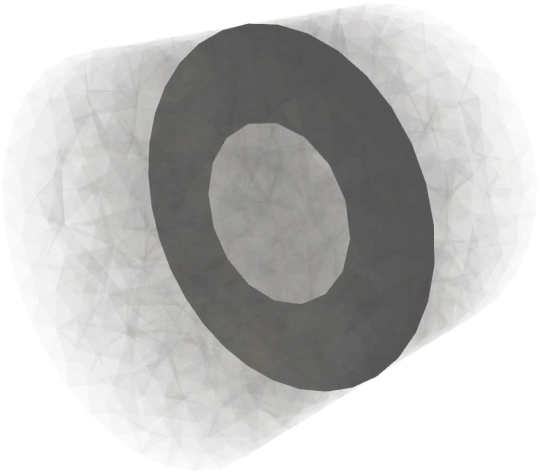

Figure 6.4: Geometry of the circular obstruction.

The pressure field and the streamlines are both depicted in Figure 6.5. Since the boundary conditions applied impose a normal stress of 10 at the inlet and 0 at the outlet, the most noticeable pressure drop occurs at the circular obstruction. The streamlines show that the flow is accelerated as it passes through the circular region.

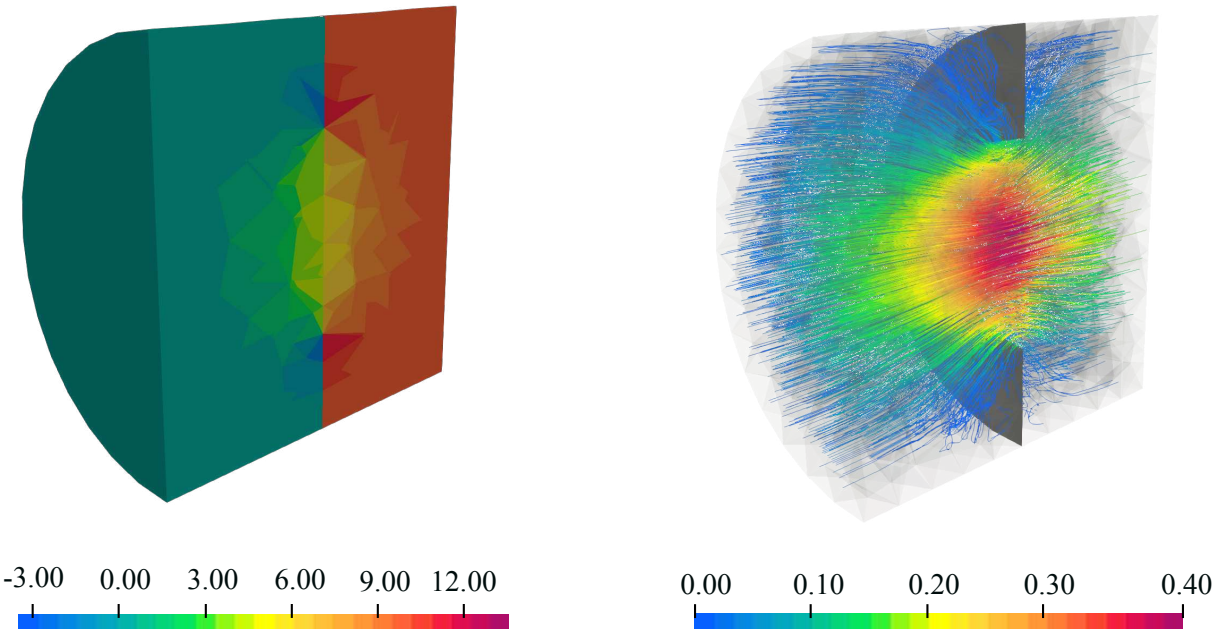

(a) Pressure field.

(b) Streamlines.

Figure 6.5: Results for circular obstruction.

A second analysis is performed to evaluate the flow pattern when multiple circular gaps are inserted in the domain. The gaps are placed symmetrically in the middle of the domain, but the same can be done randomly. The results for the pressure field and streamlines are shown in Figure 6.6.

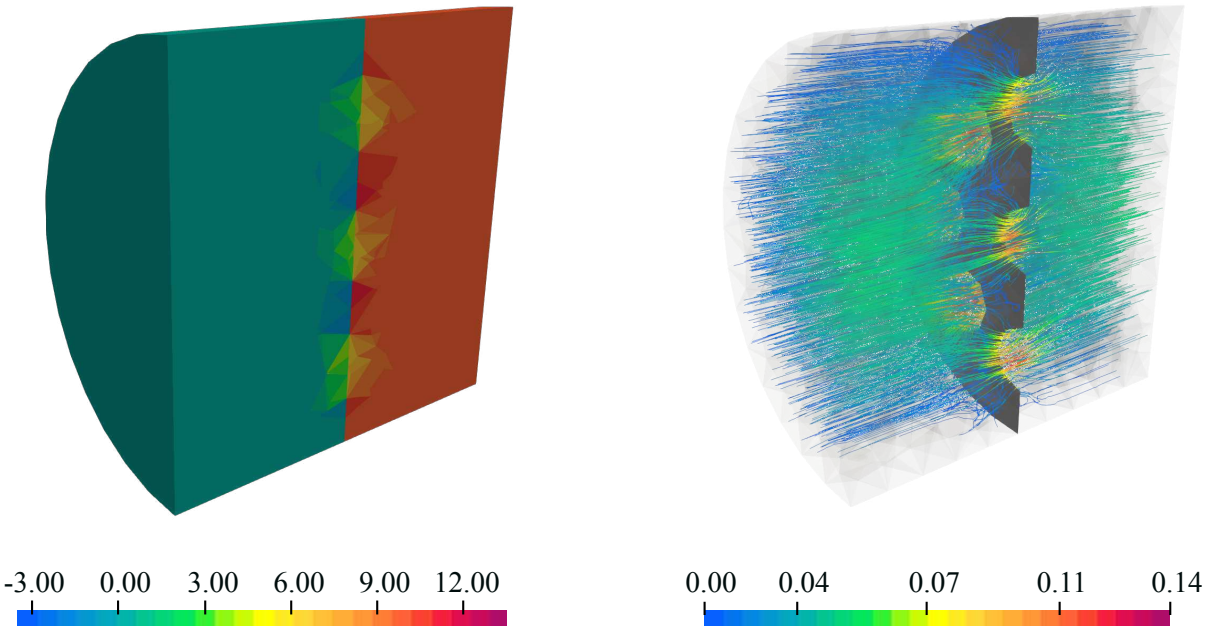

(a) Pressure field. (b) Streamlines.

Figure 6.6: Results for multiple circular obstructions.

An analysis of the influence of the gap's size on the flow behavior is presented in Section 6.1.4.

6.1.2 Cross Obstructions

The cross-shape obstruction is the second type of obstruction implemented. An example of the geometry of the cross obstruction is shown in Figure 6.7.

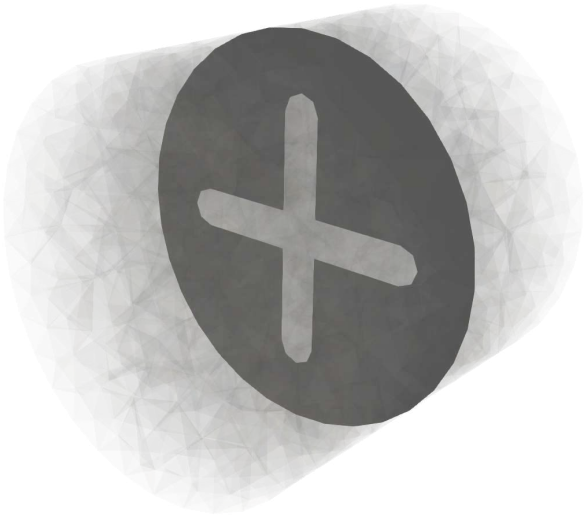

Figure 6.7: Geometry of the cross obstruction.

The pressure field and streamlines are shown in Figure 6.8.

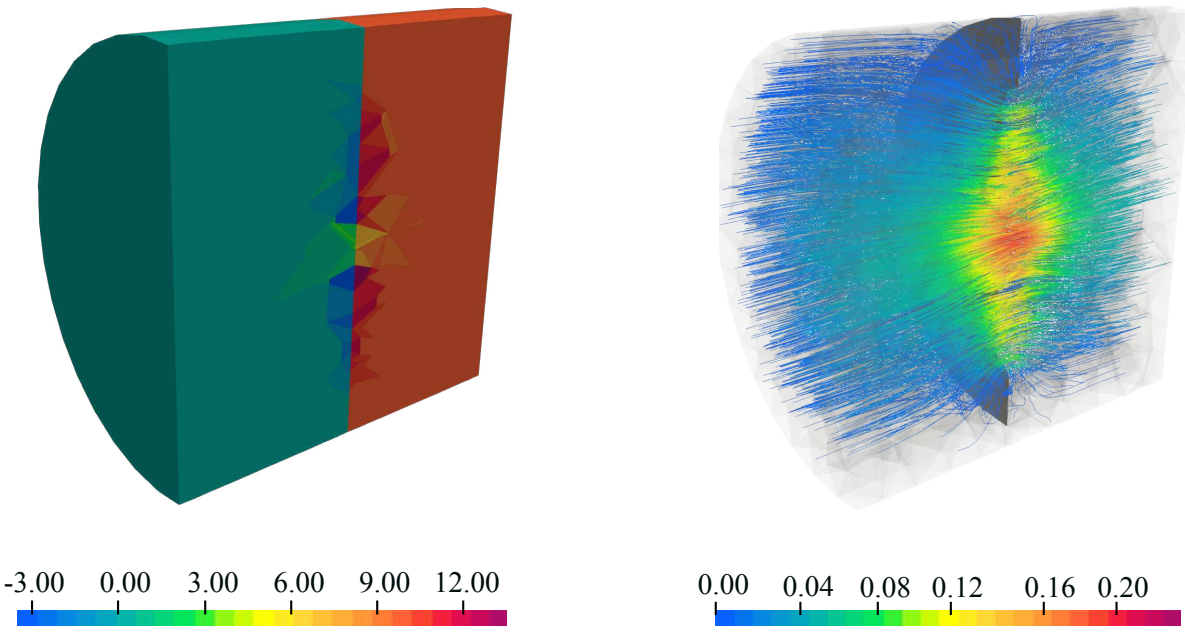

(a) Pressure field.

(b) Streamlines.

Figure 6.8: Results for cross obstruction.

This example shows that the algorithm is capable of generating more complex geometries than a simple circle. As mentioned, the OOP structure allows the code to be easily extended to other geometries by creating new classes that inherit the *TPZModuleTypology* class and share the same methods. The following section presents cases in which the domain is composed of more than one type of obstruction.

6.1.3 Multiple Obstructions

Domain with multiple obstructions are easily generated by creating separated modules for each obstruction, and then merging them into a single mesh. Figure 6.9 shows the geometry of two examples: one with two circular obstructions and another with different types of obstructions.

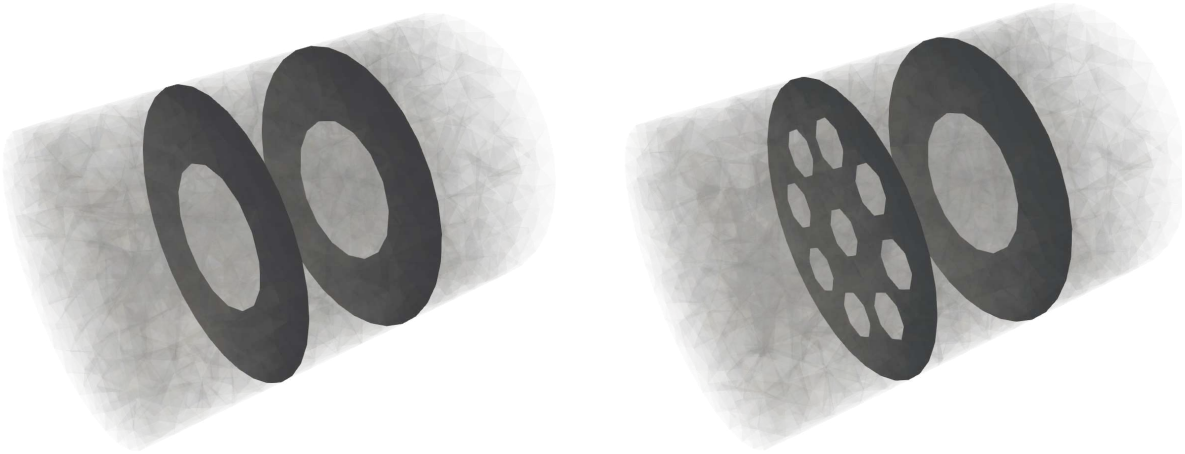

(a) Two circular obstructions. (b) Different obstructions.

Figure 6.9: Geometry of the domain with multiple obstructions.

The *Gmsh* software allows the module to be created and merged without overlapping the surfaces and volumes, which is fundamental for the mesh to be correctly generated. The results for the flow within a domain with two circular obstructions are shown in Figure 6.10.

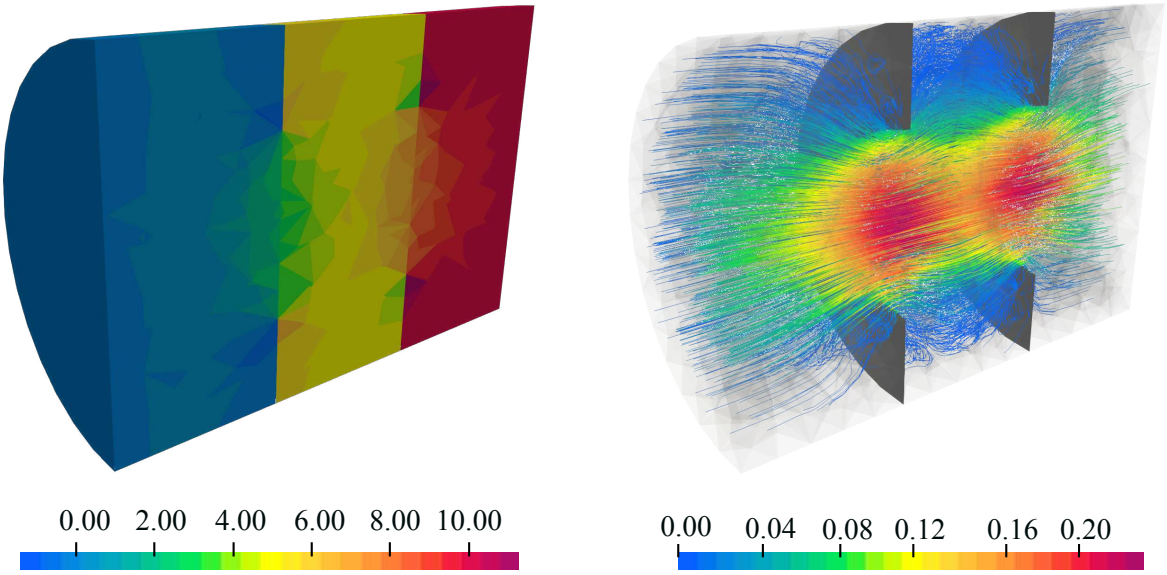

(a) Pressure field. (b) Streamlines.

Figure 6.10: Results for two circular obstructions.

Figure 6.11 depicts the pressure field and streamlines for a domain with one obstruction with a circular gap and another with multiple circular gaps placed in one-third and two-thirds of the channel's length, respectively. Note the division of the flow while passing through the obstructions.

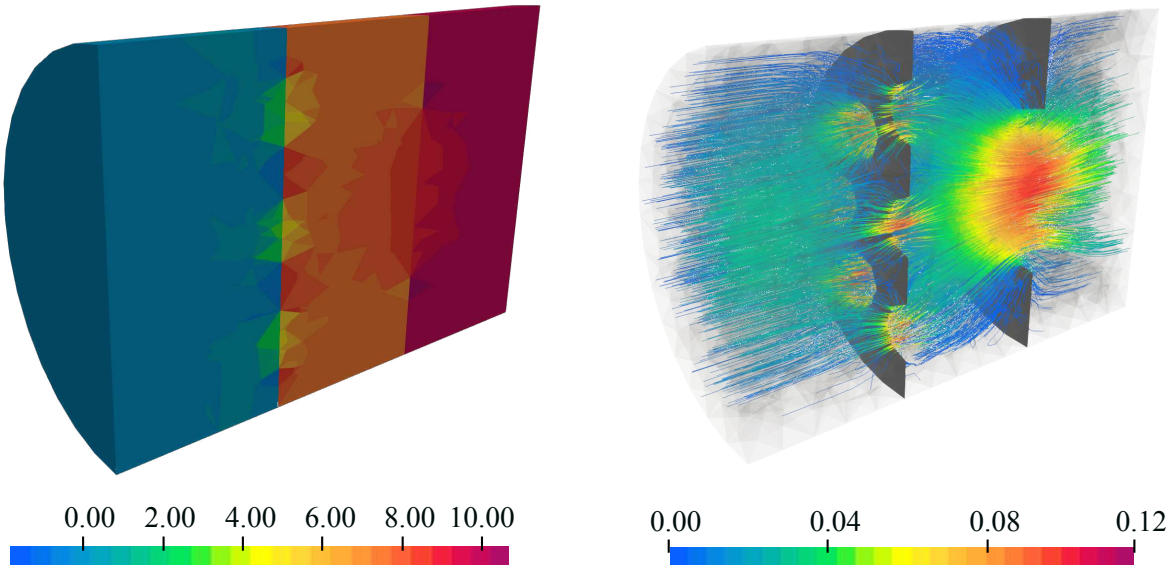

(a) Pressure field. (b) Streamlines.

Figure 6.11: Results for two different obstructions.

The results showed in Sections 6.1.1 - 6.1.3 demonstrate that the mesh generation algorithm is robust and capable of creating obstructions with different types of geometries. The flow behavior is consistent with the expected behavior, which points out that the hybrid-hybrid formulation is also capable of simulating, qualitatively, the flow through obstructed domains. Further analyses can be performed to evaluate the impact of different obstructions on the flow, designing new and optimal geometries that return the desired pressure drop between the modules of the in-scale prototype.

6.1.4 The Influence of the Obstruction's on the Flow

This section aims to evaluate the influence of the obstruction's size on the flow behavior. The domain is composed of an 80 cm long channel with a 9 cm diameter. A single circular obstruction is placed at the center with a radius varying from 1 to 4 cm. Fluid viscosity is set to 1. The BCs are the same as the ones presented in Figure 6.3, with the difference that the normal stress at the inlet is unitary.

The case with no obstructions is adopted as the reference. Figure 6.12 presents the pressure field and the pressure drop over a line that crosses the channel at the center (following the z-axis). Note that the observed pressure drop is the difference between the imposed pressure at the inlet and the outlet.

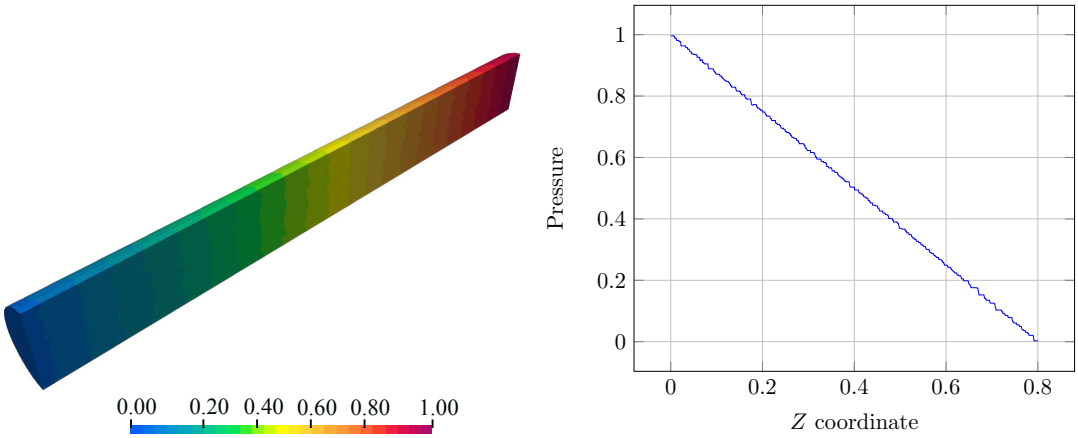

(a) Pressure field. (b) Pressure drop.

Figure 6.12: Results for the reference domain without obstruction.

Figure 6.13 shows the velocity field and the velocity profile over the same line. The variations observed in the velocity profile are due to the mesh refinement. The element size h_{el} is set to 1 cm for all simulations.

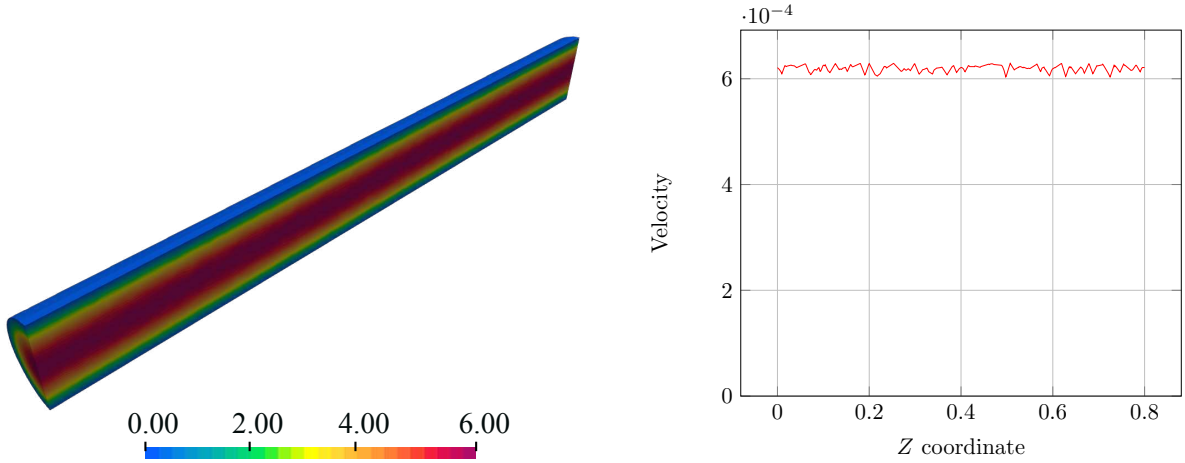

(a) Velocity field ($\times 10^{-4}$). (b) Velocity profile.

Figure 6.13: Results for the domain without obstruction.

Figures 6.14 to 6.17 show the results for the pressure field and the pressure drop for the domain with obstructions of different sizes. Note that, the wider the obstruction, the more pressure is lost by the friction of the fluid with the walls, and naturally the more similar the pressure drop is to the reference case.

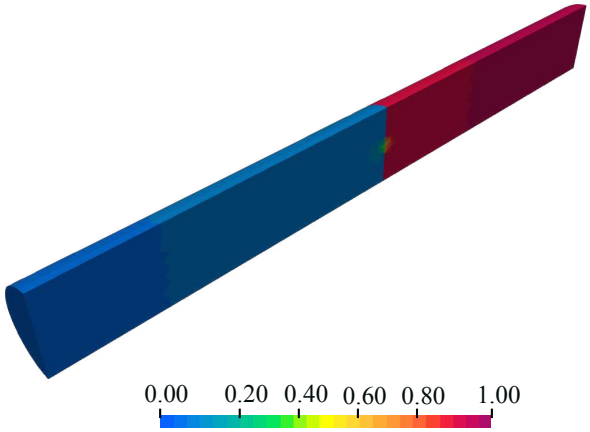

(a) Pressure field.

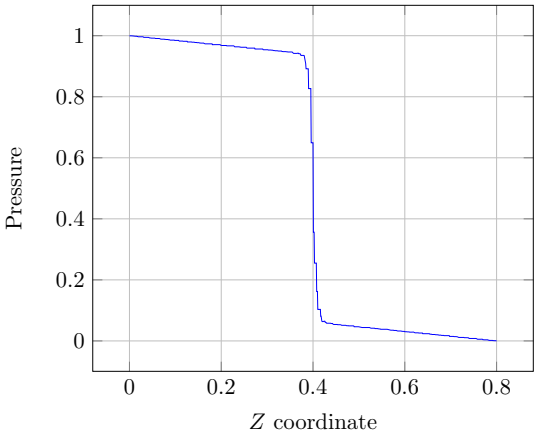

(b) Pressure drop.

Figure 6.14: Results for the domain with obstruction of radius 0.1 cm.

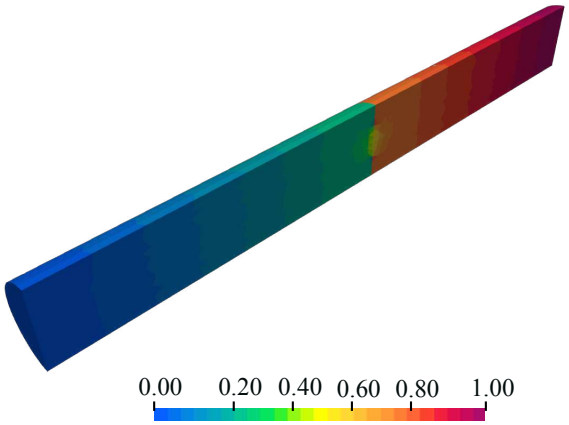

(a) Pressure field.

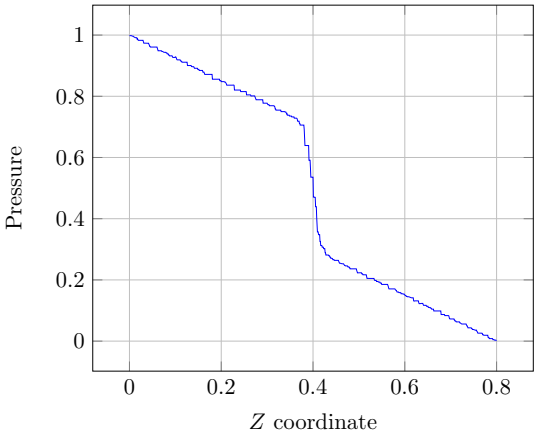

(b) Pressure drop.

Figure 6.15: Results for the domain with obstruction of radius 0.2 cm.

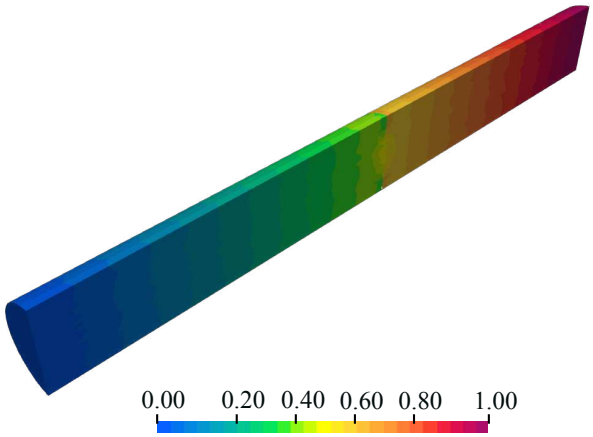

(a) Pressure field.

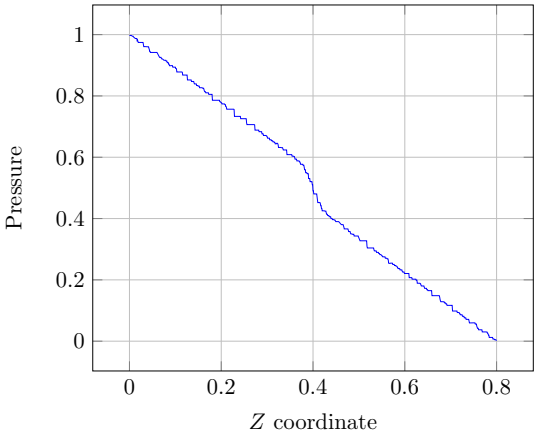

(b) Pressure drop.

Figure 6.16: Results for the domain with obstruction of radius 0.3 cm.

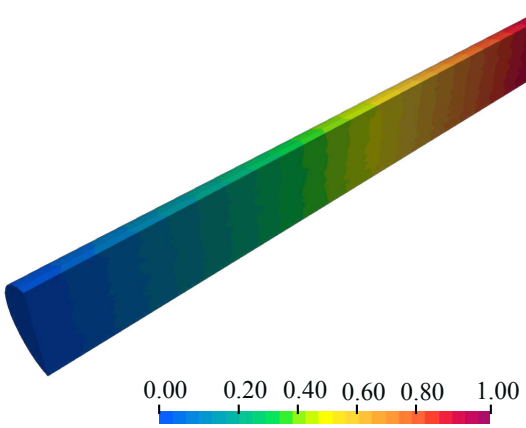

(a) Pressure field.

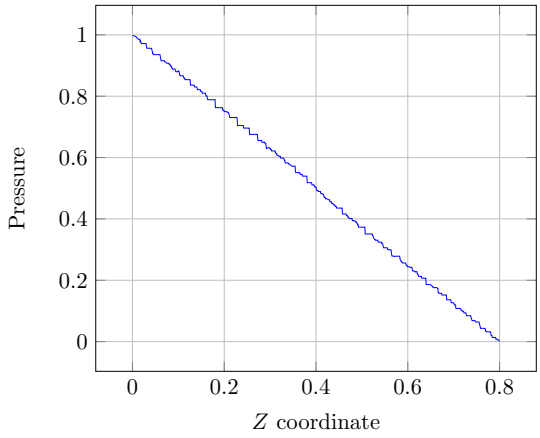

(b) Pressure drop.

Figure 6.17: Results for the domain with obstruction of radius 0.4 cm.

In the first case, with the 1 cm radius obstruction, the pressure drop observed due to the obstruction is 0.8, approximately. This amount slightly decreases as the obstruction radius increases. For 2 cm, the pressure drop is 0.4, for 3 cm, less than 0.1, and finally, for 4 cm, the obstruction is almost imperceptible.

Figures 6.18 to 6.21 show the velocity and the velocity profile for the same domains. Since the inlet flow is not fixed, the velocity field magnitude for wider obstructions is observed to be higher than for narrower ones. The velocity profiles also show that the peak velocity, at the center of the channel, is higher for narrower obstructions.

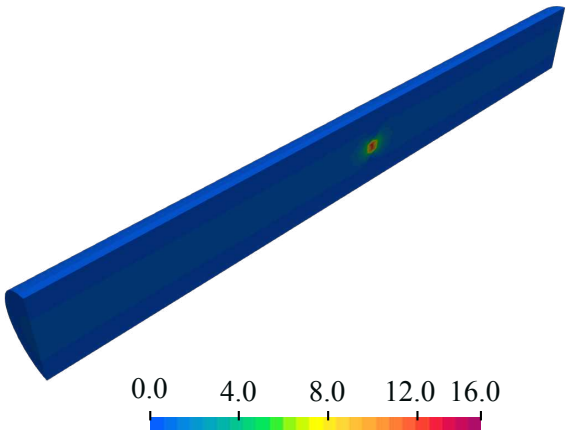

(a) Velocity field ($\times 10^{-4}$).

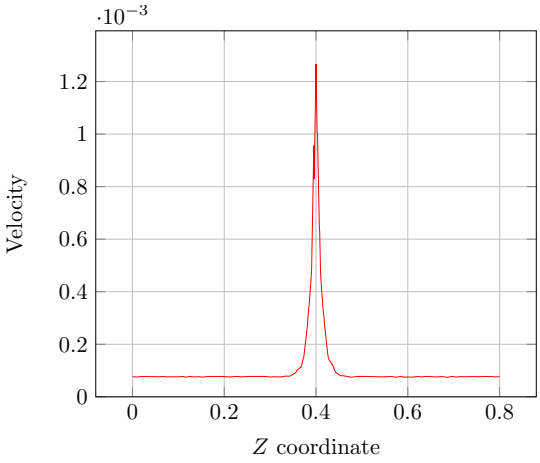

(b) Velocity profile.

Figure 6.18: Results for the domain with obstruction of radius 0.1 cm.

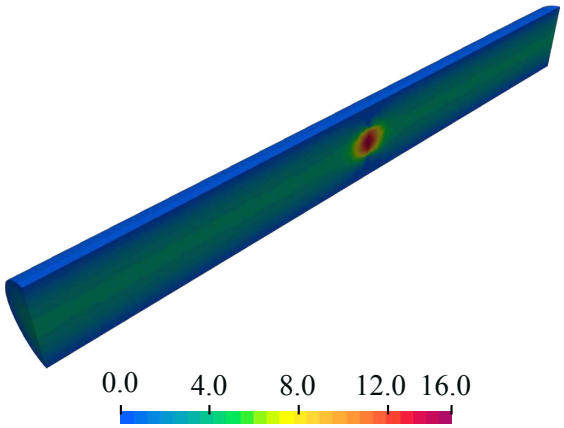

(a) Velocity field ($\times 10^{-4}$).

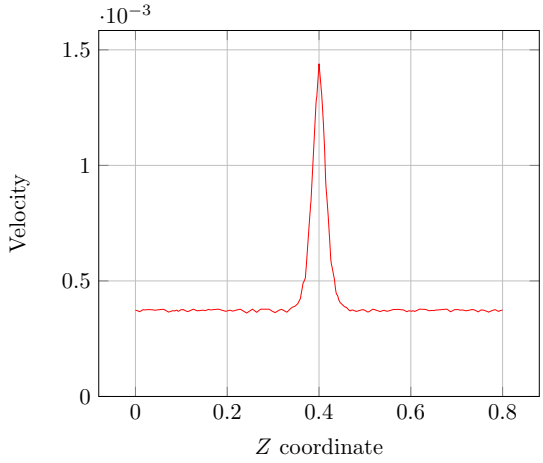

(b) Velocity profile.

Figure 6.19: Results for the domain with obstruction of radius 0.2 cm.

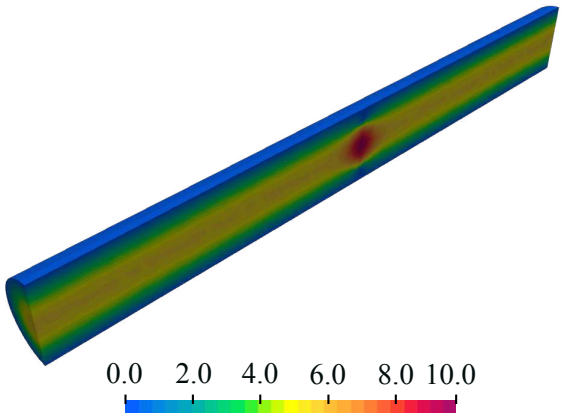

(a) Velocity field ($\times 10^{-4}$).

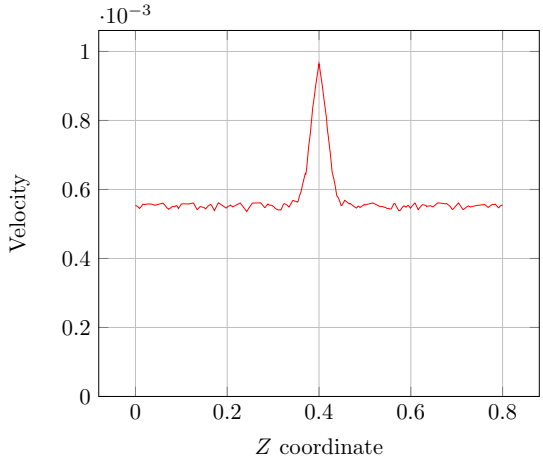

(b) Velocity profile.

Figure 6.20: Results for the domain with obstruction of radius 0.3 cm.

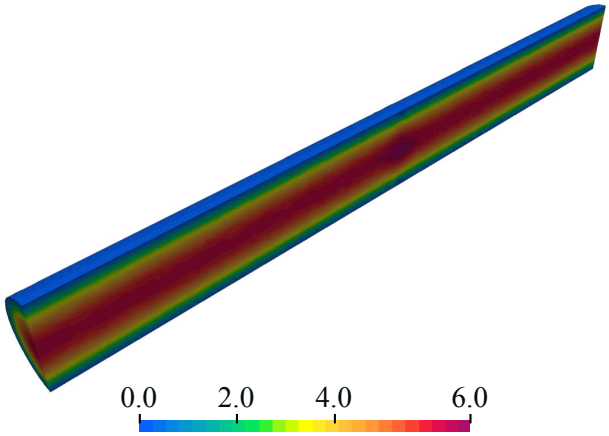

(a) Velocity field ($\times 10^{-4}$).

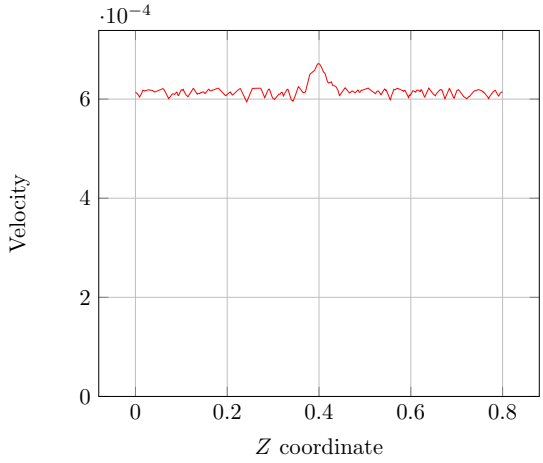

(b) Velocity profile.

Figure 6.21: Results for the domain with obstruction of radius 0.4 cm.

The velocity profiles also show the distance from the obstruction at which the flow is perturbed. Approximately 5 cm before and after the obstruction, the velocity profile begins to change. Afterward, the flow pattern is reestablished. The peak velocity is observed at the center of the channel, where the obstruction is placed. As the obstruction's radius increases, the peak velocity decreases, and the velocity profile becomes more uniform. For the larger obstruction, although no disturbance is observed in the pressure gradient, the velocity profile is still affected by the reduction of the channel's cross-section.

A similar study can be done, changing the obstruction's shape, position, and boundary conditions to evaluate the flow behavior. The optimal geometry for the in-scale prototype can be designed from this analysis and the pressure drop estimated for the 10-meter module. Ultimately, numerical results can also be compared to experimental data to validate the model.

Chapter 7

Conclusions and Future Work

In the development of this work, a methodology for the creation of meshes with obstructed domains is presented, along with the implementation of a new hybrid-hybrid formulation for the Stokes problems. A variation of the hierarchical $H(\mathrm{div}, \Omega)$ spaces, the Hdiv-C, is employed to solve the problems of interest in engineering and scientific applications.

The proposed method is optimal for cases in which local mass conservation is paramount. The new hybrid-hybrid formulation is a suitable alternative for the semi-hybrid formulation, without compromising computational performance. The $H(\mathrm{div}, \Omega)$ spaces presented have demonstrated to be competitive in terms of error and number of DoFs, after applying static condensation, when compared to the Mixed Taylor-Hood. Regarding the matrix structure, the proposed method only has one pressure per element, while the Taylor-Hood presents one pressure per node, resulting in a more complex system.

The condensing process when employing Hdiv-C is straightforward, while for the Hdiv-S additional procedures are required to avoid singular matrices. As expected, the Hdiv-C results for velocity and deviatoric stress are identical to the results obtained with the Hdiv-S. The approximation error for velocity and deviatoric stress, for both Hdiv-S and Hdiv-C, are better than the Taylor-Hood element scheme. Not to mention the fact that, by its point-wise conservation of the mass property, hybrid-hybrid formulation combined with the proper choice of the $H(\mathrm{div}, \Omega)$-$L^2(\Omega)$ spaces leads to a more accurate solution for the divergence of the velocity field than the Taylor-Hood element.

Many examples of applications of the hybrid-hybrid formulation are presented in this work to show the range of possibilities that the method can be used. All the examples are solved with the same Object-Oriented code, which is now incorporated into the NeoPZ library.

Finally, the framework developed to create obstructed domains has shown to be robust and capable of generating different types of obstructions and domains. In addition, the combination of the mesh generator algorithm with the hybrid-hybrid formulation yields accurate simulations with reliable results for the Stokes equations. It is believed that the methodology presented in this work can be used to not only design the optimal geometry for the in-scale prototype but also be employed in many fields of engineering in which the knowledge of the flow modeled by

the Stokes equations is essential.

This project can be extended to different fields of applications. Some of the possible future works are:

- The hybrid-hybrid formulation can be extended to solve Navier-Stokes problems, in which the inertial terms are considered;
- The current constitutive law used for the Cauchy stress tensor only takes into account Newtonian fluids. The code can be extended to include non-Newtonian fluids;
- Work can be done to develop optimal iterative methods that further optimize the methodology of solution of the hybrid-hybrid formulation;
- Within the TotalEnergies project, an experimental analysis of the axial flows in pipes with obstruction devices is expected to be carried out in the next months. The proposed numerical formulation shall be validated.

Bibliography

1 VISHNYAKOV, V. et al. *Primer on enhanced oil recovery*. [S.l.]: Gulf Professional Publishing, 2019.

2 PALSSON, B. et al. The water injection process: a technical and economic integrated approach. *Chemical Engineering Research and Design*, Elsevier, v. 81, n. 3, p. 333–341, 2003.

3 ŁUKASZEWICZ, G.; KALITA, P. *Navier–Stokes Equations: An Introduction with Applications*. [S.l.]: Springer, 2016.

4 STENBERG, R. Analysis of mixed finite elements methods for the stokes problem: a unified approach. *Mathematics of computation*, v. 42, n. 165, p. 9–23, 1984.

5 CAO, J.; KITANIDIS, P. Adaptive finite element simulation of stokes flow in porous media. *Advances in water resources*, Elsevier, v. 22, n. 1, p. 17–31, 1998.

6 GASSMÖLLER, R. et al. Evaluating the accuracy of hybrid finite element/particle-in-cell methods for modelling incompressible stokes flow. *Geophysical Journal International*, Oxford University Press, v. 219, n. 3, p. 1915–1938, 2019.

7 SANDSTRÖM, C. et al. A two-scale finite element formulation of stokes flow in porous media. *Computer Methods in Applied Mechanics and Engineering*, Elsevier, v. 261, p. 96–104, 2013.

8 KOLAŘÍK, F.; PATZÁK, B.; ZEMAN, J. Computational homogenization of fresh concrete flow around reinforcing bars. *Computers & Structures*, Elsevier, v. 207, p. 37–49, 2018.

9 KIM, Y.; LEE, S. et al. Stable finite element methods for the stokes problem. *International journal of Mathematics and Mathematical Sciences*, Hindawi, v. 24, p. 699–714, 2000.

10 HUGHES, T. J.; FRANCA, L. P.; BALESTRA, M. A new finite element formulation for computational fluid dynamics: V. circumventing the babuška-brezzi condition: A stable petrov-galerkin formulation of the stokes problem accommodating equal-order interpolations. *Computer Methods in Applied Mechanics and Engineering*, Elsevier, v. 59, n. 1, p. 85–99, 1986.

11 ZIENKIEWICZ, O. C.; TAYLOR, R. L.; ZHU, J. Z. *The finite element method: its basis and fundamentals*. [S.l.]: Elsevier, 2005.

12 GIRAULT, V.; RAVIART, P.-A. *Finite element methods for Navier-Stokes equations: theory and algorithms*. [S.l.]: Springer Science & Business Media, 2012. v. 5.

13 ARNOLD, D. N.; BREZZI, F.; FORTIN, M. A stable finite element for the stokes equations. *Calcolo*, Springer, v. 21, n. 4, p. 337–344, 1984.

14 GUZMÁN, J.; NEILAN, M. Conforming and divergence-free stokes elements in three dimensions. *IMA Journal of Numerical Analysis*, Oxford University Press, v. 34, n. 4, p. 1489–1508, 2014.

15 BOFFI, D. Three-dimensional finite element methods for the stokes problem. *SIAM journal on numerical analysis*, SIAM, v. 34, n. 2, p. 664–670, 1997.

16 MORGAN, H.; SCOTT, L. R. Towards a unified finite element method for the stokes equations. *SIAM Journal on Scientific Computing*, SIAM, v. 40, n. 1, p. A130–A141, 2018.

17 STENBERG, R. Error analysis of some finite element methods for the stokes problem. *Mathematics of Computation*, v. 54, n. 190, p. 495–508, 1990.

18 TAYLOR, C.; HOOD, P. A numerical solution of the navier-stokes equations using the finite element technique. *Computers & Fluids*, Elsevier, v. 1, n. 1, p. 73–100, 1973.

19 LEHRENFELD, C.; SCHÖBERL, J. High order exactly divergence-free hybrid discontinuous galerkin methods for unsteady incompressible flows. *Computer Methods in Applied Mechanics and Engineering*, Elsevier, v. 307, p. 339–361, 2016.

20 HESTHAVEN, J. S.; WARBURTON, T. *Nodal discontinuous Galerkin methods: algorithms, analysis, and applications*. [S.l.]: Springer Science & Business Media, 2007.

21 BREZZI, F. et al. Discontinuous galerkin approximations for elliptic problems. *Numerical Methods for Partial Differential Equations: An International Journal*, Wiley Online Library, v. 16, n. 4, p. 365–378, 2000.

22 NGUYEN, N. C.; PERAIRE, J.; COCKBURN, B. A hybridizable discontinuous galerkin method for stokes flow. *Computer Methods in Applied Mechanics and Engineering*, Elsevier, v. 199, n. 9-12, p. 582–597, 2010.

23 GIRAULT, V.; RIVIÈRE, B.; WHEELER, M. A discontinuous galerkin method with nonoverlapping domain decomposition for the stokes and navier-stokes problems. *Mathematics of computation*, v. 74, n. 249, p. 53–84, 2005.

24 COCKBURN, B. et al. Local discontinuous galerkin methods for the stokes system. *SIAM Journal on Numerical Analysis*, SIAM, v. 40, n. 1, p. 319–343, 2002.

25 TOSELLI, A. hp discontinuous galerkin approximations for the stokes problem. *Mathematical Models and Methods in Applied Sciences*, World Scientific, v. 12, n. 11, p. 1565–1597, 2002.

26 CARVALHO, P. G.; DEVLOO, P. R.; GOMES, S. M. A semi-hybrid-mixed method for stokes–brinkman–darcy flows with h (div)-velocity fields. *International Journal for Numerical Methods in Engineering*, Wiley Online Library, v. 125, n. 1, p. e7363, 2024.

27 CARVALHO, P. G.; DEVLOO, P. R.; GOMES, S. M. On the use of divergence balanced h (div)-l2 pair of approximation spaces for divergence-free and robust simulations of stokes, coupled stokes–darcy and brinkman problems. *Mathematics and computers in simulation*, Elsevier, v. 170, p. 51–78, 2020.

28 KANSCHAT, G.; RIVIERE, B. A strongly conservative finite element method for the coupling of stokes and darcy flow. *Journal of Computational Physics*, Elsevier, v. 229, n. 17, p. 5933–5943, 2010.

29 WANG, J.; WANG, Y.; YE, X. A robust numerical method for stokes equations based on divergence-free h (div) finite element methods. *SIAM Journal on Scientific Computing*, SIAM, v. 31, n. 4, p. 2784–2802, 2009.

30 CHEN, Y.; HUANG, F.; XIE, X. H (div) conforming finite element methods for the coupled stokes and darcy problem. *Journal of computational and applied mathematics*, Elsevier, v. 235, n. 15, p. 4337–4349, 2011.

31 WANG, J.; YE, X. New finite element methods in computational fluid dynamics by h (div) elements. *SIAM Journal on Numerical Analysis*, SIAM, v. 45, n. 3, p. 1269–1286, 2007.

32 SIQUEIRA, D. D.; DEVLOO, P. R.; GOMES, S. M. A new procedure for the construction of hierarchical high order hdiv and hcurl finite element spaces. *Journal of Computational and Applied Mathematics*, Elsevier, v. 240, p. 204–214, 2013.

33 CASTRO, D. A. et al. Three dimensional hierarchical mixed finite element approximations with enhanced primal variable accuracy. *Computer Methods in Applied Mechanics and Engineering*, Elsevier, v. 306, p. 479–502, 2016.

34 DEVLOO, P. R. et al. An efficient construction of divergence-free spaces in the context of exact finite element de rham sequences. *Computer Methods in Applied Mechanics and Engineering*, Elsevier, v. 402, p. 115476, 2022.

35 HUGHES, T. J.; FRANCA, L. P. A new finite element formulation for computational fluid dynamics: Vii. the stokes problem with various well-posed boundary conditions: symmetric formulations that converge for all velocity/pressure spaces. *Computer methods in applied mechanics and engineering*, Elsevier, v. 65, n. 1, p. 85–96, 1987.

36 FRANCA, L. P.; HUGHES, T. J.; STENBERG, R. *Stabilized finite element methods for the Stokes problem*. [S.l.]: Teknillinen korkeakoulu, 1991.

37 BABUŠKA, I. The finite element method with lagrangian multipliers. *Numerische Mathematik*, Springer, v. 20, n. 3, p. 179–192, 1973.

38 BREZZI, F. On the existence, uniqueness and approximation of saddle-point problems arising from lagrangian multipliers. *Publications des séminaires de mathématiques et informatique de Rennes*, n. S4, p. 1–26, 1974.

39 GURTIN, M. E. *An introduction to continuum mechanics*. [S.l.]: Academic press, 1982.

40 HOLZAPFEL, G. A. *Nonlinear solid mechanics: a continuum approach for engineering science*. [S.l.]: Kluwer Academic Publishers Dordrecht, 2002.

41 OLIVELLA, X. O.; BOSCH, C. Agelet de S. *Continuum Mechanics for Engineers. Theory and Problems*. 2017.

42 BECKER, E. B.; CAREY, G. F.; ODEN, J. T. Finite elements, an introduction: Volume i. *., 258*, p. 1981, 1981.

43 CLOUGH, R. W. The finite element in plane stress analysis. *Proc. 2nd ASCE Confer. On Electric Computation, 1960*, 1960.

44 DEVLOO, P. R. B.; BRAVO, C. M. A. A.; RYLO, E. C. Systematic and generic construction of shape functions for p-adaptive meshes of multidimensional finite elements. *Computer Methods in Applied Mechanics and Engineering*, Elsevier, v. 198, n. 21-26, p. 1716–1725, 2009.

45 ZHANG, L.; CUI, T.; LIU, H. A set of symmetric quadrature rules on triangles and tetrahedra. *Journal of Computational Mathematics*, JSTOR, p. 89–96, 2009.

46 BREZZI, F.; FORTIN, M. *Mixed and hybrid finite element methods*. [S.l.]: Springer Science & Business Media, 2012. v. 15.

47 RAVIART, P.-A.; THOMAS, J.-M. A mixed finite element method for 2-nd order elliptic problems. In: SPRINGER. *Mathematical Aspects of Finite Element Methods: Proceedings of the Conference Held in Rome, December 10–12, 1975*. [S.l.], 2006. p. 292–315.

48 GUYAN, R. J. Reduction of stiffness and mass matrices. *AIAA journal*, v. 3, n. 2, p. 380–380, 1965.

49 IRONS, B. M. A frontal solution program for finite element analysis. *International Journal for Numerical Methods in Engineering*, Wiley Online Library, v. 2, n. 1, p. 5–32, 1970.

50 WILSON, E. L. The static condensation algorithm. *International Journal for Numerical Methods in Engineering*, Wiley Online Library, v. 8, n. 1, p. 198–203, 1974.

51 BARRETT, J. W.; ELLIOTT, C. M. Finite element approximation of the dirichlet problem using the boundary penalty method. *Numerische Mathematik*, Springer, v. 49, p. 343–366, 1986.

52 LEMARIÉ-RIEUSSET, P. G. *The Navier-Stokes problem in the 21st century*. [S.l.]: CRC press, 2018.

53 SHANKAR, P.; DESHPANDE, M. Fluid mechanics in the driven cavity. *Annual review of fluid mechanics*, Annual Reviews 4139 El Camino Way, PO Box 10139, Palo Alto, CA 94303-0139, USA, v. 32, n. 1, p. 93–136, 2000.

54 SRINIVASAN, R. Accurate solutions for steady plane flow in the driven cavity. i. stokes flow. *Zeitschrift für angewandte Mathematik und Physik ZAMP*, Springer, v. 46, p. 524–545, 1995.

55 RODOLFO, A. et al. Multiscale hybrid-mixed methods for the stokes and brinkman equations-a priori analysis. 2024.

56 LUCCI, P. C. de A. *Descrição Matemática de Geometrias Curvas por Interpolação Transfinita*. Tese (Doutorado) — [sn], 2009.

57 COONS, S. A. Surfaces for computer-aided design of space forms. 1967.

58 JACOBS, E. N.; WARD, K. E.; PINKERTON, R. M. *The Characteristics of 78 related airfoil section from tests in the Variable-Density Wind Tunnel*. [S.l.]: US Government Printing Office, 1933.

59 LADSON, C. L. et al. *Computer program to obtain ordinates for NACA airfoils*. [S.l.], 1996.

60 BABAIE, Z.; BAHRAMI, D.; BAYAREH, M. Investigation of a novel serpentine micromixer based on dean flow and separation vortices. *Meccanica*, Springer, v. 57, n. 1, p. 73–86, 2022.

61 KANG, T. G. et al. A chaotic serpentine mixer efficient in the creeping flow regime: from design concept to optimization. *Microfluidics and nanofluidics*, Springer, v. 7, p. 783–794, 2009.

62 GEUZAINE, C.; REMACLE, J.-F. Gmsh: A 3-d finite element mesh generator with built-in pre-and post-processing facilities. *International journal for numerical methods in engineering*, Wiley Online Library, v. 79, n. 11, p. 1309–1331, 2009.

Appendix A

Stokes Repository Code

The code used throughout this work can be found in the following GitHub repository: Labmec/Mixed_Hybrid_Stokes.git